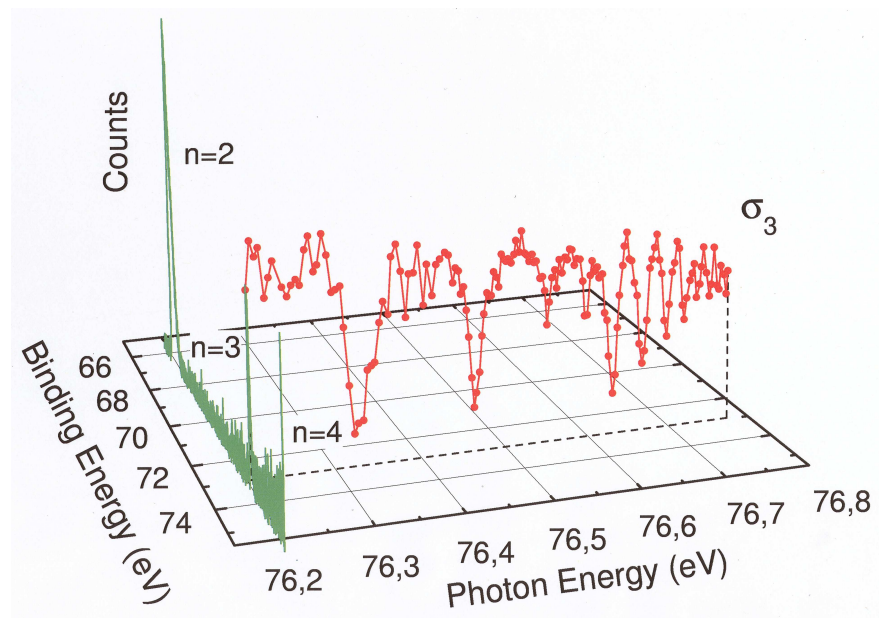


Yuhai Jiang

Doubly excited helium: from strong correlation to chaos



am Fachbereich Physik
der Freien Universität Berlin
eingereichte Dissertation

March 2006

Cover: The bar diagram along the binding energy axis represents an experimental photoemission spectrum measured with $h\nu = 76.2$ eV, with the satellites $n = 2$ to 4 representing the ionic final states of $\text{He}^+(n)$. The solid curve through the data points represents partial cross section σ_3 below the ionization threshold I_5 , which can be derived from a large number of such photoemission spectra (not shown here) recorded at different photon energies. For details, see text in Sect. 5.2.

1. Gutachter: Prof. Dr. Dr. h.c. G. Kaindl
Institut für Experimentalphysik, Freie Universität Berlin, Berlin

2. Gutachter: Prof. Dr. J. M. Rost
Max-Planck-Institut für Physik Komplexer Systeme, Dresden

Tag der Disputation: 03. Mai 2006

To my family

Min Zhang (wife)

Bingquan Jiang (son)

Bingyi Jiang (daughter)

Abstract

In the present dissertation, the double excitation states of helium including the autoionization decay of these states were studied experimentally and theoretically in a broad energy region, which includes the transition from strong correlation below the low single ionization thresholds (SIT) to the region of quantum chaos at energies very close to the double-ionization threshold.

Two kind of experiments were performed, namely total-ion-yield measurements with the aim to observe total cross sections (TCS) and electron time-of-flight (TOF) measurements to obtain partial cross sections (PCS) as well as angular distribution parameters (ADP). Both types of measurements were performed at the third generation synchrotron radiation facility BESSY II in Berlin. The TCSs were recorded up to the SIT I_{15} , and they were found to be in excellent agreement with state-of-the-art complex-rotation calculations performed recently by D. Delande. These experimental and theoretical data on the TCSs were analyzed in order to study quantum chaos in doubly excited helium, and interesting signatures of quantum chaos were found. The TOF technique allowed to measure PCSs and ADPs in the energy regions from I_5 to I_9 and I_7 , respectively. These experimental data provide a critical assessment of theoretical models that can be used to explore the dynamics of strong correlation as well as quantum chaos in helium.

In the theoretical part of this dissertation, the n - and l -specific PCSs and ADPs below I_4 were calculated employing the R-matrix method. The present theoretical results agree well with a recent experimental study of l -specific PCSs below I_4 by J.R. Harries *et al.*

An analysis of patterns in the PCSs and ADPs on the basis of the present experimental and theoretical l -specific data allowed to improve the present understanding of autoionization decay dynamics in this two-electron atom.

Zusammenfassung

In der vorliegenden Arbeit wurden sowohl experimentell als auch theoretisch Doppelanregungszustände des Heliums inklusive deren Zerfälle durch Autoionisation über einen breiten Energiebereich hin untersucht. Dieser Energiebereich spiegelt den Übergang von einem stark korrelierten System unterhalb der untersten Einfachionisationsschwellen (SIT) zu Quantenchaos in der Nähe der Doppelionisationsschwelle von Helium wider.

Im Rahmen dieser Dissertation wurden zwei verschiedene Experimente durchgeführt. Zum einen wurden durch Messungen des Photoionisationsstromes die totalen Wirkungsquerschnitte (TCS) und zum anderen mit Hilfe von Flugzeit-Elektronenspektren die partiellen Wirkungsquerschnitte (PCS) und Winkelverteilungsparameter (ADP) gemessen. Diese beiden Experimente wurden an der Synchrotronstrahlungsquelle BESSY II in Berlin durchgeführt. Die totalen Wirkungsquerschnitte wurden bis zur Einfachionisationsschwelle I_{15} vermessen und zeigen eine exzellente Übereinstimmung mit *state-of-the-art complex-rotation* Rechnungen, die erst kürzlich von D. Delande durchgeführt wurden. Diese experimentellen und theoretischen Daten für den totalen Wirkungsquerschnitt wurden dazu benutzt, den Übergang zu Quantenchaos in Helium zu studieren, wobei interessante und neuartige Signaturen des Quantenchaos gefunden wurden. Die Flugzeitspektren ermöglichten es, die Winkelverteilungsparameter und partiellen Wirkungsquerschnitte für den Energiebereich von der Schwelle I_5 bis zur Schwelle I_7 bzw. I_9 zu messen. Diese Daten erlauben kritische Tests von Modellen, die dazu benutzt werden können, die starke Elektronenkorrelation und – damit verbunden – das Quantenchaos in Helium zu verstehen.

In dem theoretischen Teil dieser Arbeit wurden die n - und l -spezifischen partiellen Wirkungsquerschnitte und Winkelverteilungsparameter bis zur Ionisationsschwelle I_4 mit Hilfe der R-Matrix-Methode berechnet. Diese theoretischen Ergebnisse stimmen gut mit einer ersten experimentellen Untersuchung der l -spezifischen partiellen Wirkungsquerschnitte unterhalb der Ionisationsschwelle I_4 überein, die von J.R. Harris *et al.* durchgeführt wurde.

Die Analyse von Mustern in den partiellen Wirkungsquerschnitten und Winkelverteilungsparametern auf der Basis der l -spezifischen Daten, die sowohl experimentell als auch theoretisch erzielt wurden, erlaubt ein verbessertes Verständnis für die Autoionisation in dem Zweielektronenatom Helium.

Contents

Introduction	5
I Background and basic principles	9
1 Atomic structure and interaction with the electromagnetic field	10
1.1 LS-coupling	10
1.2 Atomic photoionization process	11
1.2.1 Interaction of an atom with a photon	12
1.2.2 Dipole transition approximation	13
1.2.3 Cross sections and angular distribution parameters	14
2 Light source and experimental techniques	17
2.1 Properties of synchrotron radiation	17
2.2 Properties of monochromator	20
2.3 Gas ionization cell	22
2.4 Time-of-flight techniques	23
2.4.1 Time-of-flight electron spectrometer	24
2.4.2 Time-to-Energy conversion	25
2.4.3 Transmission function and analyzer efficiency	28
3 Doubly excited resonances of helium	30
3.1 Parameterizations of resonance profiles in cross sections	32
3.1.1 Fano profiles for the total cross sections	33
3.1.2 Starace's formula for partial cross sections	34
3.1.3 Kabachnik's formula for the angular distribution parameters . . .	35
3.2 Classification schemes for doubly excited resonances of helium	36
3.2.1 Molecular adiabatic approximation	36
3.2.2 Herrick's classification schemes	38
II Experimental photoexcitation and autoionization spectroscopy of helium	41
4 Photoionization cross sections in the ion yield	42

4.1	Wigner distribution and Poisson distribution for energy levels	43
4.2	Ericson fluctuations and autocorrelation function	47
4.3	The classical configurations	49
4.4	Complex-rotation method	51
4.5	Quantum signatures of chaos in highly excited states of helium	52
4.5.1	Experimental total cross sections up to I_{15}	52
4.5.2	Calculated K values up to I_{17}	60
4.5.3	Statistical analysis of nearest-neighbor spacings	67
4.5.4	Porter Thomas distribution of linewidths	70
4.5.5	Lorentzian distribution of Fano q parameters	72
4.6	The angular correlation mechanism around the double-ionization threshold	73
5	Photoionization spectroscopy by TOF measurements	77
5.1	Experimental set-up	78
5.2	Data acquisition	81
5.3	Channel-resolved measurements up to I_9	82
5.3.1	Partial cross sections	83
5.3.2	General pattern	89
5.3.3	Mirroring behavior	91
5.4	Angle-resolved measurements up to I_7	94
5.4.1	Differential cross sections and β parameter	95
 III Theoretical work on photoionization with excitation in helium		99
6	Theoretical calculation of n- and l-specific partial cross sections	100
6.1	R-matrix method	101
6.2	Photoionization spectra below I_3	105
6.2.1	Partial cross sections σ_{nl}	105
6.2.2	Angular distribution parameters β_{nl}	109
6.3	Photoionization spectra below I_4	111
6.3.1	Partial cross sections σ_{nl}	111
6.3.2	Angular distribution parameters β_{nl}	117
 Summary and Outlook		121
 Acknowledgements		124
 Appendices		124
 A Semiclassical case of helium at double-ionization threshold		125
 B Random matrix theory		126

Bibliography	129
Curriculum Vitae	136
Publications and Conference contributions	137

Introduction

The discovery of strong electron correlation effects in double-excitation resonant states of helium in an experiment by Madden and Codling in the 60's of the past century [1] triggered the development of group-theoretical and molecular adiabatic approximation approaches to understand this unexpected strong correlation dynamics described by a set of approximate quantum numbers in low doubly excited states. Close to the double-ionization threshold, the spectra exhibit complicated fluctuations due to electron correlation which finally leads to quantum signatures of chaos [2]. The aim of this dissertation is to study doubly excited helium in a very broad energy range from strong correlation dynamics below the lower ionization thresholds to quantum chaotic dynamics very close to the double-ionization threshold. In addition, the present studies are expected to improve the understanding of electron correlation, develop new concepts for quantum chaos, and also improve the understanding of quantum mechanics from the viewpoint of classical chaos.

Quantum chaos can be considered as the behavior of a quantum mechanical system whose classical counterpart would be chaotic. The field is not limited to theoretical interests related to the quantum-classical correspondence of chaos. Since the 1990's new techniques of fabricating semiconductor microstructures have opened a whole new active research area, namely the field of mesoscopic physics. A large number of interesting systems in the mesoscopic regime, e.g. quantum dots [3, 4] and tunneling devices [5], can be well understood on the basis of quantum chaos [6]. Gutzwiller's trace formula [7, 8] presents the correspondence between quantum mechanics and classical nonlinear mechanics of chaotic systems and has been successfully applied to a number of fields [9]. So far, most of the studies of chaos are limited to simple theoretical model problems with two degrees of freedom such as the double pendulum [10]. For atomic systems, intensive studies have been performed for the hydrogen atom in a strong magnetic field [11, 12, 13, 14, 15]. Very recently, the first experiment on the chaotic scattering of ^{85}Rb atoms was achieved [16, 17]. For doubly excited helium close to the double-ionization threshold, where $\hbar \rightarrow 0$, quantum chaos is expected since its classical counterpart, the classical three-body system, is a nonintegrable system. For this atom, theoretical studies of quantum chaos are mainly focused on 1-D helium [10, 18] and $^1S^e$ doubly excited helium [19], since these studies can be carried out with good accuracy for reasons of simplicity as compared to the $^1P^o$ doubly excited states in 3-D helium.

In this dissertation, the $^1P^o$ doubly excited states in helium are addressed. By absorbing a single photon, ground-state helium can be excited into a singly ionized continuum

state $^1P^o$ by direct and indirect photoionization processes. As a consequence, Fano profiles [20] are observed for the resonances in the cross section due to interference between these two processes. For the studies from strong correlation to quantum chaos in doubly excited helium, two kinds of experiments were performed in the dissertation. One is the measurement of total cross sections (TCS) by monitoring the total ion yield with a gas cell [21]. This technique provides high count rates and allows to measure the spectra with small cross sections extremely close to the double-ionization threshold, where one expects quantum signatures of chaos. In contrast to the total ion yield measurements of the TCS, the measurements for partial cross sections (PCS) and angular distribution parameters (ADP) were performed by detecting photoelectron spectra with an advanced time-of-flight (TOF) technique [22]. This technique can distinguish between the decay channels to the different final states $\text{He}^+(n)$ by measuring the various kinetic energies of emitted electrons. For this topic, our studies focus on strong correlation dynamics of autoionization in doubly excited helium in the intermediate energy region, i.e. below the single ionization thresholds (SIT) I_5 to I_9 . The SIT I_N implies the energy when the principal quantum number of the inner electron in doubly excited states is N and the one of the outer electron is infinite. Both kinds of measurements were performed using third-generation synchrotron radiation light sources. High brightness of the light and the high-resolution monochromators are prerequisites for performing these state-of-the-art experimental studies. Some fundamental knowledge about the atomic interaction with the electromagnetic field as well as about the properties of synchrotron radiation and monochromators is introduced in the first part of this dissertation.

Due to strong electron correlation inside the helium atom, the spectra of the double-excitation states cannot be described by traditional quantum numbers like e.g. the orbital angular momentum quantum number. Instead, a set of approximate quantum numbers were introduced for the description of the spectra [23]. It was later shown that these approximate quantum numbers are identical to the exact quantum numbers which describe the separable two-center Coulomb problem of H_2^+ [24]. In the energy region above I_4 , the most interesting features are caused by perturbers; these are low lying resonances of Rydberg series belonging to higher ionization thresholds, which interfere with Rydberg series that converge towards a lower ionization threshold. Predicted by quantum defect theory [25], these perturbers will influence the energy positions of the Rydberg resonances by an increase of the quantum defect by one within the region of the interference; the linewidths and Fano parameters q of the corresponding Fano resonances are also modulated. In the region close to the double-ionization threshold, the interferences due to the overlap of several perturbers with different Rydberg series render the observed spectra highly complicated. In this case, the approximate quantum numbers reflecting strong electron correlation are expected to lose their physical meaning, and the regularities in the two-electron resonance spectrum start to dissolve. If many resonances in the spectrum are strongly overlapping and the spectra hence fluctuating, one expects the occurrence of Ericson fluctuations [26] in the spectra; they are, together with the loss of good quantum numbers, assumed to be features of quantum chaos. Close

to the double-ionization threshold, the helium atom can be described in a semiclassical way. Considering that its classical counterpart is nonintegrable, one expects to see the manifestations of chaos in doubly excited helium from a study of quantum numbers, spectral fluctuations, and the statistical properties of resonance parameters. Therefore, the last eV below the double-ionization threshold has drawn considerable attention in both experimental and theoretical studies.

Recently, Püttner *et al.* have performed experimental and theoretical studies on the TCSs below the SIT I_9 with the result that the statistical properties of the energy levels revealed a transition towards quantum chaos [18]. In this dissertation, the experimental studies on the TCS are extended up to the SIT I_{15} , i.e. up to 6 further thresholds are measured. These new data will be analyzed together with the results of very recent state-of-the-art complex-rotation calculations of Delande [27] that were carried out up to the SIT I_{17} . This experimental and theoretical progress makes it possible to explore the exciting physical phenomenon—quantum chaos in doubly excited helium. On the basis of these data, the approximate quantum numbers, the question Ericson fluctuations as well as the statistical properties of energy levels, linewidths, and Fano parameters q will be topics in this dissertation. The statistical analysis displayed interesting precursor quantum signature of chaos in doubly excited helium. Many unexpected results were found and interesting questions such as the absence of Ericson fluctuations will be addressed. Semiclassical configurations [2, 28] related to the double-ionization dynamics in helium are employed to understand the chaotic dynamics of doubly excited resonances. Using the theoretical results, the experimental spectra will be assigned for the first time up to the SIT I_{14} . These highly interesting and novel results will be presented in Sect. 4 of the present dissertation. Up to now, the published experimental and theoretical studies of the TCS were limited to regions below the SIT I_9 [18, 29, 30, 31, 32, 33].

The studies of the PCSs and ADPs of doubly excited states of helium below the SITs I_5 to I_9 are performed with the TOF electron spectrometers and presented in Sect. 5 of this dissertation. These PCSs and ADPs show similarity which are called general pattern [34, 35]. They can be understood on the basis of propensity rules for autoionization decay [31, 33]. In this chapter, we will prove experimentally the presence of the general patterns up to the SIT I_9 , but does not work well due to more and more perturbers. Interesting features, such as the mirroring behavior [36, 37, 38] of double-excitation resonances will also be addressed in this dissertation. Since the PCSs and the ADPs can carry additional information on the coupling of between outgoing channels, more resonances are expected to be observed in the PCSs than in the TCSs. Their clarifications can improve the understanding to the decay dynamics of doubly excited autoionization resonances. In addition, the PCSs and the ADPs provide additional tests of the quality of the theoretical data that are employed in our statistical study of quantum chaos [18].

Theoretical n - and l -specific PCSs and ADPs as well as corresponding TCSs below the SIT I_4 were calculated by the R-matrix method; the results are given in the last part of dissertation. A justification of this theoretical work is the impressive agreement

between the results of the present calculations and those of very recent measurements of the l -specific PCSs by Harries *et al.* [39, 40]. On the basis of reliable l -specific PCSs and ADPs, more general cross section patterns such as mirroring behavior and mimicking behavior [38] are expected to appear, which can further improve the understanding of correlation and decay dynamics in two-electron atoms.

Part I

Background and basic principles

Chapter 1

Atomic structure and interaction with the electromagnetic field

1.1 LS-coupling

The electronic structure of an atom is determined by the Coulomb interaction between the electrons and the nucleus, as well as between different electrons which is commonly called electron correlation. In the non-relativistic limit, the Hamiltonian H for an atom with N electrons is given in atomic units by

$$H = \sum_{i=1}^N \left(-\frac{1}{2} \nabla_i^2 - \frac{Z}{r_i} \right) + \sum_{i < j=1}^N \frac{1}{r_{ij}}, \quad (1.1)$$

where r_i denotes the relative coordinate of the electron i with respect to the nucleus and $r_{ij} = |r_i - r_j|$. By approximating the Coulomb interaction between the electrons with a mean effective spherical potential $V(r)$, equation (1.1) can be written as

$$H = H_c + H_1 \quad (1.2)$$

with

$$H_c = \sum_{i=1}^N \left(-\frac{1}{2} \nabla_i^2 - \frac{Z}{r_i} \right) + V(r_i) \quad (1.3)$$

and

$$H_1 = \sum_{i < j=1}^N \frac{1}{r_{ij}} - V(r_i). \quad (1.4)$$

H_1 represents the difference between the actual and the averaged Coulomb interactions of the electrons, and contains electron correlation effects. The term H_1 is normally small compared to the terms Z/r_i and $1/r_{ij}$ and can, therefore, be regarded as a perturbation. Due to strong electron-electron correlation in doubly excited two-electron systems, like helium, the Hamiltonian in Eq. (1.2) cannot simply be solved with the perturbation

method. However, the mixing of two-electron hydrogenic configurations due to the interaction term $1/r_{ij}$ can be described well by group-theoretical techniques [23] but not by independent electron picture, resulting in new approximated quantum numbers to characterize the doubly excited states instead of the orbital angular momentum quantum numbers in two-electron systems.

In the relativistic case, other interactions have to be added, of which the spin-orbit interaction represents the largest contribution, which is given by

$$H_2 = \sum_i \xi(r_i) l_i \cdot s_i, \quad (1.5)$$

where $\xi(r_i) = \frac{1}{2r_i} \frac{dV(r_i)}{dr_i}$. l_i and s_i are the orbital angular momentum and spin angular momentum of electron i , respectively. If $H_1 \gg H_2$, the dominating Coulomb interaction preserves the spin and the orbital angular momentum and the vector sums of the individual angular momenta

$$L = \sum l_i \quad \text{and} \quad S = \sum s_i. \quad (1.6)$$

From these, one obtains the total angular momentum J from the coupling

$$J = L + S. \quad (1.7)$$

This is called *LS-coupling*. The opposite case, $H_1 \ll H_2$, is called *jj-coupling* and requires that

$$j_i = l_i + s_i \quad \text{and} \quad J = \sum j_i. \quad (1.8)$$

The case that both perturbations, H_1 and H_2 , are of the same order of magnitude is difficult to handle because both terms must then be treated on the same footing. This situation is called *intermediate coupling*. As a rough rule, one can use *LS-coupling* for the outer shells in low- Z elements, and *jj-coupling* for inner shells in high- Z elements. For other cases, *intermediate coupling* is often required.

From these considerations, *LS-coupling* is expected for He, however, for the special case of doubly excited resonances of helium very close to the $\text{He}^+(N=2)$ ionization threshold, recent experimental [41] and theoretical results [42] have confirmed that the spin-orbit interaction significantly contributes to the total energy of the atom, and results in a breakdown of *LS-coupling*. Since this particular energy region is not of interest in the present work, the discussions on experimental results and theoretical calculations is based on *LS-coupling* throughout this dissertation.

1.2 Atomic photoionization process

An atom can be ionized by obtaining extra energy from an incoming photon if the extra energy is larger than the negative potential of a bound electron. The single photoionization process of an atom can be expressed by

$$A + h\nu \rightarrow A^+ + e^- . \quad (1.9)$$

This single photoionization process obeys mainly the dipole selection rule for an electronic dipole transition (i.e. a change of the total orbital angular momentum $\Delta L = \pm 1$ and the parity). In the final state, one electron is free and the others remain in a positive ion either in the ground state or in the excited state.

The interaction of a photon with an atom resulting in ionization is usually expressed in terms of a cross section, σ , which is defined as the *transition probability per unit time and per unit target scatterer and per unit flux of incident particles with respect to the atom*. If this photoionization can lead to various channels, i.e. the remaining electrons in the ion could be in various energy levels, we call the cross section specifying to one channel a partial cross section (PCS). In doubly excited helium, PCSs σ_n or σ_{nl} describe satellite cross sections leading to the final states $\text{He}^+(\text{n})$ or $\text{He}^+(\text{nl})$, respectively. A total cross section (TCS), σ_T , can be regarded to be the sum of all PCSs, σ_n or σ_{nl} . The parameter β is related to the scattering angle θ in Eq. (1.22), so that it is called angular distribution parameter (ADP). The ADP together with the TCS and the PCS have become standard quantities in the study of the interactions between photons and atoms. In this section, we shall briefly introduce the derivations of the TCSs, the PCSs, and the ADPs that are employed in this dissertation in order to observe electron correlations and transitions in doubly excited helium.

1.2.1 Interaction of an atom with a photon

For an electron in the electromagnetic field, the mechanical momentum \mathbf{p} has to be replaced by the canonical momentum, which includes the vector potential \mathbf{A} of the field. The scalar potential Φ of the electromagnetic field is also added, giving

$$H = \frac{(\mathbf{p} - e\mathbf{A})^2}{2m_0} + \Phi \quad (1.10)$$

for the Hamiltonian. In Coulomb gauge and space-free electromagnetic field, e.g. in the external field of monochromatized synchrotron radiation, \mathbf{A} and Φ can be chosen

$$\nabla \cdot \mathbf{A} = 0 \quad \text{and} \quad \Phi = 0. \quad (1.11)$$

Under these conditions, the synchrotron radiation field can be described by

$$\mathbf{A}(\omega; \mathbf{r}, t) = A_0 \epsilon \left\{ e^{i(\mathbf{k} \cdot \mathbf{r} - \omega t)} + cc \right\}, \quad (1.12)$$

where ϵ is the polarization vector, A_0 the field intensity, and cc the complex conjugate; \mathbf{k} , \mathbf{r} , ω , and t have their normal meanings. One can regard the interaction with the radiation field as an additional potential energy term, which perturbs the atom with the vector potential \mathbf{A} alone.

The time-dependent Schrödinger equation in an electromagnetic field then reads

$$i\hbar \frac{\partial \Psi}{\partial t} = \left[\frac{(\mathbf{p} - e\mathbf{A})^2}{2m_0} + V(r) \right] \Psi, \quad (1.13)$$

where $\mathbf{p} = -i\hbar\nabla$ and $V(r)$ is the Coulomb potential. With the conditions given in Eq. (1.11), this results in

$$(\mathbf{p} - e\mathbf{A})^2 \Psi = (p^2 - 2e\mathbf{A} \cdot \mathbf{p} + e^2 A^2) \Psi. \quad (1.14)$$

One can therefore write the Schrödinger equation (Eq. (1.13)) as

$$i\hbar \frac{\partial \Psi}{\partial t} = \left[H_{atom} + \frac{ie\hbar}{m_0} \mathbf{A} \cdot \nabla + \frac{e^2}{2m_0} A^2 \right] \Psi. \quad (1.15)$$

From the full Hamiltonian given in Eq. (1.15) with three terms, only one term, namely $\mathbf{A} \cdot \nabla$, is responsible for the photon-atom interaction. For a weak vector potential A , it can be treated as a perturbation. On the same footing, the contribution of term A^2 can also be neglected. Employing time-dependent perturbation theory and Fermi's golden rule for the transition rate w from an initial atomic state $|i\rangle$ to a final atomic state $|f\rangle$, one obtains

$$w = \frac{2\pi}{\hbar} |\langle f | H_{int} | i \rangle|^2 \delta(\text{energy conservation}), \quad (1.16)$$

with the time-independent interaction

$$H_{int} = \frac{e\hbar}{2m_0} A_0 e^{i\mathbf{k} \cdot \mathbf{r}} \boldsymbol{\epsilon} \cdot \nabla. \quad (1.17)$$

1.2.2 Dipole transition approximation

The transition matrix between the initial state $|i\rangle$ and the final state $|f\rangle$ can be written according to Eqs. (1.16) and (1.17) as

$$D_{if} \propto \langle f | e^{i\mathbf{k} \cdot \mathbf{r}} \boldsymbol{\epsilon} \cdot \nabla | i \rangle. \quad (1.18)$$

In many cases of practical interest this matrix can be simplified by expanding the exponential function $e^{i\mathbf{k} \cdot \mathbf{r}}$ as

$$e^{i\mathbf{k} \cdot \mathbf{r}} = 1 + (i\mathbf{k} \cdot \mathbf{r}) + \frac{1}{2!} (\mathbf{k} \cdot \mathbf{r})^2 + \dots \quad (1.19)$$

Normally in the low-photon-energy region, the $\mathbf{k} \cdot \mathbf{r}$ term in the expression given in (1.19) is three orders of magnitude smaller than unity. If one just includes the first term, unity, in this expansion, it is known as the *electric dipole approximation*. The electric quadrupole transitions or magnetic dipole transitions described by the second term of Eq. (1.19) are weaker by a factor α^2 for low energies (< 1000 eV), and under these conditions, electric dipole approximation works well. Here, α is the fine structure constant. As the photon energy increases, the electric quadrupole transition strength being proportional to $\omega^4 \alpha^2$, increases dramatically in comparison to the electric dipole transition strength being proportional to ω^2 and magnetic dipole transition being proportional to $\omega^2 \alpha^2$ (for details, see Ref. [43]). Therefore, for doubly excited resonances of helium, which all

have excitation energies below 79 eV, the electric dipole approximation can be employed safely throughout this dissertation. Since the magnetic dipole term is at least a factor α^2 smaller than the electric dipole term, it can be neglected even in the low-energy region.

If one uses linearly polarized light in dipole approximation, the dipole transition matrix D_{if} in Eq. (1.18) can be written as $\langle f | \nabla | i \rangle$, which is called the *velocity form*. With the help of the general commutation relation

$$\frac{d\mathbf{r}}{dt} = \frac{\partial \mathbf{r}}{\partial t} + \frac{i}{\hbar} [H, \mathbf{r}] = \frac{i}{\hbar} [H, \mathbf{r}] \quad (1.20)$$

and $\mathbf{p} = i\hbar \nabla = m_0 d\mathbf{r}/dt$, one finds

$$\langle f | \nabla | i \rangle = m_0 (E_f - E_i) \langle f | \mathbf{r} | i \rangle = m_0 \omega \langle f | \mathbf{r} | i \rangle, \quad (1.21)$$

which is called the *length form* of the dipole matrix. These forms of the dipole matrix are completely equivalent only for exact initial- and final-state wavefunctions since the relations $H|x\rangle = E_x|x\rangle$, with $x = i$ and f , are used in Eq. (1.21). Therefore, the differences of the matrix elements in these two forms are often used to check the quality of the target wavefunctions used in calculations. In Part III of this dissertation, our calculations employing R-matrix method will be presented in both forms, velocity form and length form.

1.2.3 Cross sections and angular distribution parameters

For photoelectrons ejected from atoms by linearly polarized radiation, the differential cross sections (DCS) can be written, in the electric dipole approximation, as [44, 45, 46]

$$\frac{d\sigma_{nl}}{d\Omega} = \frac{\sigma_{nl}}{4\pi} \left[1 + \beta_{nl} \left(\frac{3\cos^2\theta - 1}{2} \right) \right], \quad (1.22)$$

where n and l are, respectively, the principal and the orbital angular momentum quantum numbers of the residual ion, θ is the angle between the momentum of the photoelectron and the polarization vector of the photon with both directions being in the plane perpendicular to the light propagation direction, which is called *dipole plane*. The PCS σ_{nl} , which leads to the final state $|nl\rangle$ of the ion, can be written as

$$\sigma_{nl} = \frac{1}{3(2L_i + 1)} \sum_{l', L_f} |M(nll'L_f)|^2. \quad (1.23)$$

The ADPs β_{nl} can be described by [45, 46]

$$\begin{aligned} \beta_{nl} = & \frac{5}{\sigma_{nl}(2L_i + 1)} (-1)^{L_i l} \sum_{l'_1, L_f^1} \sum_{l'_2, L_f^2} \left[(2l'_1 + 1)(2l'_2 + 1)(2L_f^1 + 1)(2L_f^2 + 1) \right]^{1/2} \\ & \times \begin{pmatrix} 1 & 1 & 2 \\ 0 & 0 & 0 \end{pmatrix} \begin{pmatrix} l'_1 & l'_2 & 2 \\ 0 & 0 & 0 \end{pmatrix} \left\{ \begin{matrix} 1 & 1 & 2 \\ L_f^1 & L_f^2 & L_i \end{matrix} \right\} \left\{ \begin{matrix} l'_1 & l'_2 & 2 \\ L_f^1 & L_f^2 & l \end{matrix} \right\} \\ & \times M(nll'_1 L_f^1) M(nll'_2 L_f^2)^*. \end{aligned} \quad (1.24)$$

L_i and L_f are the orbital angular momenta of initial and final states, respectively, and l' is the orbital angular momentum of the photoelectron. $M(nll'L_f)$ is the transition amplitude in the electric dipole approximation and includes the Coulomb phase shift factor. From the experimental side, equations (1.23) and (1.24) for the PCSs, σ , and the ADPs, β , are too complicated to be employed for profile analysis of the spectra. Therefore, these expressions have to be parametrized, which will be presented in detail in Sect. 3.1 together with the parametrization of the resonances in the TCSs, σ_T .

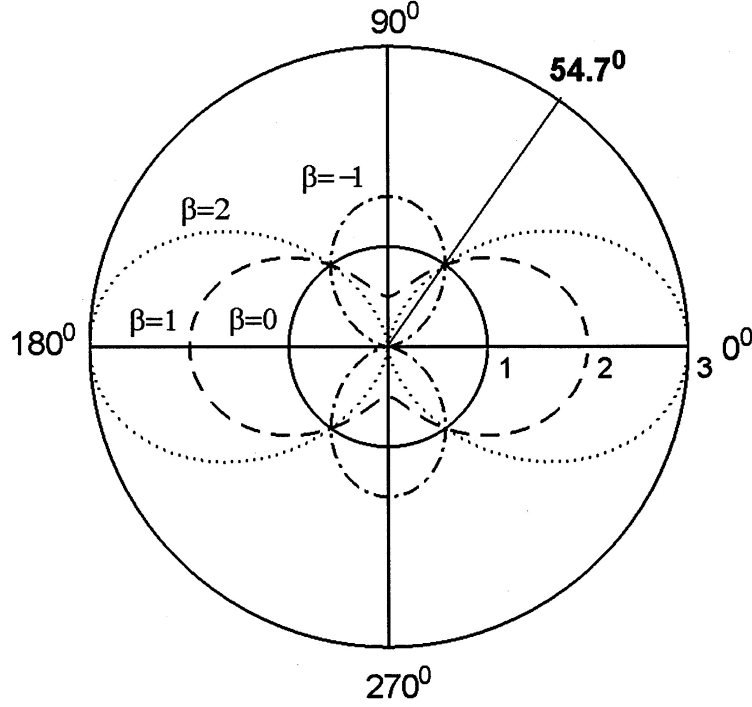


Figure 1.1: Polar plot of the angular distributions of photoelectrons for the four values $\beta = -1, 0, 1$, and 2 .

From Eq. (1.22), one can derive that the β_{ns} is equal to 2 in LS-coupling. In addition, the requirement that the DCSs in Eq. (1.22) cannot be negative results implies that the values of the ADPs β are restricted by the inequality

$$-1 \leq \beta \leq 2. \quad (1.25)$$

The angular distributions of photoelectrons for the four values $\beta = -1, 0, 1$, and 2 are plotted in Fig. 1.1. The PCS can be measured directly by mounting the detector at the magic angle, $\theta \approx 54.7$, since under this condition the second term in Eq. (1.22) becomes equal to zero. From Fig. 1.1, one can also see that the photoelectron intensity at the magic angle is independent of the β values. Due to the two unknown parameters σ_{nl} and β_{nl} in Eq. (1.22) at least two detectors have to be mounted at different angles in order to obtain the ADPs from the experiment. A larger number of detectors can, however, provide more precise values for β . Later in this dissertation, two photographs of the experimental set-up allowing the use of up to 12 TOF spectrometers are shown, which was used in the ADP measurements of this dissertation.

In theory, the n -specific ADP β_n are related to the nl -specific β_{nl} by

$$\beta_n = \frac{-8\pi A_n^2}{\sigma_n} = \frac{-8\pi \sum_l A_{nl}^2}{\sigma_n} = \frac{-8\pi \sum_l \frac{A_{nl}^2}{\sigma_{nl}} \cdot \sigma_{nl}}{\sigma_n} = \frac{\sum_l \beta_{nl} \sigma_{nl}}{\sum_l \sigma_{nl}}, \quad (1.26)$$

where A^2 , referred to A_2 in Ref. [46], is proportional to the real part of the transition amplitude, $\text{Re}M(nll'_1 L_f^1)M(nll'_2 L_f^2)^*$. Note that, experimentally, the terms $\sum_l \beta_{nl} \sigma_{nl}$ and $\sum_l \sigma_{nl}$ are averaged over the energies; therefore, in order to compare with experimental data, the calculated β_n should be obtained by the convoluted terms $\sum_l \beta_{nl} \sigma_{nl}$ and $\sum_l \sigma_{nl}$, and not by a convolution of their fraction; this fact was relevant for the present theoretical work which will be presented in part III.

Chapter 2

Light source and experimental techniques

The use of a third-generation synchrotron radiation (SR) light source, a high-resolution monochromator, and advanced time-of-flight (TOF) techniques allows to measure high-resolution vacuum ultra-violet (VUV) spectra. A modern SR light source in combination with a undulator provides high photon flux from the infrared to hard x-rays region. The harmonic radiation from an undulator is selected by a monochromator and results in highly monochromatic light with high intensity, which is needed for the present photoionization measurements of doubly excited helium. The well-defined time structure of SR allows TOF electron spectrometers to measure photoelectron time spectra if the storage ring is operated in a single-bunch mode. This technique is particularly well suited for the present studies of channel- and angle-resolved measurements of doubly excited helium because of its high-resolution and good transmission particularly for slow electrons. In this chapter, I shall briefly introduce the properties of SR and monochromators as well as the TOF techniques. In addition, I shall briefly describe the gas cell, which was used for total ion yield measurements of doubly excited helium.

2.1 Properties of synchrotron radiation

A electron that undergoes an acceleration generates electromagnetic radiation (see Fig. 2.1(a)). If the photons are created by electrons with highly relativistic velocities in a circular orbit, this radiation is called SR (see Fig. 2.1(b)). The main difference to Fig. 2.1(a), which displays the non-directed emission pattern of an accelerated charged particle at non-relativistic velocities, is the strong forward direction of SR (Fig. 2.1(b)). Due to the relativistic velocity of the circulating electrons, the emission pattern of the radiation is dramatically pushed into forward direction (see Fig. 2.1). The opening half-angle Θ of the cone is proportional to $1/E$ and given by [47]

$$\Theta = \frac{1}{\gamma} = \frac{m_0 c^2}{E}, \quad (2.1)$$

where E is the electron energy, m_0 the rest mass of the electron, and c the velocity of light.

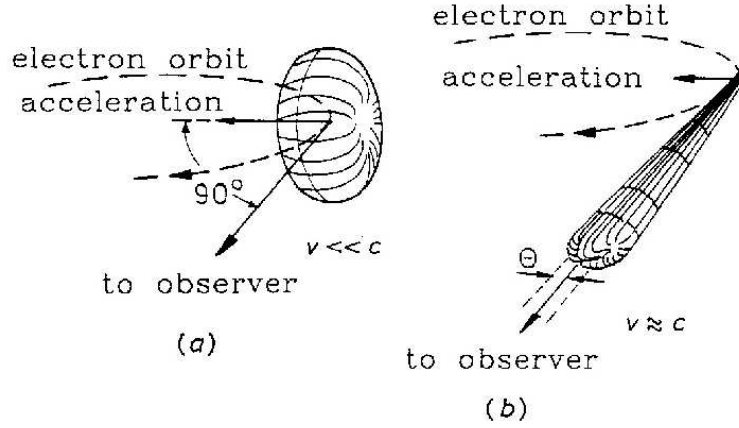


Figure 2.1: Emission pattern of an electron circulating with velocity v : (a) $v/c \ll 1$; (b) $v/c \approx 1$ (from Ref. [47, 48]).

In SR facilities that concentrate on the production of such radiation, the accelerated electrons are stored in a circular ring, called *electron storage ring*. An electron storage ring is composed of many technical components like injection system, microwave cavity for acceleration, bending magnets, focus magnets, vacuum system, and wiggler/undulator. The electrons are generated in an injection system consisting of an electron source and an accelerator, either a synchrotron or a linear acceleration. When the electrons are accelerated to the operating energy of the storage ring, they are injected into the storage ring. The bending magnets are used to deflect the electron beam which ensures the electrons to travel in a circular path. The bending magnets can also serve as the source of SR. In the straight section of the storage ring, a number of focus magnets such as quadrupole magnets are placed for the aim of focusing the electrons. The quadrupole magnets act much like glass lenses in light optics. In order to compensate the energy loss of the electrons during the SR emission, the electrons are accelerated each time as they pass through the RF cavity installed inside the electron storage ring. At the Berliner Elektronenspeicherring für Synchrotronstrahlung (BESSY II), a 500 MHz cavity is operated and results in a time period of 2 ns between two adjacent bunches. Taking 240 m circumference of the storage ring into account, a maximum number of 400 electron bunches can be injected in the multi-bunch operation mode, which was used for our total ion yield measurements presented in chapter 4. In the single-bunch operation mode at BESSY II, only one bunch is filled resulting in a pulse period of 800 ns, which defines the time window for the photoemission measurements with the TOF techniques.

In a simple picture, the wiggler or the undulator can be considered to consist of a large number of bending magnets (see Fig. 2.2), which results in high intensity radiation. When the electrons in the storage ring fly through a bending magnet, a wiggler or an undulator SR is generated. Physically, the undulator and wiggler have similar magnetic structures and they are typically a couple of meters long (more than 10-meter long undulators are operated in free-electron lasers (FEL)). In contrast to the smooth spectral distribution

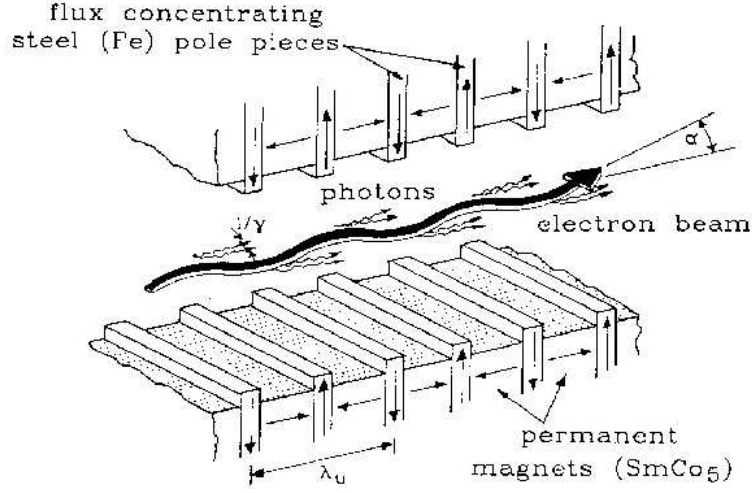


Figure 2.2: The transverse undulator with permanent magnets and iron poles providing a magnetic field with period λ_u . The maximum deflection angle α of the electron beam and the photon emission angle $\Theta = 1/\gamma$ at the maximum bending of the undulators are shown (From [47, 49]).

of radiation from a bending magnet or a wiggler, the radiation from an undulator shows characteristic maxima, which results from the periodic magnetic structure of the insertion devices illustrated in Fig. 2.2. Since it is composed of many bending magnets, the total photon flux radiated from a wiggler increases by a factor equal to the number of poles n in comparison to the radiation from a single bending magnet. In contrast to the radiation distribution of the wiggler, the undulator can produce quasi monochromatic radiation with high brightness peaks (see Fig. 2.3), where the peak intensity is higher by a factor of n^2 as compared to a single bending magnet.

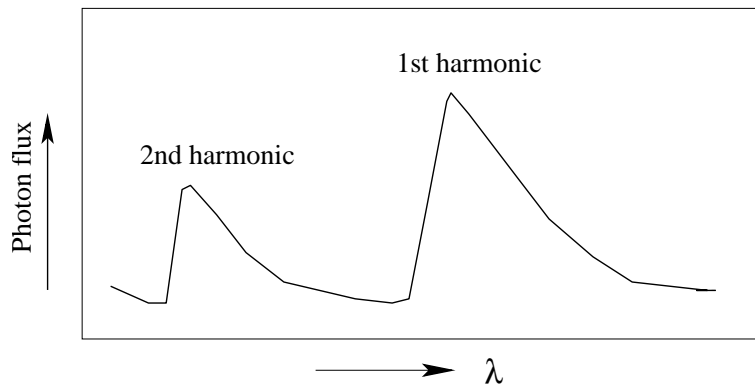


Figure 2.3: Photon flux distribution of an undulator for the first two harmonics.

The interference between electromagnetic waves emitted by the same electron at the different bending magnets of an undulator yields a redistribution of the spatial and spectral intensity. For the radiation emitted at angles Δ and Λ with respect to the

undulator axis, one gets [47]

$$\lambda_n = \frac{\lambda_u \Theta^2}{2n} \left[1 + \frac{K^2}{2} + \frac{\Delta^2 + \Lambda^2}{\Theta^2} \right], \quad (2.2)$$

where λ_n is the wavelength of the n th harmonic radiation ($n = 1$ is the fundamental radiation); λ_u is the magnetic period; Δ and Λ refer to the angles of the radiation emitted in the plane parallel to and perpendicular to the permanent magnets, respectively. $K = \gamma\alpha \propto B_0\lambda_u$ is a characteristic parameter for these devices. Here α and B_0 are the maximum deflection angle and the strength of magnetic field on the axis of the electron beam. Due to the weak magnetic field B_0 and the small period λ_u of the magnetic structure, which cause a small deviation angle α , the undulator has smaller values of K than the wiggler. The essential difference between a wiggler and an undulator lies in the magnetic field strength B_0 .

The harmonics are the characteristics of an undulator spectrum as shown in Fig. 2.3, where the first and the second harmonic are plotted. In order to collimate the undulator light, a small size aperture is placed behind the undulator. Since harmonics with even number are off axis, only odd ones are selected to go through the aperture. According to the energy region required for an experiment, one can choose the harmonic, which provides high photon flux. For doubly excited helium, photon energies from 65 to 79 eV are required so that the 1st harmonics was applied due to its high photon flux. During the measurement, the gap between the permanent magnets of the insertion device has to be adjusted in order to maintain a high photon flux over the whole photon-energy range of the measurement.

2.2 Properties of monochromator

The harmonic radiation of an undulator has to be monochromatized and focused on the spot, where the experiment is performed, via a beamline containing some collimating and focusing elements such as grating, slits, and mirrors.

The present measurements of the PCSs and the ADPs of doubly excited helium were performed at beamline U125/2-SGM (BUS) of BESSY II, which employs a spherical grating monochromator (SGM). The optical layout of the BUS beamline is schematically displayed in Fig. 2.4. The two prefocusing and refocusing mirrors M_1 and M_3 , respectively, are placed in the front and at the end of beamline. An exit slit S_2 , placed in front of M_3 , can be adjusted depending on resolution and flux. For the present measurements, high resolution is needed, and a small aperture of the exit slit S_2 was therefore used. In order to enhance the quality of focused light, an entrance slit S_1 is normally placed behind the prefocusing mirror M_1 in the SGM beamline. The monochromator is a key part and is located in the center of the beamline; it selects a narrow band of the photon energies from the broad energy range of SR and, in addition, focuses the monochromatic light on the exit slit.

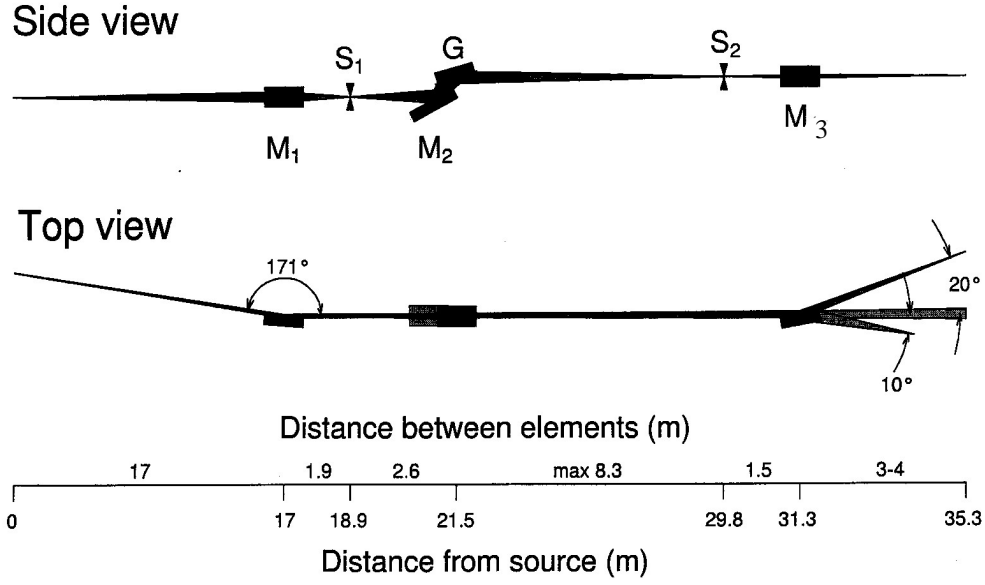


Figure 2.4: Optical layout of spherical grating monochromator in beamline U125/2-SGM at BESSY II (from Ref. [50]).

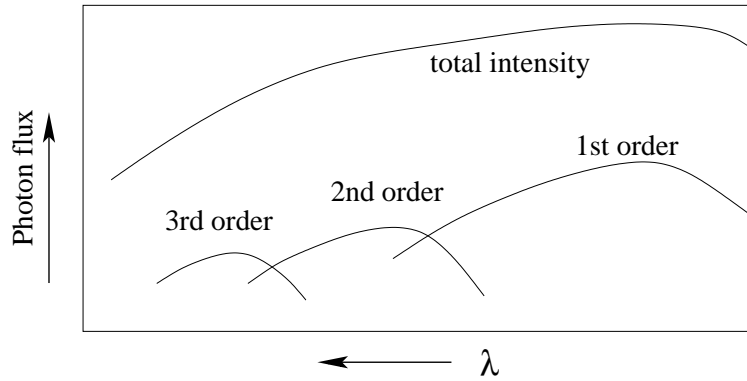


Figure 2.5: Photon flux distributions from a monochromator with the first three orders. The total intensity contains the monochromatized light of all orders.

For a spherical or plane grating of the monochromator, the diffraction from its surface obeys the same equation,

$$m\lambda = d \cdot (\sin\zeta + \sin\eta), \quad (2.3)$$

where d is the distance between successive grooves, m the diffraction order, λ the diffracted wavelength, ζ and η the angles of incidence and diffraction, respectively. ζ and η can be varied by a rotation of the grating, which results in a change of the diffracted wavelength, i.e. the photon energy is selected by varying the angles of incidence and diffraction, ζ and η . Except for the selection of light, the spherical grating has the additional function to focus the diffracted light onto the exit slit. When the wavelength of light is varied, the distance of the focus to the exit slit varies. This is the reason why an

additional plane mirror (M_2 in Fig. 2.4) is installed in the monochromator, which can match the focus requirement by an adjustments of ζ and η as well as of the distance between grating and light source without having to move the position of the exit slit. In order to avoid a loss of flux, large angles of incidence ζ are applied in grating-incidence monochromators for high photon energies. In contrast to grating-incidence monochromators, a normal incidence monochromator with smaller angles ζ is used measurements ($E_{\text{photon}} \leq 30$ eV) for low photon energies.

The proper choice of the numbers of grooves of a grating is mainly determined by the energy region of interest. A spherical grating with a groove density of 1100 l/mm is used for the present PCS and ADP measurements of doubly excited helium for photon energies from 65 to 79 eV.

In Fig. 2.5, the photon flux distributions as a function of wavelength is given for different diffraction orders. The first, second, and third orders of monochromatized light are represented by $m = 1, 2$, and 3 in Eq. (2.3), respectively. According to experimental needs to the flux and the resolution of interest, one can choose the first order of light to gain the flux or the second order of light for higher resolution.

2.3 Gas ionization cell

The measurements of the total photoionization cross section were performed with an ionization cell shown schematically in Fig. 2.6; it contains a two-plate ionization chamber with an active length of 10 cm. The ionization cell was pumped to a pressure of $\leq 10^{-8}$ mbar and then filled with $5 - 1000$ μ bar of the gas under study (noble gas, N_2 , CO, O_2 , etc.); for helium, the pressure was $\cong 0.5 - 1$ mbar. One electrode, used as a repelled electrode, is kept at about +100 V; at the other electrode, the photoionization current in the $10^{-15} - 10^{-12}$ A range is recorded as a function of photon energy by a commercial pico-Ampere-meter (Keithley 6517). The ionization chamber is separated from the ultrahigh vacuum (UHV) of the monochromator (in the 10^{-10} -mbar range) by a 1500-Å-thick Aluminum or 1000-Å-thick Carbon window. In order to avoid disturbing effects due to absorption edges of the window (e.g., Al 2p (at $\cong 73$ eV) or C 1s ($\cong 284$ eV)), the window material was selected according to the photon-energy range studied. For photon energies from 65 to 79 eV in care of doubly excited helium, a carbon window was accordingly used for total-ion-yield measurements. Because the windows cannot withstand pressure differences exceeding $\cong 10$ mbar, special attention was taken during the pump-down of the ionization chamber.

The gas cell was also used for determining the photon energy resolution. The achievable energy resolution, ΔE , depending on the incident photon energy, E , the diffraction order, m , the finite size of the exit slit, ΔE_s , the finite size and stability of the beam source, ΔE_b , as well as the finite quality of the optical elements, ΔE_e , can be expressed by [21],

$$\Delta E \propto E^{3/2} m^{-1/2} (\Delta E_s^2 + \Delta E_e^2 + \Delta E_b^2)^{1/2}. \quad (2.4)$$

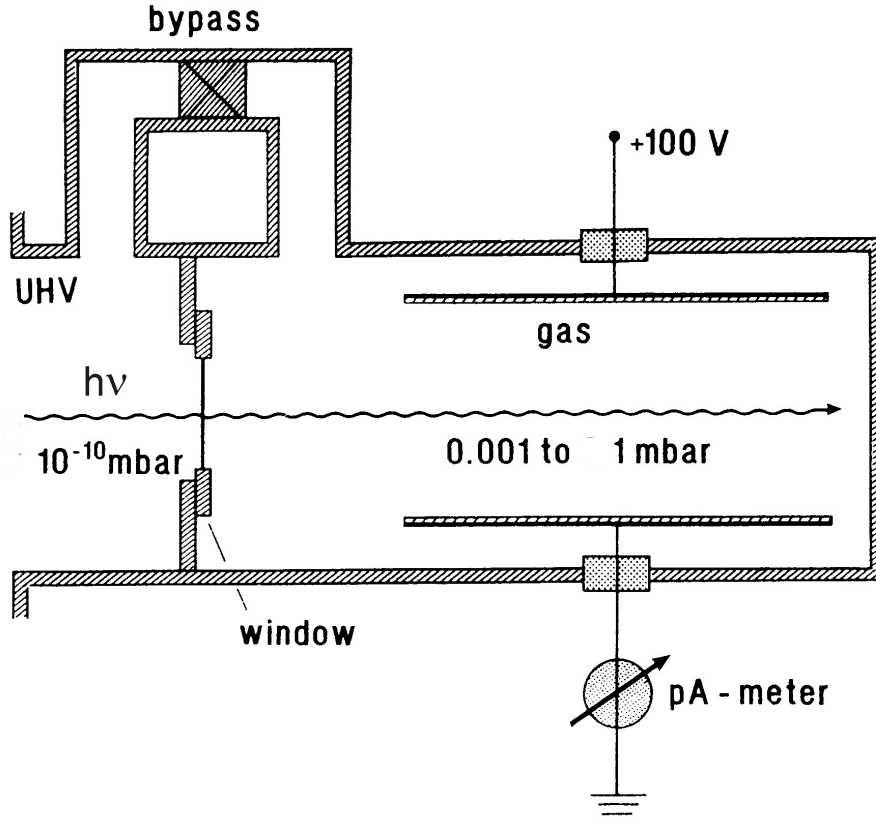


Figure 2.6: Schematic view of the ionization cell (from [21]).

In order to achieve high photon flux, the first order, $m = 1$, was chosen in our measurements, as mentioned before. ΔE_s depends linearly on the width s of the exit slit. The actual adjustment of the exit slit is a competition between count rate and energy resolution. For the total-ion-yield measurements (the TOF measurements), a photon energy resolution (FWHM) of $\cong 1.7$ meV ($\cong 6$ meV) were used. Normally, the resonance $2, -1_3$ is employed for a characterization of photon resolution. It therefore serves as a benchmark for the optimization of mirror positions, the size and position of the exit slit, etc.

2.4 Time-of-flight techniques

About 40 years ago, the pulsed nature of SR emitted from electron storage rings provided the basis for the development of time-of-flight (TOF) electron spectroscopy as an efficient, but relatively low-resolution alternative to electrostatic or magnetostatic analyzers. Early TOF electron spectrometers were used for photoemission experiments on solid samples where a lower absolute energy resolution could be tolerated [51]. Since the 80's of the last century, detectors and timing electronics for TOF electron spectrometers for gas-phase experiments were developed [22, 52]. In the present dissertation, the photoelectron time spectra for studies of the PCSs and the ADPs in doubly excited helium were taken by TOF electron spectrometers, which allow to determine the kinetic energies

of various outgoing electrons. Consequently one can determine the principal quantum numbers n of the remaining electron in $\text{He}^+(n)$ and in this way n -specific PCSs and ADPs are achieved.

In the TOF technique, the kinetic energies of the photoelectrons are determined by measuring the flight times of the electrons from the interaction region to the detector, which are typically of the order of some tens to hundred nanoseconds. This method inherently relies on a timing pulse directly correlated to the SR light pulse, and a signal provided by the electron detector. The time spectra of electrons with various kinetic energies can be collected simultaneously. In order to avoid an overlap of slow photoelectrons originating from one pulse and fast photoelectrons coming from the next pulse, the time window, i.e. the pulse period, has to be long enough to ensure the arrival of the electrons with the lowest velocity. Therefore, the single-bunch mode of SR is used to match such a time window.

One advantage of a TOF spectrometer in comparison to an electrostatic analyzer is that it can collect the entire electron spectrum simultaneously. Due to this, the background noise in the time spectrum is suppressed since it is evenly distributed over the entire time spectrum; this fact greatly increases the signal-to-noise ratio for the weak structures analyzed in this work. Another advantage of the TOF technique is that, due to its simplicity and small size, more than one spectrometer can be mounted to an experimental chamber. This allows to perform angle-resolved measurements without rotating the chamber so that the available beamline can be used more efficiently. In the “ball-chamber” used for the measurements of the ADPs (see Figs. 5.2 and 5.3), more than 10 TOFs can be mounted in the dipole plane. In addition, TOF spectrometers have a high transmission for photoelectrons with low kinetic energy down to $\cong 50$ meV.

2.4.1 Time-of-flight electron spectrometer

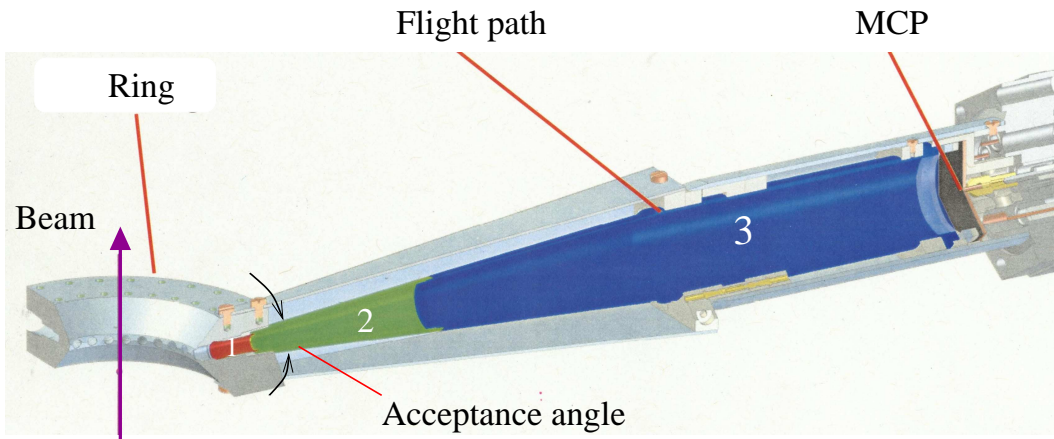


Figure 2.7: Schematic for the design of TOF electron spectrometer. The drift tube for electron flight path contains three parts marked by 1, 2, and 3, respectively. (From M. Braune)

The TOF spectrometer employed for the measurements of the ADPs is schematically

shown in Fig. 2.7; it is similar to the TOF spectrometer used in the PCS measurements. Three accelerating potentials, normally less than 2 eV, can be applied to parts 1, 2, and 3 in the drift tube that has a length of 28.1 cm. The TOF spectrometers are spatially fixed by a ring perpendicular to the beam indicated by the vertical arrow in Fig. 2.7; the acceptance angle of the TOF spectrometer is $5^\circ - 6^\circ$. To detect the electrons, a multi-channel plate (MCP) was installed at the end of the drift tube. For this particular TOF spectrometer design, the total flight distance of photoelectrons from the interaction region to the MCP is about 30.9 cm.

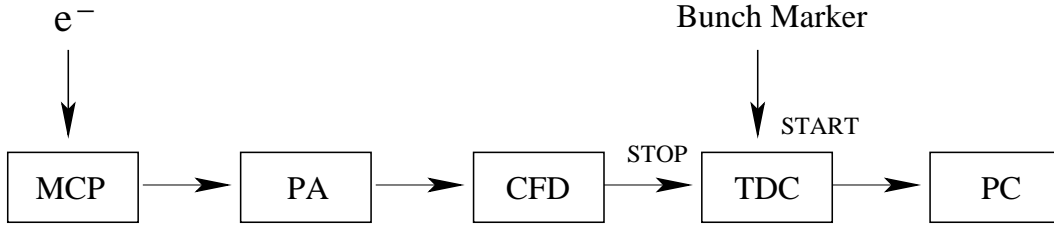


Figure 2.8: Schematic of the data-acquisition electronics.

Fig. 2.8 shows schematically the electronics used for processing the MCP pulses from one TOF analyzer. The electrons are detected by three MCPs, with diameter of $\cong 34$ mm diameter, in a Z-stack arrangement. Normally, an operating voltage of 3000 V is applied to the MCP that has a resistance of $50 - 100$ M Ω . The signals are first amplified using a preamplifier (PA) and then reach a constant-fraction discriminator (CFD), where signal noise is suppressed by setting a reasonable threshold as a trigger point. The CFD output signal is a fast timing pulse that is used for the “stop” signal for the time-to-digital-converter (TDC). The “start” signal is provided by the bunch marker that is correlated to the SR pulse. The time difference between “start” and “stop” is converted in the TDC into channel numbers, which are recorded and stored by a computer. In the single-bunch mode of BESSY II, the time window between two adjacent pulses is 800 ns. This time period represents 13385 channels, each channel having a time resolution of $\cong 60$ ps.

2.4.2 Time-to-Energy conversion

In this dissertation, the TOF photoelectron time spectra were taken at different photon energies using a step-width of 3 meV, and they have to be first converted into photoelectron energy spectra by a time-to-energy conversion in order to obtain differential cross sections (DCS). Time spectra taken directly from a TOF electron spectrometer are not linear in energy (see Eq. (2.5)) resulting in an asymmetric shape, especially for peaks with low kinetic energies; this can be seen in Fig. 2.9. Therefore, it is necessary to linearize the spectrum in energy without affecting the peak area (proportional to the number of counts). The relationship between the flight time t and the kinetic energy

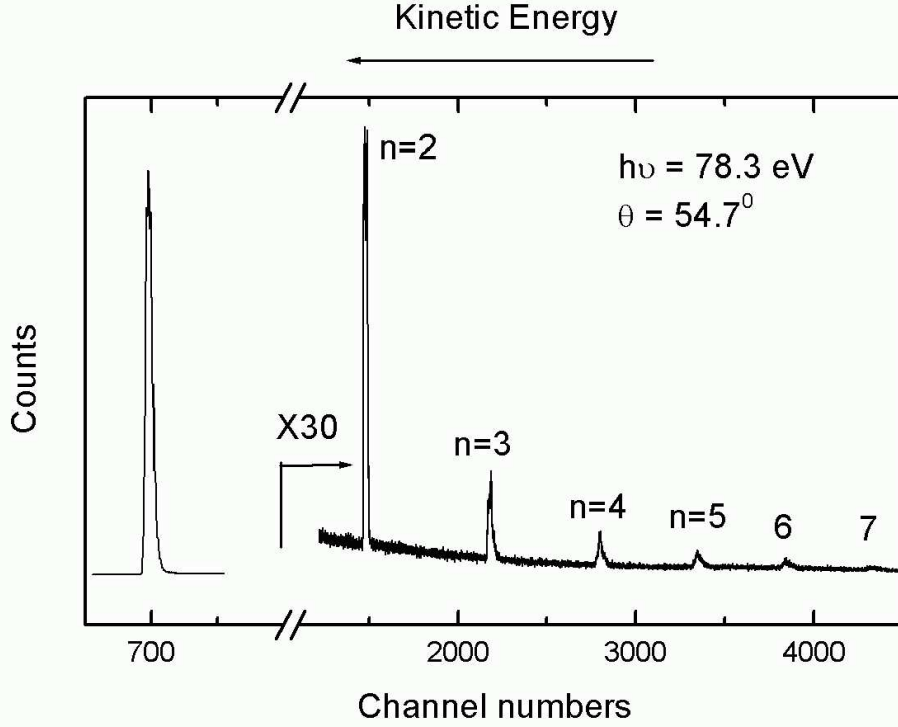


Figure 2.9: Photoelectron spectrum on the time scale taken at a photon energy of 78.3 eV. n indicate the decay channels that lead to a final state $\text{He}^+(n)$. The channel numbers are proportional to the flight time of the photoelectron in contrast to the kinetic energy, which is increasing in the opposite direction.

E_{kin} of an electron under field-free conditions is given by

$$E_{kin} = \frac{1}{2}m_e v^2 = \frac{m_e l^2}{2t^2}, \quad (2.5)$$

with m_e being the electron mass and l the distance from the interaction region to the detector. In order to improve the transmission, in particular for slow electrons, the spectra were measured with an accelerating voltage (E_{pot}), and thus Eq. (2.5) cannot be applied without precise knowledge of all the electrical potentials in the analyzer. An empirical expression has to be used for the relation between kinetic energy and the corresponding channel. Considering this correspondence between a channel in the time spectrum (ch) and the flight time (t) ($t \propto (\text{prompt} - ch)$), one can rewrite Eq. (2.5) as

$$E_{kin}(ch) - E_{pot} \propto \frac{1}{(\text{prompt} - ch)^2}. \quad (2.6)$$

Here the prompt describes a peak in the time spectrum that originates from photons scattered from the gas target. Due to the high velocity of light, the flight time from the interaction center to the detector can be neglected and the corresponding peak can be used as zero on the time axis. One can fit this formula to some peaks with known kinetic energies in the time spectra. With the fit result, one can transform a time spectrum into an energy spectrum by a point-to-point transformation. A precise time-to-energy

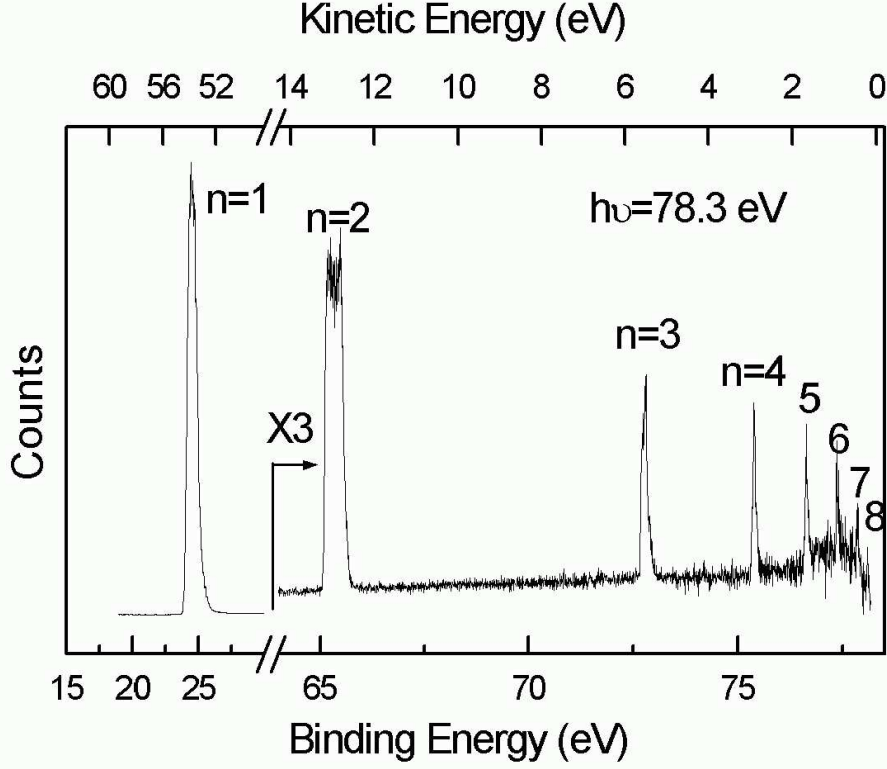


Figure 2.10: Photoelectron spectrum on the energy scale taken at a photon energy of 78.3 eV and obtained from the spectrum on the time scale in Fig. 2.9 by time-to-energy conversion. The corresponding kinetic energies are marked on the upper x-axis.

conversion is difficult to obtain for low-energy electrons because the paths of the electrons are strongly influenced by residual magnetic fields. As a result, the kinetic-energy axis cannot be determined accurately by a simple fit based on Eq. (2.6). It is necessary to use a polynomial fit function to obtain a complete and accurate time-to-energy conversion. In this dissertation, the electrons with kinetic energies down to 0.3 eV were taken in the measurements of the PCSs and the ADPs. Only high-quality fit curves can guarantee the conservation of the spectra in the time-to-energy conversion procedure, in particular for low-count peaks with low kinetic energies. The high accurate time-to-energy conversion can convert the peaks, corresponding to one of final ion states $\text{He}^+(n)$ with various photon energies, to an exactly the same binding energy scale. Then, the DCSs are obtained automatically by the Sunny program [53] by evaluation of the counts in an energy window on the binding energy axis containing these peaks. Otherwise, the peaks in the energy spectra (as a function of binding energy) can experience a shift with respect to different photon energies, which causes the loss of counts during the extraction of the DCSs.

As an example, the spectrum taken at a photon energy of 78.3 eV at $\theta = 54.7^\circ$ was converted from the time scale given in Fig. 2.9 to the energy scale presented in Fig. 2.10. After conversion, the peaks become symmetric and their widths as well as relative intensities vary in the spectrum on the energy scale.

The kinetic-energy resolution, $\Delta E/E$, of an electron TOF spectrum is given by [54]

$$\frac{\Delta E}{E} = \sqrt{\left(\frac{2\Delta t}{t}\right)^2 + \left(\frac{2\Delta l}{l}\right)^2 + \left(\frac{2\Delta\lambda}{\lambda}\right)^2}; \quad (2.7)$$

it depends on the relative uncertainties in the wavelength ($2\Delta\lambda/\lambda$), the flight time ($2\Delta t/t$), and the electron flight-path length ($2\Delta l/l$). The latter is determined by the size of the interaction region, typically 100-1000 μm , the analyzer acceptance angle (5°), and the variation in the length of flight path. Due to the small acceptance angle, the total variation of the electron flight length should be less than 3 mm. In summary, the kinetic-energy resolution is estimated to be about 2% of the kinetic energy. For a detailed discussion of electronics, see Ref. [54].

2.4.3 Transmission function and analyzer efficiency

The slow electrons are lost more easily during the drift process towards the detector. This can result from residual magnetic or electric fields inside the chamber. In order to effectively detect very slow electrons, accelerating voltages are applied to the drift tube. However, even for this case, the counts for slow electrons may decrease dramatically, in particular for electrons with kinetic energies below 1 eV. Therefore, a transmission correction has to be applied in order to convert the counts for slow electrons into partial relative cross section.

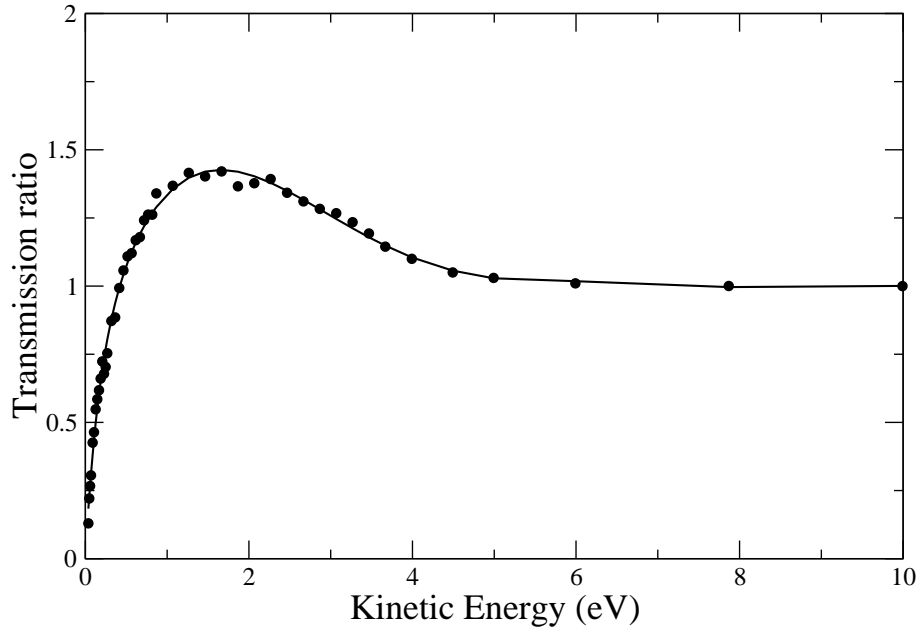


Figure 2.11: Transmission function as a function of photoelectron kinetic energy. Solid points are our experimental data for the satellite $n = 2$ of helium; the solid line is the fit to the function given in Eq. (2.8).

Fig. 2.11 displays a typical transmission correction function for a TOF electron spectrometer derived from the fit to our experimental cross section for the satellite $n = 2$ of

helium. Experimental data are shown as solid points below the kinetic energy of 10 eV. Here, the transmission correction function employed for the fit has the form

$$y = p_1 \cdot \exp(-x/p_2) + p_3 \cdot x + p_4 \cdot x^2 + p_5 \cdot x^3, \quad (2.8)$$

where p_1 to p_5 are free fit parameters. y and x represent the transmission correction factor and the kinetic energy, respectively. After determining the parameters in Eq. (2.8) by a fit, this function can be employed to correct the cross sections for any satellite with the same kinetic energy. Above kinetic energies of 10 eV, no transmission correction is performed, i.e. the transmission correction factor for photoelectrons with high kinetic energies is assumed to be unity.

For a measurement of the β parameter, besides transmission correction, the TOF efficiency has to be taken into account. Due to differences in TOF spectrometer design, the potential of MCP, and the electronics, TOF efficiencies could vary within a factor of 2. For helium spectra, the efficiency factors for various TOFs can be extracted from a comparison of the $1s$ lines. This is due to the following facts: first, the kinetic energy of photoelectron from the $1s$ line is quite high ($E_{kin} > 50$ eV in the present region concerned) and, consequently, these fast electrons are not affected by the transmission or underlying magnetic fields; second, the efficiency of a TOF spectrometer is assumed to be independent of the kinetic energy of the photoelectrons. In addition, the angular distribution parameter $\beta_{1s} = 2$ has to be taken into account. For 90° TOF in the absence of $1s$ peak, one can determine its efficiency factor by a photoelectron line having a $\beta \neq 2$ such as $\text{Ne}^+ 2p$ emission line [55].

Chapter 3

Doubly excited resonances of helium

By absorbing one photon, one can reach from ground-state of helium a final state with one electron in the continuum and the second one in the ground or excited state of the remaining ion. These final states can be reached via two different paths as shown in Fig. 3.1. The first path is the direct photoionization channel with excitation, i.e. one electron is promoted to the continuum and the second one is excited to a higher orbit. This process can be described by

$$\text{He}(1s^2) \ ^1S^e + h\nu \rightarrow [\text{He}^+(nl) + e^-] \ ^1P^o. \quad (3.1)$$

Here n and l are principal quantum number and orbital angular momentum quantum number, respectively. In the second path, both electrons are first excited to a discrete state, which subsequently decays via autoionization. This process can be described by

$$\text{He}(1s^2) \ ^1S^e + h\nu \rightarrow \text{He}^*(N, K_{n'}) \ ^1P^o \rightarrow [\text{He}^+(nl) + e^-] \ ^1P^o, \quad (3.2)$$

where $N, K_{n'}$ is a simplified classification scheme. N, n' , and K are approximate radial and angular quantum numbers, respectively; and a detailed discussion will be given

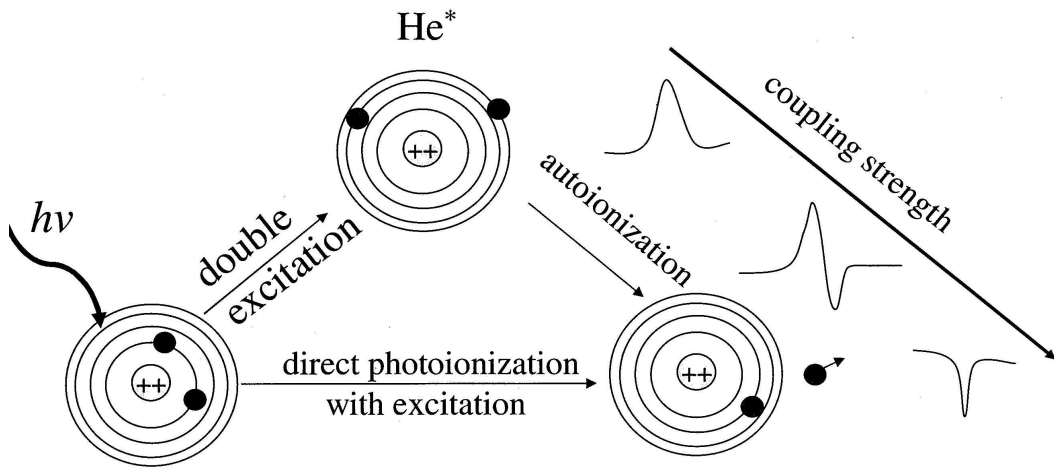


Figure 3.1: Schematic representation of photoionization following excitation from the $^1S^e$ ground state of helium to a $^1P^o$ final state.

in Sect. 3.2. In the energy domain, these two processes cannot be distinguished by experiment and, therefore, according to the interference of these two decay paths, Fano profiles are observed in the spectra. Three different cases (weak, medium, and strong) for the dependence of the lineshape of the resonance on the coupling strength are shown in Fig. 3.1, that will be discussed together with the Fano parameter q in Sect. 3.1.1. The two paths mentioned occur on different time scales and one can distinguish them in the time domain. Sub-fs extreme ultraviolet pulses and attosecond streaking techniques can trace the buildup of a Fano resonance in the time domain; the feasibility of such experiments has been analyzed theoretically [56].

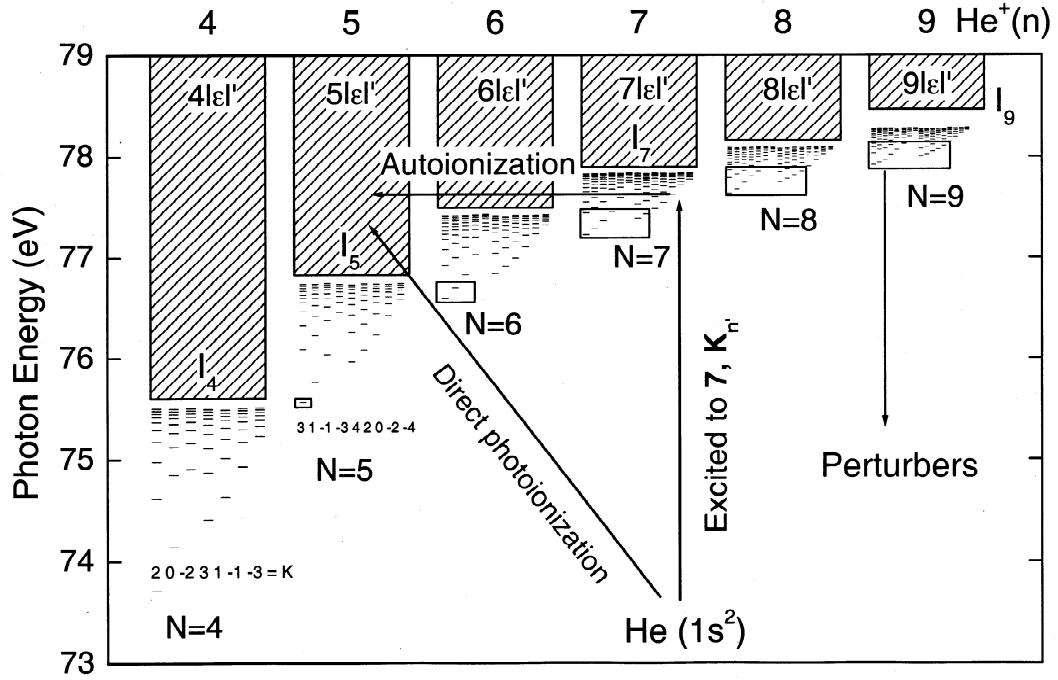


Figure 3.2: Energy diagram of the $1P^o$ double-excitation resonances below the SITs I_4 to I_9 in He with energies taken from Ref. [31]. $2N - 1$ Rydberg series indicated by some horizontal lines are converged to single ionization threshold (SIT) I_N . The lines with arrows represent different paths which lead to the final continuum states with the remaining electron in $\text{He}^+(n)$ states with $n = 1, \dots, 6$. The resonances in the boxes are the perturbers.

Fig. 3.2 shows the energy level scheme of double-excitation resonances in helium below the single ionization thresholds (SIT) I_4 to I_9 . Two different paths leading to the final continuum states, namely autoionization and direct photoionization with excitation, are indicated in this figure; they were discussed above, see Fig. 3.1. As marked on the upper x-axis in this figure, the doubly excited states $N, K_{n'}$ ($N = 7$) can decay to the final continuum states with the remaining electron in the $\text{He}^+(n)$ states with $n = 1$ to 6. Observably $N - 1$ channels with $n = 1$ to $N - 1$ are open if one scans spectra at photon energies between I_{N-1} and I_N , i.e. in this energy region $N - 1$ satellites can be resolvable from channel-resolved measurements such as experimental PCSs. These different decay channels can be distinguished by the kinetic energies of the corresponding photoelectrons

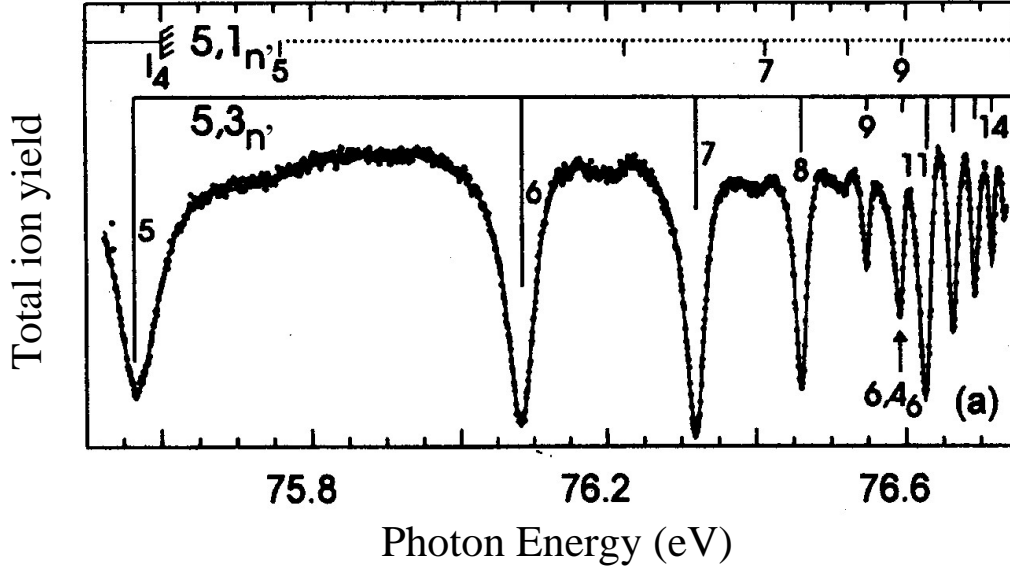


Figure 3.3: Experimental total cross sections below the SIT I_6 . The position of the perturber $6, 4_6$ is indicated by an arrow. The figure is taken from Ref. [30]

that correspond to the PCSs, σ_n .

The most interesting feature is the occurrence of perturbers, which are indicated by boxes in Fig. 3.2. Perturbers are low-lying resonances of a Rydberg series below I_N that lie energetically in the region of high-lying resonances below I_{N-1} . Figure 3.2 displays the first perturber located exactly at I_4 , but more and more perturbers appear in the Rydberg series below higher single-ionization thresholds. The appearance of perturber states dramatically modulates Fano profiles of resonances that converge towards a lower ionization threshold. Total cross sections below the SIT I_6 given in Fig. 3.3, as an example, show how the spectrum is affected by the perturber $6, 4_6$, which is indicated by a vertical arrow. Clearly, in the region of the perturber, the resonances of Rydberg series $5, 3_{n'}$ are significantly varied. In this dissertation, we are concerned with the energy region above the SIT I_8 , where a large number of perturbers cause the spectra to fluctuate and to become complicated. Therefore, one expects to observe Ericson fluctuations [26] in the spectra, which describes the fact that it is impossible to identify each resonance due to strong overlaps of the states. Ericson fluctuations, originally observed in nuclear physics, have become quantum signatures of chaos in atomic system (discussed later).

3.1 Parameterizations of resonance profiles in cross sections

In principle, one can calculate cross sections and ADPs with Eq. (1.23) and Eq. (1.24), but these complicated formula cannot be used directly for the analysis of experimental

data. Therefore, a parameterization of resonance profiles can clarify the physical picture of a resonance and allows one to perform a more quantitative comparison between experimental results and calculations. In the following subsections, we shall discuss the parameterizations of resonance profiles in the TCS, the PCS, and the ADP, that will be used in the fit analysis of our data.

3.1.1 Fano profiles for the total cross sections

The resonances in the absorption spectra exhibit pronounced Fano profiles that originate from an interference between direct photoionization and indirect photoionization channels as discussed before. This leads to Fano profiles of the form [20, 57]:

$$\sigma_T(E) = \sigma_a \frac{(q + \epsilon)^2}{1 + \epsilon^2} + \sigma_b, \text{ with reduced energy } \epsilon = 2 \frac{E - E_r}{\Gamma}. \quad (3.3)$$

Here, E_r is the resonance energy and Γ the natural width given by the decay rate of the autoionization resonance. The Fano parameter q represents the discrete/continuum mixing strength, i.e. coupling strength. With $|i\rangle$, $|\nu\rangle$, and $|f\rangle$ describing the initial, intermediate (discrete state), and final continuum state, respectively, the linewidth can be written as

$$\Gamma = 2\pi |\langle f|V|\nu\rangle|^2, \quad (3.4)$$

where V represents the Coulomb interaction. σ_a and σ_b represent the non-resonant background cross sections for transitions to continuum states that interact or do not interact, respectively, with discrete autoionization states [57]. Therefore, σ_a is affected by the interaction whereas σ_b is constant. The Fano parameter q is given by

$$q = \frac{\langle \nu|r|i\rangle}{\pi \langle \nu|V|f\rangle \langle f|r|i\rangle}, \quad (3.5)$$

which represents the ratio of the dipole matrix element of a transition to a discrete state to that of a transition to the continuum, which interacts with the discrete state. As demonstrated in Fig. 3.1, for the case that the coupling strength between the final state $|f\rangle$ and the discrete state $|\nu\rangle$ is very weak, the value for q in Eq. 3.5 becomes large and a Lorentz lineshape is observed in the cross section; for a strong coupling strength, q is close to zero and one can see a window dip; for all other cases of the coupling strength, the variation in the cross section caused by a resonance is described by a Fano-like lineshape. If q is negative, the minimum in the absorption cross section occurs on the high-energy side of the line and otherwise on the low-energy side, as can be seen in Fig. 3.4 by the simulations to Eq. (3.3).

By setting $\sigma_a/(\sigma_a + \sigma_b) = \rho^2$ and $\sigma_T^0 = \sigma_a + \sigma_b$, the σ_T in Eq. (3.3) can also be written as [57, 58]

$$\sigma_T = \sigma_T^0 \left(\rho^2 \frac{(q + \epsilon)^2}{1 + \epsilon^2} + 1 - \rho^2 \right). \quad (3.6)$$

Here, ρ^2 is the fractional part of the TCS that interacts with the resonance [58] and it is called correlation parameter. σ_T^0 represents the off-resonance TCS.

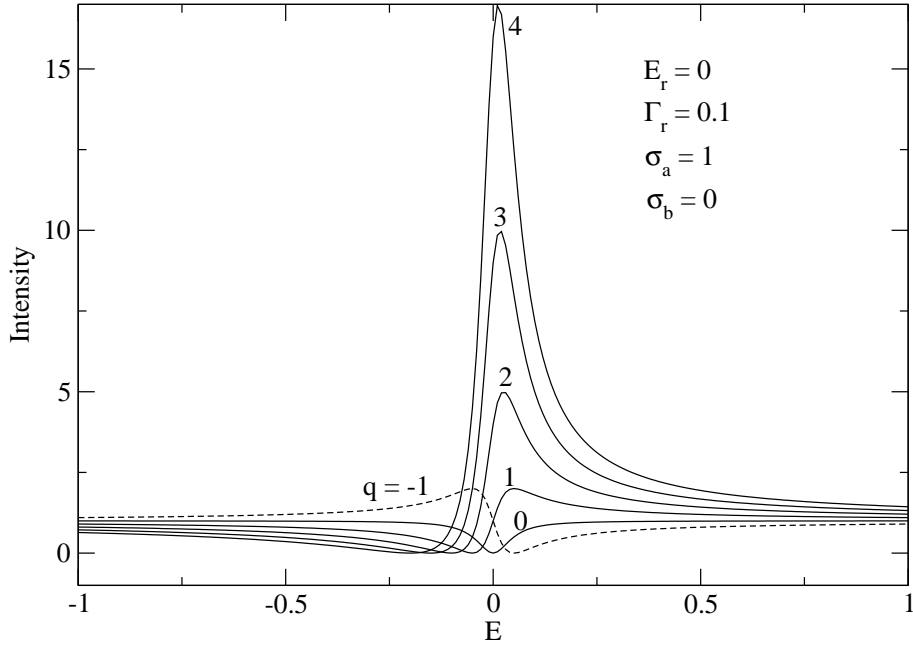


Figure 3.4: Simulations of Fano lineshapes as a function of q for various values of $q = -1, 0, 1, 2, 3$, and 4 . The values of the other parameters used in the simulations are given in the figure.

3.1.2 Starace's formula for partial cross sections

In Ref. [59], Starace used the observed channels to describe the resonance profiles in the PCS. A PCS denoted by P can be described analytically by

$$\sigma_P = \sigma_P^0 + \frac{\sigma_P^0}{1 + \epsilon^2} \{ 2\epsilon(q\text{Re}\langle\alpha\rangle_P - \text{Im}\langle\alpha\rangle_P) - 2q\text{Im}\langle\alpha\rangle_P - 2\text{Re}\langle\alpha\rangle_P + (q^2 + 1)\langle|\alpha|^2\rangle_P \}. \quad (3.7)$$

Here, σ_P^0 is the PCS in the absence of a resonance and the second term describes the Fano-like lineshape of the resonance in σ_P . α is the Starace parameter [59] and represents the fraction of the dipole amplitude. Setting $C_1 = q\text{Re}\langle\alpha\rangle_P - \text{Im}\langle\alpha\rangle_P$ and $C_2 = 1 - 2q\text{Im}\langle\alpha\rangle_P - 2\text{Re}\langle\alpha\rangle_P + (q^2 + 1)\langle|\alpha|^2\rangle_P$, the above equation can be written as

$$\sigma_P = \frac{\sigma_P^0}{1 + \epsilon^2} \{ \epsilon^2 + 2\epsilon C_1 + C_2 \}. \quad (3.8)$$

This equation depends on only *two* independent linear combinations, C_1 and C_2 , of the *three* parameters $\langle|\alpha|^2\rangle_P$, $\text{Re}\langle\alpha\rangle_P$, and $\text{Im}\langle\alpha\rangle_P$. As a consequence, one may only determine C_1 and C_2 by fitting Eq. (3.8) to the experimental data, but $\langle|\alpha|^2\rangle_P$, $\text{Re}\langle\alpha\rangle_P$, and $\text{Im}\langle\alpha\rangle_P$ cannot be determined from the fit. Interestingly, one may note that the formula for describing the resonances in the PCS given in Eq. (3.8) has the same mathematical structure as the Fano formula (Eqs. (3.3) and (3.6)) for the TCS. Therefore, it is possible to describe the PCSs by the Fano formula, but in this case q as well as C_1 and C_2 represent only effective parameters without deeper physical meaning. The relation between these parameters is [60]

$$C_1 = \rho^2(q^2 - 1) + 1 = \frac{\sigma_a q + \sigma_b}{\sigma_b}$$

$$\begin{aligned}
C_2 &= 2q\rho^2 = \frac{\sigma_a}{\sigma_b} \\
\sigma_P^0 &= \frac{\sigma_T^0}{\rho^2} = \sigma_b.
\end{aligned} \tag{3.9}$$

The Fano formula given in Eqs. (3.3) and (3.6), together with Eq. (3.8), can be used to fit the experimental TCSs or PCSs.

3.1.3 Kabachnik's formula for the angular distribution parameters

The transition matrix elements in Eq. (1.24), which characterize excitation and autoionization decay, have to be parameterized, so that they can be used in the fit analysis of the experimental data. To this purpose, Kabachnik [46] parameterized the ADPs β given in Eq. (1.22) in the following way:

$$\begin{aligned}
\beta &= -2 \frac{X\epsilon^2 + Y\epsilon + Z}{A\epsilon^2 + B\epsilon + C} \\
&= -2 \frac{X}{A} \cdot \frac{\epsilon^2 + \frac{Y}{X}\epsilon + \frac{Z}{X}}{\epsilon^2 + \frac{B}{A}\epsilon + \frac{C}{A}},
\end{aligned} \tag{3.10}$$

with

$$\begin{aligned}
A &= \frac{\sigma_a + \sigma_b}{4\pi} \\
B &= \frac{2q\sigma_a}{4\pi} \\
C &= \frac{\sigma_a q^2 + \sigma_b}{4\pi}.
\end{aligned} \tag{3.11}$$

The parameters X , Y , and Z are related to the transition amplitudes and the phase shifts given in Eq. (49) in Ref. [46]. They are considered to be slowly varying functions of energy and may be regarded as correlation constants in the vicinity of a resonance. With the off-resonance value $\beta_0 = -2X/A$ and the relations given in Eq. (3.11), one can write Eq. (3.10) as

$$\beta = \beta_0 \frac{(\epsilon^2 + \frac{Y}{X}\epsilon + \frac{Z}{X})(\sigma_a + \sigma_b)}{\sigma_a(\epsilon + q)^2 + \sigma_b(\epsilon^2 + 1)}. \tag{3.12}$$

With the new parameters $F = Y/X$ and $G = Z/X$, Eq. (3.12) becomes

$$\begin{aligned}
\beta &= \beta_0 \frac{\epsilon^2 + F\epsilon + G}{\sigma_T} \cdot \frac{\sigma_a + \sigma_b}{\epsilon^2 + 1} \\
&= \beta_0 \frac{\epsilon^2 + F\epsilon + G}{\rho^2(\epsilon + q)^2 + (1 - \rho^2)(\epsilon^2 + 1)}.
\end{aligned} \tag{3.13}$$

In the measurements, PCSs together with other DCSs are measured, and these data are used to derive the corresponding ADPs. Due to possible fluctuations caused by other

DCSs, the PCSs become more reliable with respect to the ADP. Therefore, with Eq. 3.13, a parallel fit for β is recommended by sharing the two parameters q and ρ^2 with the PCS, but not F , G , and β_0 . We shall apply this procedure to our ADP data in the near future.

One can also simply write the ADP in Eq. (3.10) as

$$\beta = \beta_0 \frac{\epsilon^2 + a_1\epsilon + b_1}{\epsilon^2 + a_2\epsilon + b_2}. \quad (3.14)$$

In this case, a_1 , b_1 , a_2 , and b_2 can also be regarded as correlation constants in an isolated resonance. During a fit process, one has to take into account the conditions $b_2 = (q^2\sigma_a + \sigma_b)/(\sigma_a + \sigma_b) > 0$ and $a_2 = (2q\sigma_a)/(\sigma_a + \sigma_b)$. Indeed, according to the large number of parameters (5 independent parameters in addition to the Fano parameters q , Γ , and E_r) in Eq. (3.14), it is quite difficult to extract them correctly from a fit to experimental data, particularly in case of overlapping resonances. In the vicinity of a resonance, the terms in the numerator and denominator of Eq. (3.10) change differently, so that their extrema are at different excitation energies and, as a result, β can vary rapidly. From simulations performed with Eq. (3.14), the variations in β show strong dependence on the parameters in the denominator.

3.2 Classification schemes for doubly excited resonances of helium

In this dissertation, we introduce two different classification schemes to describe doubly excited resonances in helium. The first is based on a molecular adiabatic description of helium, which uses the quantum numbers n_λ , n_μ , and m . These quantum numbers are equivalent to the approximate quantum numbers $N(K, T)_{n'}^A$ which were derived from group theory by Herrick and Sinanoğlu [23, 61]. In this dissertation, both classification schemes will be employed to understand the dynamics of doubly excited resonances in a two-electron system. The transformations between molecular quantum numbers and Herrick's approximate quantum numbers will also be presented in this section.

3.2.1 Molecular adiabatic approximation

In order to fully understand the decay dynamics of doubly excited states, Feagin and Briggs [24] introduced in 1986 an adiabatic approximations similar to the Born-Oppenheimer approximation for H_2^+ , but with a reversed role of electrons and nuclei (see Fig. (3.5)).

The most important feature of the molecular adiabatic approximation is the fact that the two-center Hamiltonian is separable in prolate spheroidal coordinates that are plotted in Fig. 3.6. In this case, individual resonances are obtained by calculating vibrational eigenstates according to the Schrödinger equation,

$$\left(-\frac{\partial^2}{\partial R^2} + V_{n_\lambda, n_\mu, m} - E_{n'} \right) f_{n'}(R) = 0, \quad (3.15)$$

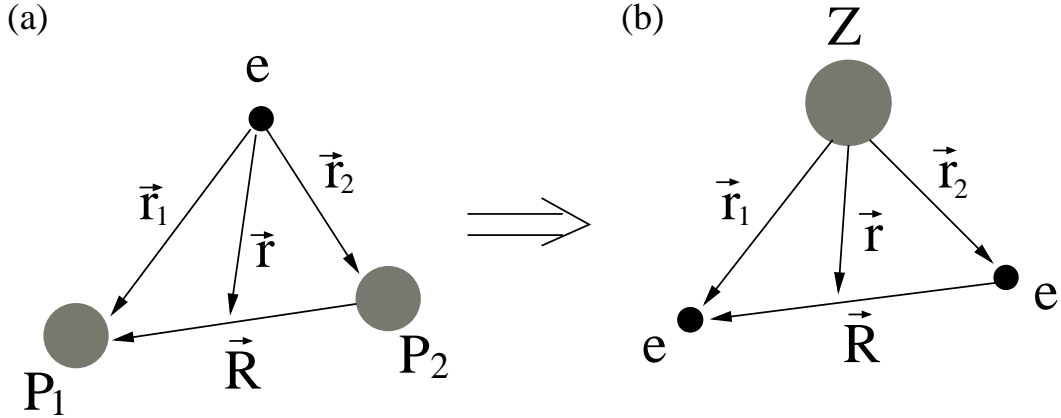


Figure 3.5: (a) Schematic of H_2^+ and (b) of the helium atom with reversed roles for the electrons and nucleus. \vec{r}_1 and \vec{r}_2 are the two possible distances between electrons and nuclei. \vec{r} is the distance between electron (nucleus) and the center of two nuclei (electrons). P and e represent the proton and electron, respectively, and \vec{R} is the distances between the two identical particles.

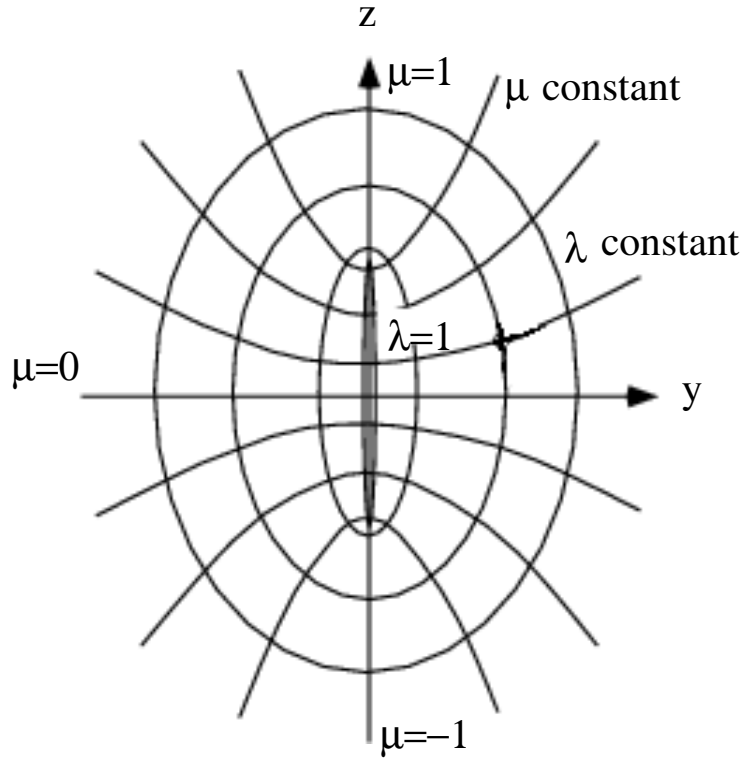


Figure 3.6: Schematic of the prolate coordinates λ and μ .

where R is the distance between the two identical particles, i.e. the electrons in case of helium. The quantum numbers n_λ and n_μ count the nodes along the respective coordinates λ and μ . m is the angular quantum number corresponding to the rotation angle along the Z axis in Fig. 3.6. The potentials $V_{n_\lambda, n_\mu, m}$ lead to a set of adiabatic avoided-crossing potential curves, which represent Rydberg series. n' are vibrational energies in these potential curves, but in doubly excited states they specify the excitation

of one electron to a Rydberg series, i.e. they represent the index of a Rydberg series. So far, a complete classification of doubly excited state can be described by quantum numbers n_λ , n_μ , m , and n' .

3.2.2 Herrick's classification schemes

The classification scheme $N(K, T)_{n'}^A$ [23, 61], which is identical to the molecular scheme with quantum numbers n_λ , n_μ , and m , is often employed to identify an isolated doubly excited resonance with N and n' , respectively, standing for the ionization threshold of a given channel and the running index of the considered Rydberg series. In an independent particle picture, $N(n')$ may be understood as the principal quantum number of the inner (outer) electron; K is one of the angular-correlation quantum numbers and proportional to the average value of $r_1 \cos \theta_{12}$, where r_1 refers to the inner electron and θ_{12} is the angle between the two electrons. T , the second angular-correlation quantum number, represents the relative orientation between the orbitals of the two electrons, which is equivalent to quantum number m in molecular approximation. A is called the radial correlation quantum number, which reflects a symmetry (the wave function of $A = +1$ states has an antinode and $A = -1$ states with a node) with respect to the x-y-plane ($\mu = 0$, i.e. $r_1 = r_2$) in Fig. 3.6. Close to the double-ionization threshold (N and n' are quite large), one obtains

$$K \rightarrow -N \langle \cos \theta_{12} \rangle \quad (3.16)$$

from

$$\langle \cos \theta_{12} \rangle \rightarrow -\frac{K}{N} + \frac{N^2 - 1 + K^2 - T^2 + 2ll'}{2Nn'}, \quad (3.17)$$

where l (l') is the orbital angular quantum number for the inner (outer) electron, respectively. For a given L and N , the ranges for K and T are given as follows [23]:

$$\begin{aligned} T &= 0, 1, \dots, \min(L, N-1), \\ \pm K &= N - T - 1, N - T - 3, \dots, 1(\text{or } 0). \end{aligned} \quad (3.18)$$

For $^1P^\circ$ double-excitation resonance of helium, T is limited to 1 and 0 and K has $2N-1$ values below a given ionization threshold I_N . $N, K = N-2$ is the principal Rydberg series, which carries most intensity in the spectra, with resonances that have larger line widths.

Herrick's quantum numbers $N(K, T)_{n'}^A$ correspond to the molecular quantum numbers $[n_\lambda n_\mu m]_{n'}$ by the following relations:

$$\begin{aligned} \text{molecular} & & \text{Herrick} \\ n_\lambda &= & \frac{1}{2}(N - K - 1 - T) \\ [n_\mu/2] &= & \frac{1}{2}(N + K - 1 - T) \\ m &= & T \\ (-1)^{n_\mu} & (=) & A. \end{aligned} \quad (3.19)$$

Here, $N = n_\lambda + [n_\mu/2] + m + 1$ and $K = n_\lambda - [n_\mu/2]$. The notation $[n_\mu/2]$ stands for the closest integer lower than $n_\mu/2$; In the two-center adiabatic approach, the fact that $A = 0$ does not occur is implied in the last equality in parentheses of Eq. (3.19) (for details see Ref. [31]). The approximate quantum numbers $[n_\lambda n_\mu m]_{n'}$ and $N(K, T)_{n'}^A$ imply the nodal structure of the wave function, which in turn leads to the propensity rules of radiative and non-radiative transitions (see Sect. 5.3.2).

Part II

Experimental photoexcitation and autoionization spectroscopy of helium

Chapter 4

Photoionization cross sections in the ion yield

Due to its simplicity, the three-body system helium, in its doubly excited states, has become a highly exciting atom for the study of quantum chaos. Quantum chaos can be considered as the behavior of a quantum system whose classical counterpart behaves chaotic. Doubly excited helium approaches the semiclassical limit, i.e. $\hbar \rightarrow 0$, in the region close to the double-ionization threshold (for details see App. A). The classical counterpart of the helium atom, the classical three-body system, is a nonintegrable system, i.e. it can behave chaotic. Therefore, one expects quantum chaos to emerge in the spectra of doubly excited resonances in He close to the double-ionization threshold. In other words, close to double-ionization threshold, the signatures of classical mechanics in doubly excited helium will be magnified by the observation of quantum-chaotic spectra. Richter *et al.* [28] showed that classical helium exhibits a mixed phase space with regular and chaotic regions by using the Poincaré section of the Wannier ridge (explained later). Chaotic dynamic in classical helium is independent of the total energy. However, the spectra in doubly excited helium carry a transition (reflecting strong electron correlations) to chaotic behavior while the photon energy is increased close to the double-ionization threshold. The strong electron correlations in this two-electron atom are reflected in a set of new approximate quantum numbers $N, K_{n'}$ instead of traditional quantum numbers like l . These approximate quantum numbers work quite well, particularly in the low energy region. In the region of high doubly excited states, an increasing number of perturbers render the spectra very complicated and fluctuating. As a consequence, the approximate quantum numbers $N, K_{n'}$ start to dissolve. At the double-ionization threshold, the helium atom may be described by classical mechanics. From this point of view, one can assume that there might not be enough good quantum numbers to describe the spectra close to double-ionization threshold of helium. In the previous work of our group [18], statistical studies of nearest-neighbor spacings (NNS) of energy levels carried out, with the results that the onset of a transition to quantum chaos in the region below the SIT I_9 could be identified. From the studies presented in this dissertation, we shall see that the transition region from integrability to full chaos in

$^1P^o$ helium is much larger, in agreement with the recent findings for $^1S^e$ doubly excited helium [19].

So far, most measurements of TCSs of doubly excited resonances in helium were limited to the energy region below the SIT I_9 [18, 30, 62]. Many advanced theoretical methods [29, 31, 32, 33, 63] have been developed during last 20 years. However, these theoretical studies were performed only in the region below the SIT I_9 as well. In this chapter, we shall present our recent experimental progress on the TCS up to the SIT I_{15} . It is worthwhile to mention here that very recently state-of-the-art complex-rotation calculations for the TCS in three-dimensional helium by our cooperation partner D. Delande (Universite Pierre et Marie Curie, Paris) have reached the SIT I_{17} [27]; they are confirmed very well up to I_{15} by the present measurements. In this part, we shall first discuss the approximate quantum numbers $N, K_{n'}$ by using theoretical results and then study statistical properties of the energy levels, Fano parameters q , and linewidths of the resonances in doubly excited helium. Preliminary statistical studies for this atom displayed interesting precursor quantum signatures of chaos. Note that detailed statistical studies have to be performed predominantly with theoretical data due to the extremely low intensities of most of the Rydberg series, which give rise to the situation that only a small fraction of the doubly excited states can be observed experimentally.

4.1 Wigner distribution and Poisson distribution for energy levels

There are two different types of motion in classical mechanics: the regular motion of integrable systems and the chaotic motion of non-integrable systems. To distinguish these two motions, one may have a look at a bundle of trajectories in the phase space originating from a very narrow cloud of starting points. In the chaotic case, the distances between any of two trajectories in phase space increase exponentially in time. For a regular motion, these distances may grow in a power of time, but never exponentially. A simple example for classical integrable system, given in Fig. 4.1, is given by a one-dimensional accelerated motion with constant accelerations. X and P_X represent the spatial coordinate and the corresponding momentum of a particle, respectively. Using different values of acceleration for the calculation of the two trajectories, the distances, $d(t_i)$, between two trajectories in phase space increase in t^2 , as can be seen in Fig. 4.1. In contrast, the distances between two trajectories grow linearly or remain constant in time if one varies the initial velocities or the initial positions of the trajectories, respectively. There are no possibilities to change the initial conditions so that one obtains an exponential increase of $d(t_i)$ in this integrable case. Therefore, the “exponential sensitivity” is the typical character for a classical chaotic behavior. When turning to quantum mechanics, the classical description of the exponential sensitivity to the initial conditions cannot be used any more to characterize quantum chaos. One reason is that one cannot directly observe quantum chaos in phase space due to the uncertainty principle in quantum me-

chanics. However, this results in one possibility to study quantum chaos in the phase space of its classical counterpart. A second reason is given by the fact that the wave function $\Psi(t)$ in Schrödinger's wave equation can always be calculated uniquely, and it is of a simple periodic form in t , i.e. $\Psi = \Psi_0 \exp(\frac{i}{\hbar} Et)$. This means that the exponential sensitivity in time is “suppressed” in the wave function of a quantum chaotic system. Nevertheless, most researchers agree that the deterministic features of quantum chaos should be manifested in some ways in the quantum observables such as the energy levels, line widths, and Fano parameters q of resonances in doubly excited helium.

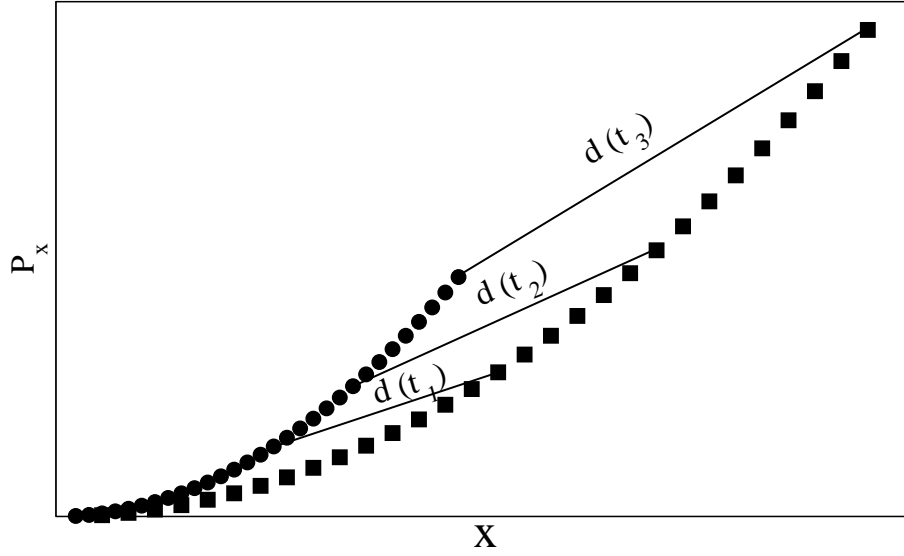


Figure 4.1: Phase space for one-dimensional accelerated motions with constant accelerations. Two trajectories that are obtained using different values of acceleration are plotted by filled circles and filled squares. The solid lines represent the distances between these two trajectories at three different times.

This raises the question how quantum chaos is manifested in the spectra. One typical manifestation is the spacing of energy levels, which will be discussed in the following. According to Heisenberg, the operators of quantum mechanics can be represented by matrices. It is then natural to conjecture that the observables of a chaotic quantum system should be represented by random matrices, i.e. the energy levels in a chaotic quantum system can be described as random elements of matrices. Some conditions based on very basic principles of physics are assumed for matrices, like the invariance of the probability density for the Hamiltonian under orthogonal transformation. Besides that the matrix elements described by the Hamiltonian must be uncorrelated. According to the invariance and the uncorrelation of the Hamiltonian, the probabilities of Hamiltonian elements are of Gaussian form, and the statistical properties of the nearest-neighbor spacings S (NNS) of energy levels are given by the Wigner distribution

$$P_W(S) = \frac{\pi}{2} S \exp(-\frac{\pi}{4} S^2). \quad (4.1)$$

The derivation of the Wigner distribution, given in Eq. (4.1), on the basis of random matrix theory [64, 65] is described in App. B; this theory was developed in the nineteen

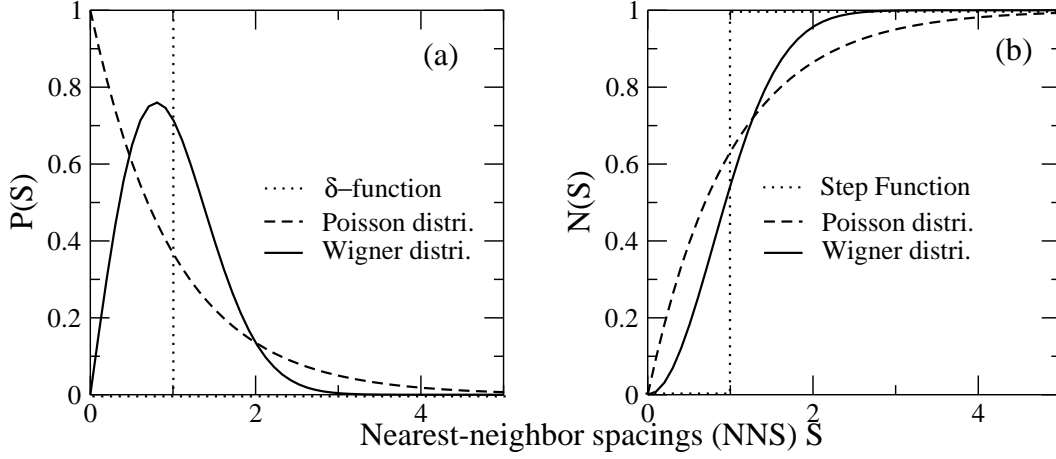


Figure 4.2: Probabilities $P(S)$ (a) and integrated probabilities $N(S)$ (b) as a function of the nearest-neighbor spacings (NNS) S . Solid lines and dashed lines represent Wigner distribution and Poisson distribution, respectively. Dotted lines in (a) and (b) represent a δ -function and a step function, respectively.

fifties and sixties in order to understand the distribution of energy levels in nuclei. Note that the spacings S are calculated from effective quantum numbers, which are obtained from the resonant energies E_r with the formula

$$\mu_N(E) = \sqrt{\frac{\mathcal{R}}{I_N - E_r}} \quad , \quad (4.2)$$

where \mathcal{R} is the Rydberg constant. A level density in the scaled spectra is independent of photon energy.

In the spectra of an integrable system, the most probable spacing between resonances that belong to different independent Rydberg series can be zero, since these energy levels are uncorrelated. The probability distribution of the NNSs for this case is predicted to be a Poisson distribution

$$P_P(S) = \exp(-S) \quad (4.3)$$

and the energy levels exhibit a level clustering, i.e. $P_P(S)$ has its maximum at $S = 0$. This is because the energy levels from various independent subsystems are decoupled from each other. In contrast to the level clustering of a Poisson distribution, the energy levels in a Wigner distribution exhibit a level repulsion

$$P_W(S \rightarrow 0) \sim S, \quad (4.4)$$

as derived from Eq. 4.1. The maximum probability in Wigner distribution appears for a mean value of S , not at $S \rightarrow 0$.

In the present case, we analyzed the statistical properties of the NNSs in helium based on the theoretical results. Since the number of resonances is limited, we used integrated Wigner or Poisson distribution for the NNSs in order to reduce statistical fluctuations. In this way we obtain

$$N_W(S) = 1 - \exp\left(-\frac{\pi}{4}S^2\right) \quad (4.5)$$

and

$$N_P(S) = 1 - \exp(-S) \quad (4.6)$$

for a Wigner and a Poisson distributions, respectively, with $N(S) = \int_0^S dS' P(S')$.

The Wigner and Poisson distributions given by Eqs. (4.1) and (4.3) as well as their integrated forms given by Eqs. (4.5) and (4.6) are plotted in Fig. 4.2. In order to better understand the NNS distributions, we additionally added the NNS distribution for one regular Rydberg series presented by a dotted line in this figure. In classical integrable systems, the number of constants of motion is equal to the degrees of freedom. A system with fewer constants of motion than degrees of freedom becomes non-integrable and has regions in phase space, where the dynamics is chaotic. In a transition from a classical to a quantum system, the constants of motion become quantum numbers. Therefore, one could study the chaotic dynamics by the quantum numbers of the system. In Fig. 4.2, three curves, δ -function or step function, Poisson distribution, and Wigner distribution, correspond to three different systems taking their quantum numbers into account. δ -function or step function indicate that the resonances belong to one regular Rydberg series. The reason is that quantum defect numbers should be equal for all resonances in a regular Rydberg series, which results in the unity of the NNSs [25] according to the Rydberg formula. Poisson distribution demonstrates the character of several independent subsystems. These subsystems can be regular Rydberg series or chaotic subsystems [10]. In this case, one can assume that there are still some good quantum numbers, which allow to identify separately the independent subsystems, and the corresponding system is not fully chaotic. In contrast to the δ -function and Poisson distribution, the Wigner distribution describes a chaotic system without good quantum numbers.

The Wigner distribution of NNS is a typical and universal characteristics of energy level fluctuations of chaotic quantum spectra, which is called BGS conjecture by Bohigas, Giannoni, and Schmit [66]. So far, Wigner distributions for the NNSs were observed in a variety of very different chaotic systems, ranging from atom to microwave billiard. Fig. 4.3 presents a collection of NNS distributions that result from a number of very different systems, e.g. the NNS distributions for the Sinai billiard¹ [66], the hydrogen atom in a strong magnetic field [67], for the excitation spectrum of a NO₂ molecule [68], for the acoustic resonance spectrum of a Sinai-shaped quartz block [69], for the microwave spectrum of a three-dimensional chaotic cavity [70], and for the vibration spectrum of a quarter-stadium shaped plate [71]. For all these examples including quantum and classical cases, excellent agreement with a Wigner distribution is found. Obviously, the BGS conjecture is independent of the quantum mechanical systems, but remains valid in a much more general context. Therefore, the search for a Wigner distribution of energy levels has become a standard tool to study the manifestation of chaos, i.e. many researchers regard it as a fundamental signature of quantum chaos [9].

Throughout this part of the dissertation, the Wigner distribution, the Poisson distribution, and the step function will be employed to study the dynamics of doubly excited

¹The billiard with a reflecting disk located in the center.

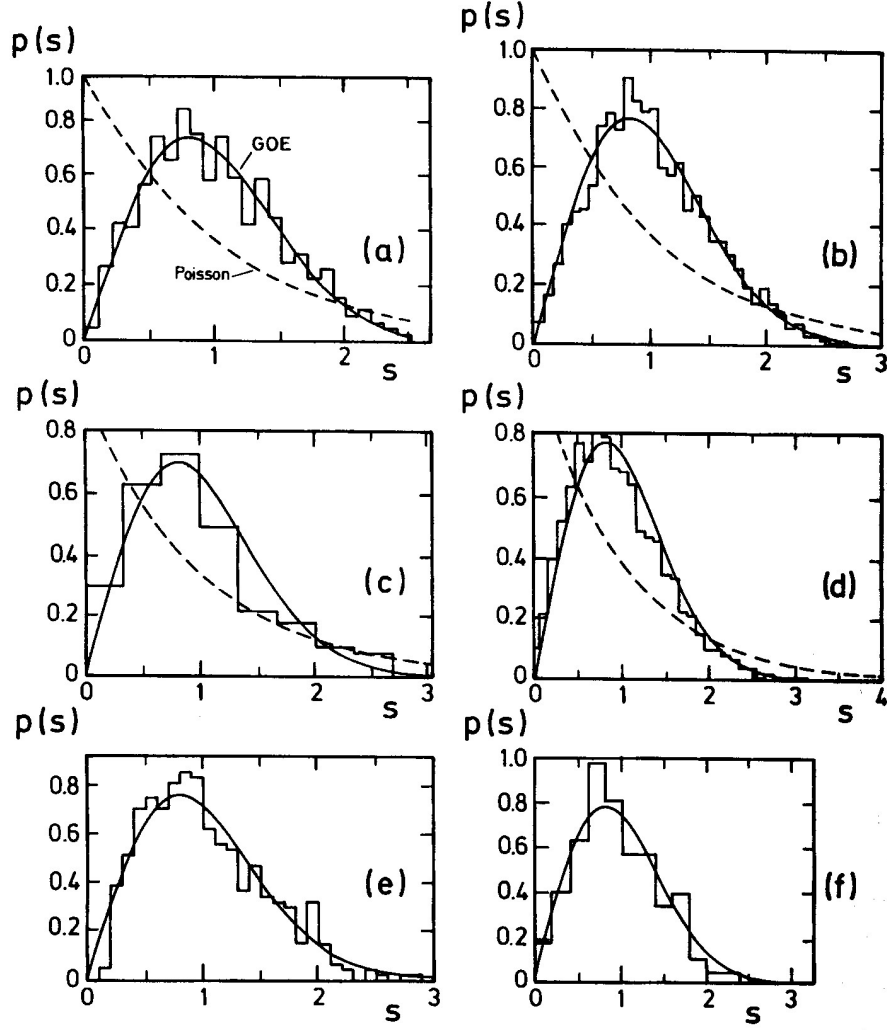


Figure 4.3: Level spacing distributions for (a) a Sinai billiard [66], (b) a hydrogen atom in a strong magnetic field [67], (c) the excitation spectrum of a NO_2 molecule [68], (d) the acoustic resonance spectrum of a Sinai-shaped quartz block [69], (e) the microwave spectrum of a three-dimensional chaotic cavity [70], and (f) the vibration spectrum of a quarter-stadium shaped plate [71]; (from Stöckmann [9])

resonances in helium in the region close to the double-ionization threshold, where quantum chaos is expected, to occur.

4.2 Ericson fluctuations and autocorrelation function

As discussed in the previous section, the Wigner distribution of the NNSs of the resonances is considered to be a standard characteristic for chaotic quantum spectra. As an additional characteristic of quantum chaos, the concept of Ericson fluctuations was developed by Ericson in 1960 [26]; it was originally related to investigations of fluctuat-

ing nuclear spectra. Nowadays, these Ericson fluctuations are considered to be a general fingerprint for quantum chaotic scattering rather than only a nuclear phenomenon [10].

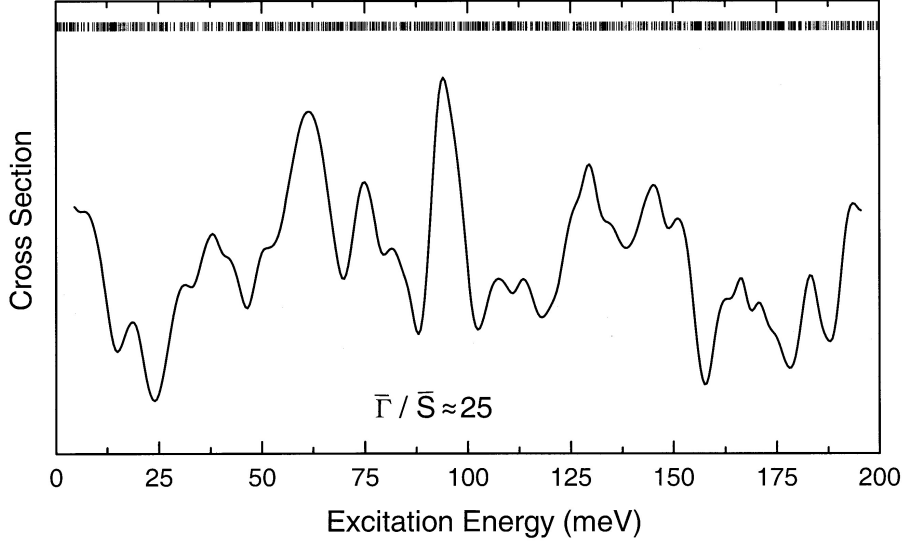


Figure 4.4: Simulated spectrum of Ericson fluctuations characterized by $\Lambda = \bar{\Gamma}/\bar{S} \gg 1$. The spectrum convoluted with a Gaussian function of 1.5 meV (FWHM) is plotted as a function of relative excitation energy. The energy positions of resonances are indicated by the vertical bars.

The Ericson fluctuations can be observed if the resonances in the spectra are strongly overlapping and the intensities of these resonances are randomly distributed, i.e. can be considered to be of the same order of magnitude. The strong overlap means that the average decay width, $\bar{\Gamma}$, of the resonances is much larger than their average energy spacing, \bar{S} . This can be quantified by defining the Ericson parameter, $\Lambda = \bar{\Gamma}/\bar{S}$. The above described case of $\Lambda = \bar{\Gamma}/\bar{S} \gg 1$ is defined as Ericson regime. If these two prerequisites, $\Lambda \gg 1$ and a comparable intensity of all resonances, are fulfilled, a spectrum consists of fluctuations which cannot be identified with single resonances. These Ericson fluctuations can be observed in a simulated spectrum in Fig. 4.4 with an Ericson parameter of $\Lambda \cong 25$. About 1000 Fano-resonances, with an average width of $\bar{\Gamma} = 5$ meV, are randomly distributed in an energy region of 200 meV, and this spectrum was convoluted with a Gaussian function of 1.5 meV (FWHM). It should be mentioned that the intensities of all resonances are random, i.e. they are comparable.

Ericson [26] predicted that spectra with Ericson fluctuations display a autocorrelation function, $C(\varepsilon)$,

$$C(\varepsilon) = \frac{1}{\bar{\sigma}^2} \int_{E_1}^{E_2} [\sigma(E + \varepsilon) - \bar{\sigma}] [\sigma(E) - \bar{\sigma}] dE, \quad (4.7)$$

with a Lorentzian form. Here, $\bar{\sigma}$ is the average cross section in the energy interval $E_1 \leq E \leq E_2$ and ε the displacement. From these autocorrelation function one can estimate the average width of resonances by a fit analysis. So far, it became a common method to analyze fluctuating spectra not only in the case of nuclear reactions [72] but also in

atomic scattering [16, 73]. Finally, we have to emphasize that an autocorrelation function with a Lorentzian form cannot be considered as an unambiguous evidence for Ericson fluctuations in a spectra. For a clear confirmation of Ericson fluctuations one has to ensure that the intensities of the resonances are randomly distributed. By neglecting this, one can easily obtain wrong conclusions about the existence of Ericson fluctuations; this topic will be addressed in more details in combination with our TCS data in the Sect. 4.5.

4.3 The classical configurations

In the past 30 years, a modern semiclassical theory was developed to understand quantum chaos with the help of classical configurations. From the Bohr-Sommerfeld quantization condition, we know that there exists a strong classical-quantum correspondence in integrable systems. M. Gutzwiller [7, 8] realized that it is impossible to use a Bohr-Sommerfeld type of quantization to deal with chaotic systems. He introduced an entirely new semiclassical approach that abandoned the attempt to find individual chaotic states. A remarkable result of these considerations is Gutzwiller's trace formula [7, 8], which establishes a bridge between quantum states and classical periodic orbits, i.e. this formula can be utilized to calculate the density of quantum states from classical periodic orbits in a chaotic system and vice versa. These classical periodic orbits can be identified using a Fourier transformation of the quantum spectra. So far, one realizes that strong classical-quantum correspondences exist even in chaotic systems. However, this issue is beyond the topics in this dissertation. In the following, we shall introduce three classical configurations, which are necessary to understand the changes of approximate quantum numbers $N, K_{n'}$. These quantum numbers will be used to assign doubly excited resonances in helium as discussed before.

For doubly excited states in helium, the following three configurations in the classical space are of particular interests:

$$\begin{aligned}
 (A) \quad & eZe \text{ configuration: } \theta_{12} \equiv \pi; \quad p_{\theta_{12}} \equiv 0 \\
 (B) \quad & Zee \text{ configuration: } \theta_{12} \equiv 0; \quad p_{\theta_{12}} \equiv 0 \\
 (C) \quad & \text{Wannier ridge: } r_1 \equiv r_2; \quad p_{r_1} \equiv p_{r_2}.
 \end{aligned} \tag{4.8}$$

r and p are the coordinates and the momenta of electrons, respectively, while 1 and 2 label two different electrons, and θ_{12} is the angle between two electrons. (A) and (B) are collinear configurations, i.e. all particles move on one line; this is equivalent to a one-dimensional helium atom.

In the collinear configuration (A), all three particles move along one axis, with both electrons on opposite sides of the nucleus. It is called *eZe* configuration and shown in Fig. 4.5(b). In contrast to the *eZe* configuration, the *Zee* configuration, shown in Fig. 4.5(a), describes a motion with both electrons on the same side of the nucleus. The configuration (C) is a Wannier ridge, which shows the symmetric electron motion in a symmetry plane. The resonances corresponding to Wannier classical orbits are expected to appear only

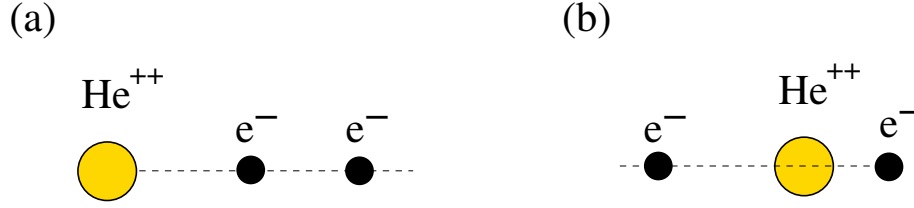


Figure 4.5: The two collinear configurations: (a) the stable Zee configuration and (b) the eZe configuration, which is chaotic in radial direction.

in the limit of double excitation very close to the double-ionization threshold [2, 74, 75]. The Wannier ridge, together with the eZe configuration, is predicted to contain the decay channels for double-ionization [76]. For detailed studies of the dynamics of these classical configurations, see Ref. [2] and references, therein.

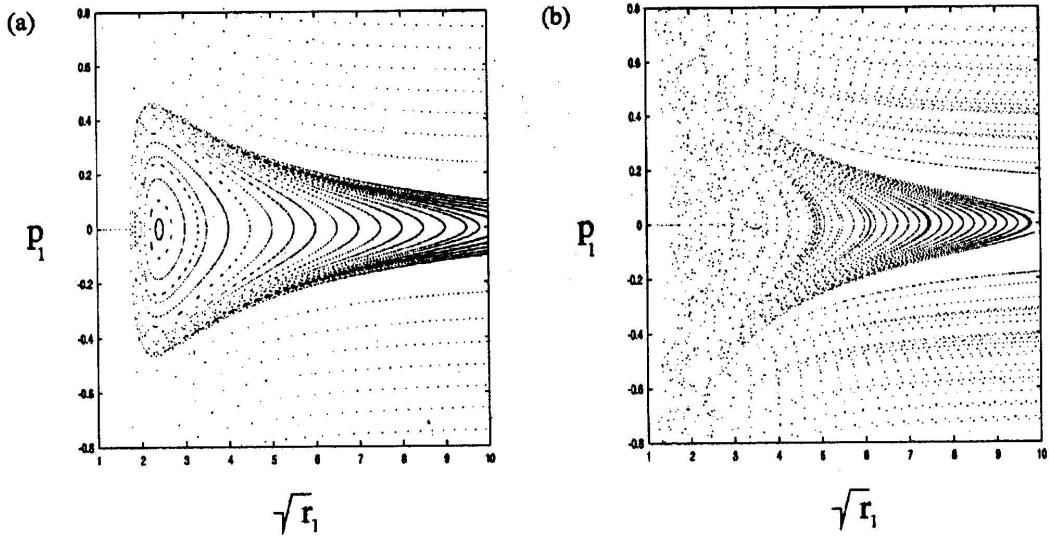


Figure 4.6: Poincaré map of helium for the two collinear configurations at $r_2 = 0$: (a) $\theta = 0$; (b) $\theta = \pi$ (taken from Ref. [2]).

Choosing $r_2 = 0$, one plots the phase space (Poincaré map) of the two collinear configurations in Fig. 4.6, i.e. the momentum of the outer electron is given as a function of its position. In the Zee configuration, surprisingly, the three-body Coulomb interaction leads to a stabilization of the dynamics in helium, which can be demonstrated well by a large stable island in the Poincaré map given in Fig. 4.6(a) [77]. The large stable island indicates that the outer electron in the Zee configuration is frozen at a finite distance from the nucleus, i.e. the outer electron cannot penetrate the inner electron and, therefore, cannot hit the nucleus. Due to the electron-electron and electron-nucleus interactions, the outer electron performs an oscillation at a frozen distance. In contrast, the inner electron can move between the nucleus and the outer electron. Therefore, the Zee is a quite stable configuration. In contrast to the stable Zee configuration, no stable islands can be found in the eZe configuration in the Poincaré map given in Fig. 4.6(b), particularly as $r_1 \rightarrow 0$, where the Poincaré map is completely structureless. In

this configuration, triple collision ($r_1 = r_2 = 0$) can occur. This, in turn, results in large momentum transfer among the three bodies (two electrons and the nucleus), and has been considered as the origin of chaos in the eZe configuration.

In summary, for perturbations in the direction of the electron-nucleus axis, the 1-dimensional helium is unstable in the eZe configuration but stable in the Zee configuration. Both configurations are stable with respect to perturbations perpendicular to the collinear phase space, i.e. stable in the angular direction. In this dissertation, the two classical configurations eZe and Zee will be employed to understand the existence and loss of the approximated quantum numbers $N, K_{n'}$, where N and n' (K) describe the radial (angular) directions.

4.4 Complex-rotation method

As we mentioned before, the statistical studies were performed using the theoretical results D. Delande obtained with the complex-rotation method. This procedure is due to the extremely low intensity of most of the Rydberg series which give rise to the fact that only a very small fraction of doubly excited states can be observed experimentally. Therefore, the complex-rotation method will be described briefly.

The method of complex-rotation [78, 79] is quite different with other methods in determining the resonant state; normally, these resonances are obtained by diagonalization of a Hamiltonian matrix. The difference of the complex-rotation method is due to the complex scalings of the radial coordinates and momenta, $r \rightarrow re^{i\theta}$ and $p \rightarrow pe^{-i\theta}$. In this way, the expectation value of the Hamiltonian becomes

$$\langle n_\theta | H | n_\theta \rangle = E_n - i\Gamma_n/2, \quad (4.9)$$

where $|n_\theta\rangle$ is the complex scaling wave function for the double-excitation states, and E_n and Γ_n represent the positions and the linewidths of resonances, respectively. The dipole transition matrix has the complex form

$$\langle i | D | n_\theta \rangle = B_n + iC_n, \quad (4.10)$$

with $|i\rangle$ being the ground state. Using the complex parameters B_n and C_n together with E_n and Γ_n , the Fano-shape parameterization of the cross section yields

$$\sigma_T = \sigma_T^0 + \sum_n \frac{(q_n + \epsilon_n)^2}{1 + \epsilon_n^2} \mu_n^2 - \mu_n^2, \quad (4.11)$$

where

$$\begin{aligned} \epsilon_n &= 2 \frac{E - E_n}{\Gamma_n}, \\ q_n &= -\frac{B_n}{C_n}, \\ \text{and } \mu_n^2 &= \frac{2C_n^2}{\pi\Gamma_n}. \end{aligned} \quad (4.12)$$

The cross section and Fano parameters can be directly derived from the two matrix elements given in Eqs. 4.9 and 4.10. This is a substantial advantage of the complex-rotation method compared to other methods, since the resonant parameters E_n , Γ_n , and q_n as well as the expectation value $\langle \cos\theta_{12} \rangle$, can be obtained directly from calculations; they do not have to be derived by a fit analysis of the calculated cross section, which is impossible in the present case of strongly overlapping resonances. The value $\langle \cos\theta_{12} \rangle$ is related to the approximate quantum number K by Eq. (3.16). Therefore, the complex-rotation method is very well suited to provide data for statistical studies of the resonant parameters E_n , Γ_n , and q_n .

In the late 1990's, complex scaling photoabsorption calculations for helium performed by Gremaud and Delande [32] covered the energy regime up to the SIT I_9 and have been used by our group to perform statistical studies on the NNSs of energy levels in that region [18]. Very recently, Delande [27] further extended these calculations up to the SIT I_{17} , i.e. up to 150 meV below the double-ionization threshold of helium. These calculated data will be employed for the studies of quantum chaos in the next section of the dissertation.

4.5 Quantum signatures of chaos in highly excited states of helium

4.5.1 Experimental total cross sections up to I_{15}

The high-resolution photoionization spectra presented in Fig. 4.7 were measured up to the SIT I_{15} using a gas cell described in chapter 2. The experiments were performed at the high-resolution undulator beamline UE56-2/PGM2 of the Berliner Elektronenspeicherring für Synchrotronstrahlung (BESSY II) using a photon energy resolution of $\Omega \cong 1.7$ meV (FWHM). A pressure of $\cong 1$ mbar was used in the gas cell, and an operating voltage of 100 V was applied to the plates within the gas cell. The spectra were taken with a step width of 250 μ eV, and six scans were recorded for each energy region in order to ensure reproducibility and to improve the signal-to-noise ratio. The backgrounds of the spectra were simulated and subtracted from the spectra. The photon energies of the spectra were calibrated by the result of the calculations of Delande [27].

In Fig. 4.7, the present experimental data, and the results of theoretical calculation employing the complex-rotation method [27], as well as the results of previous measurements by Püttner *et al.* [18] for the TCSs are plotted as solid lines in three different colors. The vertical bars mark the positions of the SITs up to I_{14} . The theoretical data were convoluted by a Lorentzian function with a FWHM of 1 meV. A comparison of the recent experimental and theoretical results shows an impressively good agreement for the entire spectrum. The present spectra show an improved signal-to-noise ratio and higher resolution than the previous measurements [18]. The present experimental and theoretical data above 78.28 eV are the first ones in this energy region, i.e. data below 6 new ionization thresholds were obtained. The complex features the spectra indicate

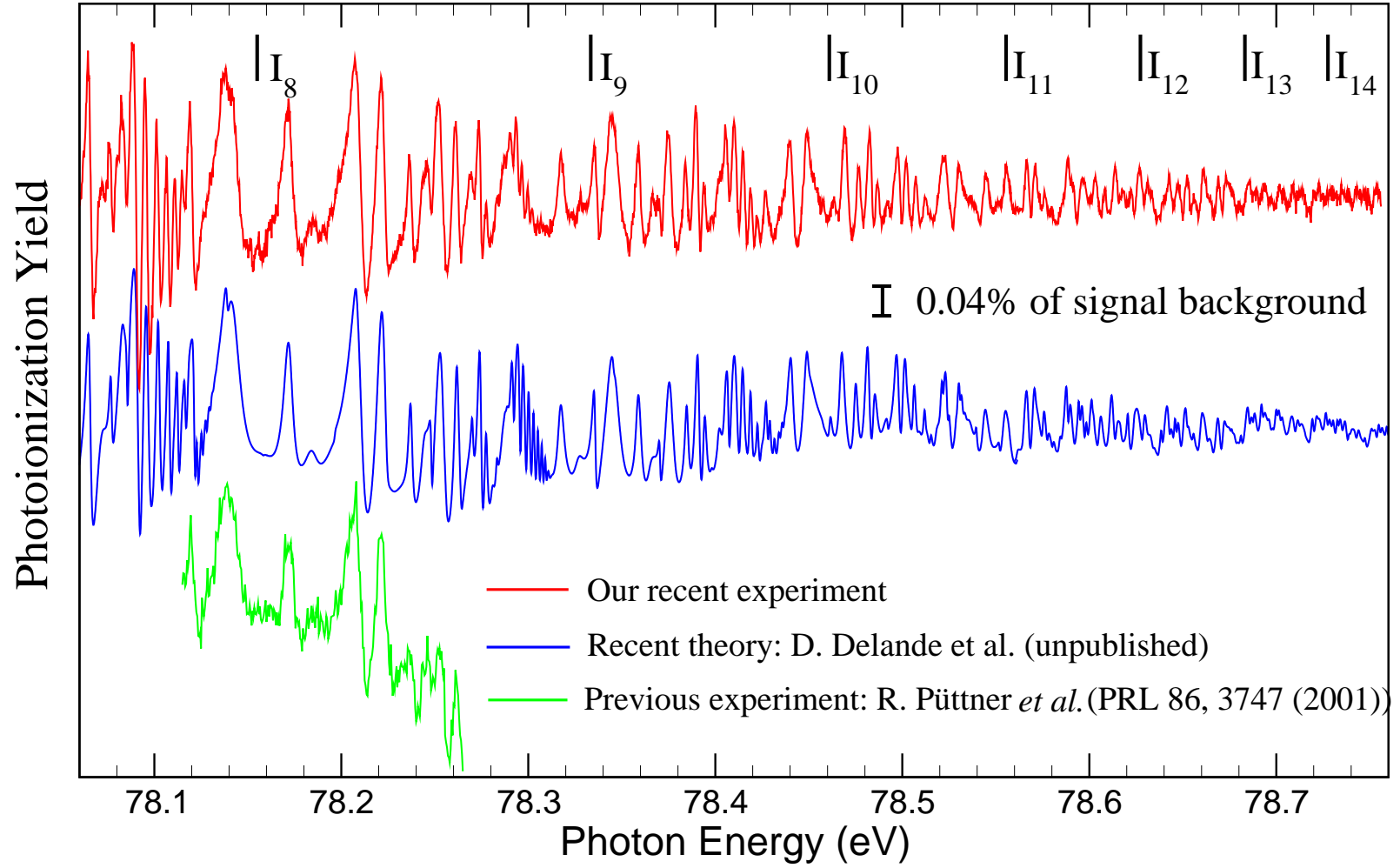


Figure 4.7: Total cross section of doubly excited helium below the SIT I_{15} . The present experimental data, complex-rotation calculations [27], and previous measurements [18] are plotted by solid lines in red, blue, and green colors, respectively. The vertical bars indicate the positions of the SITs up to the I_{14} .

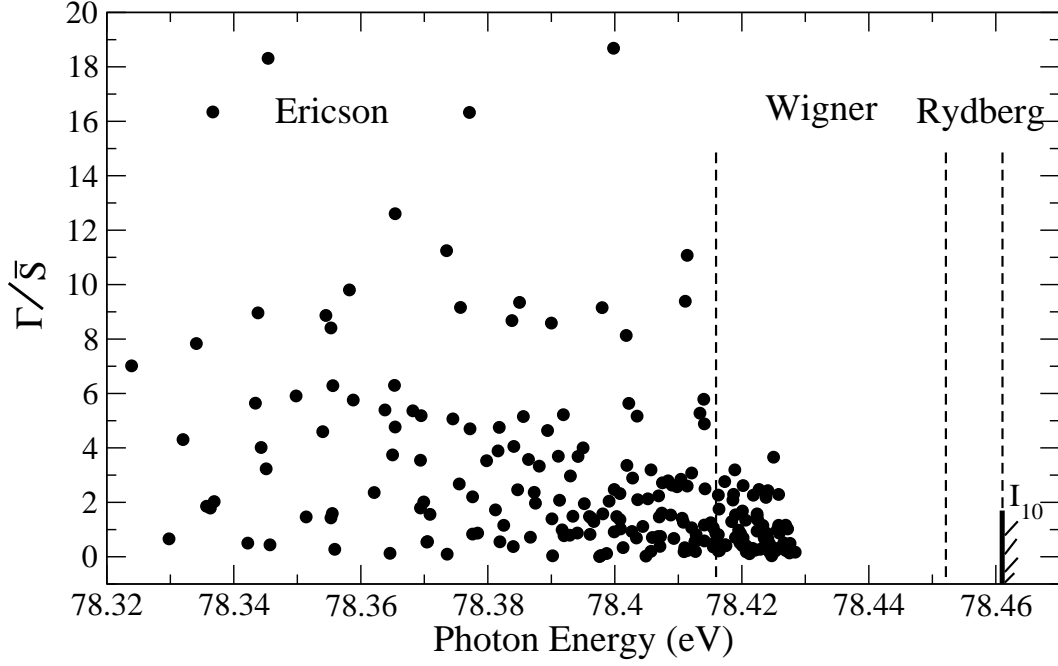


Figure 4.8: Calculated linewidths of doubly excited states in helium below the SIT I_{10} . The resonance linewidths are normalized to the mean value of spacings between the resonance energy positions. Ericson ($\bar{\Gamma} \gg \bar{S}$), Wigner ($\bar{\Gamma} \approx \bar{S}$), and Rydberg ($\bar{\Gamma} \ll \bar{S}$) regimes are indicated.

in the presence of a large number of perturbbers in this energy region. These perturbbers render the spectra significantly irregular (see Fig. 3.3) and it is therefore an interesting question whether or not the spectra can be assigned with isolated resonances. From the experimental point of view, it is really hard to take spectra in this energy region because the amplitudes of the resonances amount to only 0.2% to 0.04% of the signal background. The variations in the pressure and insufficient normalization to the photon flux could render the observation of these resonances impossible. From the theoretical point of view, many challenges are also faced due to the calculation model, accuracy, and convergence. The present state-of-the-art measurements and calculations of the TCS make it possible to study for the first time chaotic behavior in doubly excited helium very close to double-ionization threshold. The theoretical data obtained by D. Delande [27] are strongly confirmed by the present measurements and can be used as a reliable basis for further data analysis. As mentioned before, we have to use theoretical data for these detailed statistical studies because only a relatively small number of resonances can be observed in the experiments; this will be further illustrated by our fit results described in the following section.

Close to the double-ionization threshold, the mean linewidth of the resonances is much larger than the mean spacing of the resonances, i.e. $\bar{\Gamma} \gg \bar{S}$ (Ericson regime), where the resonances are strongly overlapping. In this case, the spectra are assumed to fluctuate and cannot be identified. Generally, the Ericson regime together with the comparable intensities of the spectra are assumed to be the conditions for observing Ericson fluctuations in the spectra as mentioned in Sect. 4.2. In this part, the main aim

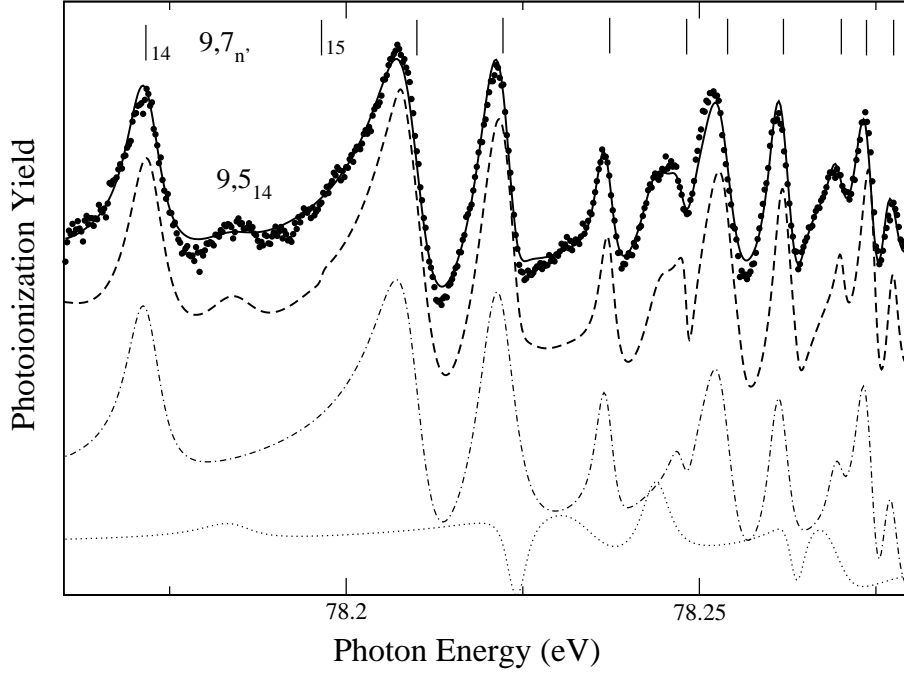


Figure 4.9: Total cross section below the SIT I_9 : The present experimental data are given by solid points, the fit result by the solid curve through the data points. The result of the complex-rotation calculations is given by the dashed curve. The fit components for the principal and secondary Rydberg series are represented by the dash-dotted and dotted lines. The vertical-bar diagrams in the upper part of the figure give the assignments of the resonances belonging to the Rydberg series $9, 7n'$.

of the analysis of the experimental data is to figure out whether Ericson fluctuations are present in the studied energy region. In Fig. 4.8, the normalized linewidths of doubly excited states in helium below the SIT I_{10} are plotted as a function of photon energy. These linewidths are normalized to the mean value of the spacings between the resonance energy positions. These data were calculated with the complex-rotation method by D. Delande [27]. There are three classes of resonances below each SIT, which can be identified by a comparison of the linewidths and energy level spacings. They are, in the order of increasing energy, Ericson ($\bar{\Gamma} \gg \bar{S}$), Wigner ($\bar{\Gamma} \approx \bar{S}$), and Rydberg ($\bar{\Gamma} \ll \bar{S}$) regimes, respectively, which have been identified below I_{10} and are indicated in Fig. 4.8. Later, the analysis of experimental spectra will focus on the region, where the corresponding resonances are in the Ericson regime, i.e. $\bar{\Gamma} \gg \bar{S}$.

A detailed comparison between the experimental and theoretical TCSs in the region up to the SIT I_{14} are given in Figs. 4.9 to 4.14. In these figures, the experimental TCSs are plotted as solid points and the dashed lines represent the theoretical results. The fit results are displayed by solid lines through the data points. As an example, the contributions of individual resonances for the principal and secondary Rydberg series are plotted by dash-dotted and dotted lines, respectively, in the lower part of Fig. 4.9. The vertical bars in the upper part of each figure mark the energy positions of the resonances. In the fit process, we fixed the resonance positions, linewidths, and Fano parameters q to

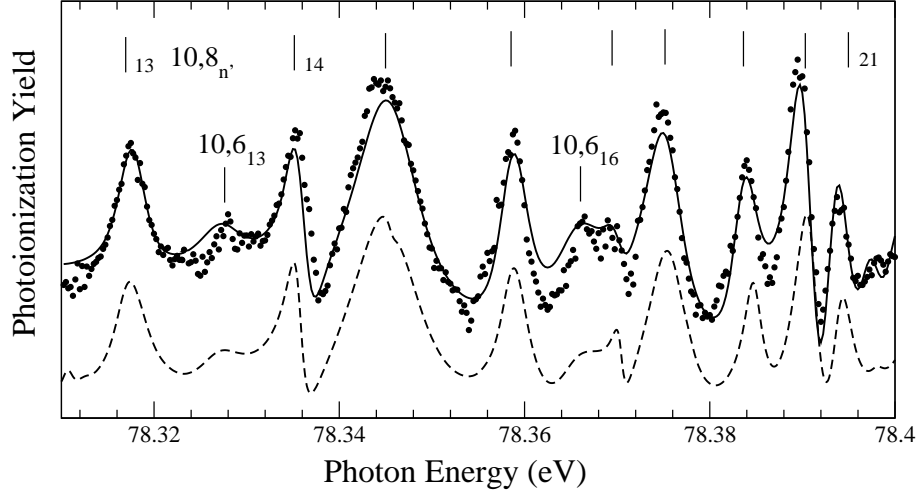


Figure 4.10: Total cross section below the SIT I_{10} . For details, see caption of Fig. 4.9.

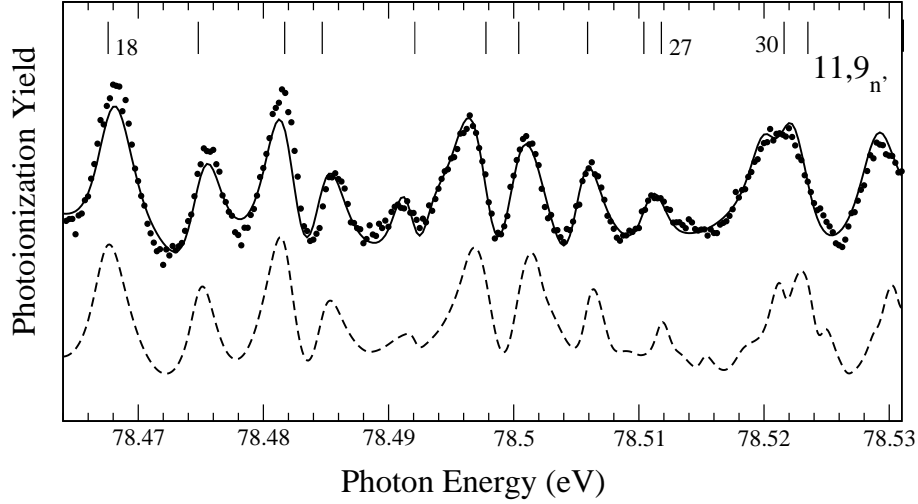


Figure 4.11: Total cross section below the SIT I_{11} . For details, see caption of Fig. 4.9.

the values of the calculations by D. Delande [27]. The intensities are treated as the only free parameters and the obtained relative intensities for most of the resonances agree with the calculated ones within a factor of 2. Due to possible tiny mechanical problems of the used monochromator [80], which could lead to small non-linearities, the photon energies of the individual resonances were allowed to have shift linearly up to 1 meV. The aim of the fits is to determine the number of resonances that are needed to reasonably describe the spectra. This is closely related to the question whether Ericson fluctuations are present in this region of the spectrum or not. Therefore, the spectra are described by fit routines using the smallest number of resonances, which lead to a sufficiently good description; such a fit procedure can be called "describing fit".

For the spectra below the SITs I_9 to I_{14} , 15 to 25 resonances were used in the describing fits. Most of these resonances can be assigned to members of the principal series ($K = N - 2$), while a much smaller fraction belongs to the secondary series ($K =$

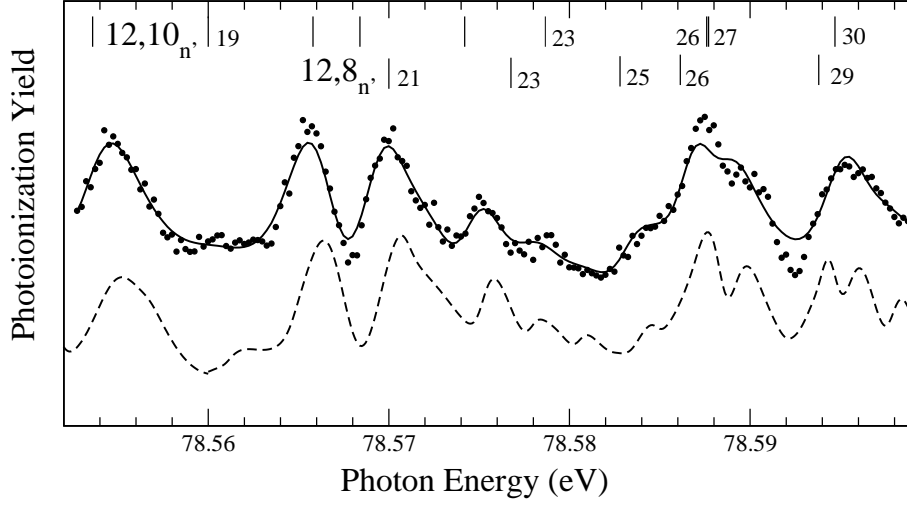


Figure 4.12: Total cross section below the SIT I_{12} . For details, see caption of Fig. 4.9.

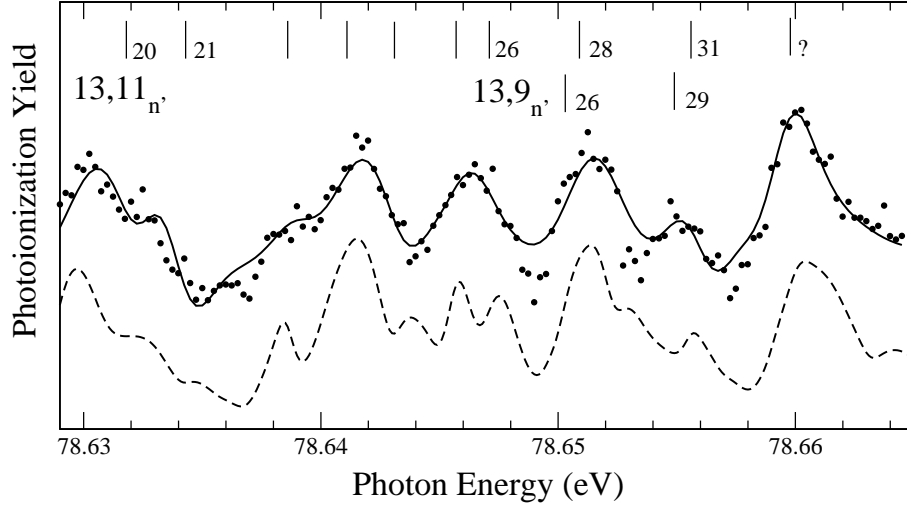


Figure 4.13: Total cross section below the SIT I_{13} . For details, see caption of Fig. 4.9.

$N - 4$); this can be seen from the fit components shown in Fig. 4.9, as an example. With these finite numbers of resonances, the experimental spectra can already be described quite well. Note that there are 17–27 Rydberg series with more than 300 resonances in the corresponding energy regions below each of the SITs I_9 to I_{14} . In addition, we point out again that Fig. 4.8 gives clear evidence that the spectra studied in this dissertation are in the Ericson regime, i.e. $\bar{\Gamma} \gg \bar{S}$. However, the present describing fits indicate clearly that the spectra are still dominated by essentially a single Rydberg series, namely the principal series ($N = K - 2$); this means that Ericson fluctuations caused by a large number of overlapping resonances are essentially absent in the spectra. This indicates that some approximate quantum numbers $N, K_{n'}$ should be still valid, a fact that will be proven later on by analyzing the calculated K values and by a statistical analysis of energy spacings between the resonances. So far, we can conclude that the Ericson

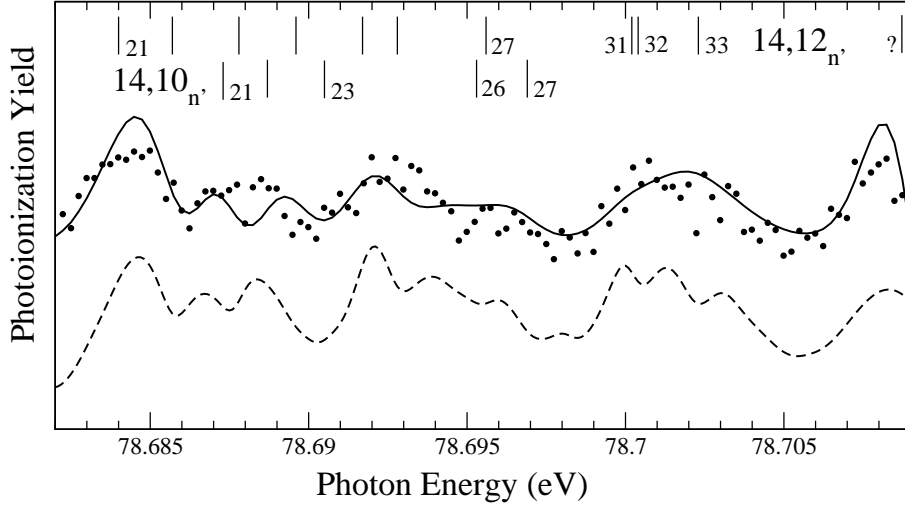


Figure 4.14: Total cross section below the SIT I_{14} . For details, see caption of Fig. 4.9.

regime is not a unique condition for observing Ericson fluctuations in the spectra. The amplitudes of transitions have to be distributed randomly.

We further point out that the agreement between the measurements, the fits, and the calculations becomes worse with increasing photon energies according to the increasing noise. On the basis of the describing fits and theoretical data, we assigned for the first time the experimental spectra up to the SIT I_{14} . The symbol “?” in Figs. 4.13 and 4.14 implies that a particular resonance could not be identified since its K -value could not be obtained from the calculations due to convergence problem. The theoretical convergence problem close to each SIT does not affect the reliability of the TCS [27], however. Due to missing resonance parameters close to each SIT, it was not possible to analyze the entire spectrum presented in Figs. 4.7 by the describing fits, which are presented in Figs. 4.9 to 4.14.

Although it has been proven that Ericson fluctuations are absent in the present spectrum, in the following we want to discuss its autocorrelation function since such an autoionization function was employed by G. Stania and H. Walther [16] as an evidence for Ericson fluctuations in the photoionization spectra of ^{85}Rb atom. To this end we compare the TCS of helium without Ericson fluctuations in Fig. 4.9 with a simulated spectrum in Fig. 4.4 that clearly displays Ericson fluctuations. We first want to point out that these two spectra exhibit similar features so that it is not possible to identify Ericson fluctuations by the variations in the cross section. For these both spectra the autocorrelation functions defined by Eq. (4.7) are calculated and presented in Fig. 4.15(a) and (b). The dashed lines in this figure are the results of a fit to a Lorentzian function, which is prediction for Ericson fluctuations. For small displacements, i.e. ε close to 0, the autocorrelation functions agree quite well with the Lorentzian function. For larger displacements, oscillations around zero are observed. The average widths of resonances of $\cong 2$ and 5 meV for the spectra in Figs. 4.9 and 4.4, respectively, are in good agreement with the ones of $\cong 3$ and $\cong 4$ which were derived from the fits. The observed features of the autocorrelation function are quite similar to that observed by G. Stania

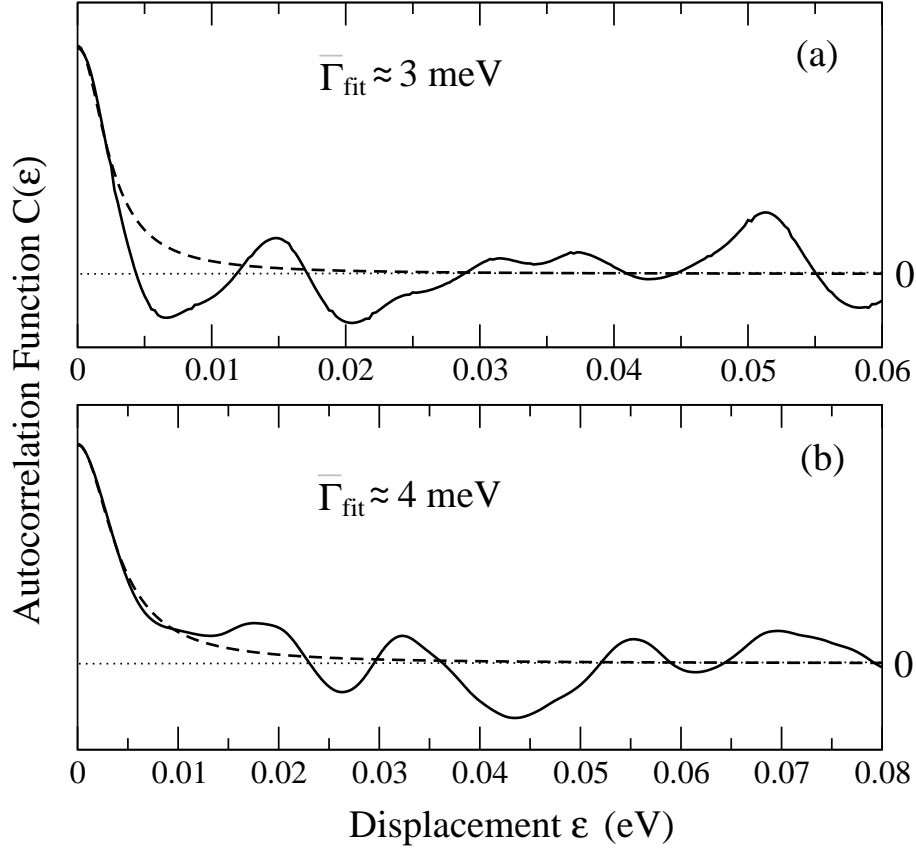


Figure 4.15: (a) Autocorrelation functions for the spectra given in Fig. 4.9 and (b) in Fig. 4.4. The dashed lines represent the fit results to a Lorentzian function, and the dotted horizontal lines indicate the value of zero.

and H. Walther. As stated before, the TCS given in Fig. 4.9 does not exhibit Ericson fluctuations. This is due to the fact that the spectrum is dominated by the principal Rydberg series although the Ericson regime ($\Lambda = \bar{\Gamma}/\bar{S} \cong 3$) is fulfilled. In addition, for small ε the autocorrelation function displays a Lorentzian shape (see Fig. 4.15(a)). Similar autocorrelation functions were also found for the TCSs in the other regions up to I_{13} where the Ericson parameter, Λ , has larger values. These considerations show that Ericson fluctuations in a spectrum can neither be identified by the shape of the spectral variations nor by the autocorrelation function. It is, therefore, essential to ensure that the intensities are also randomly described with a large number of overlapping resonances. Nevertheless, the average width of the resonances in a fluctuating spectrum can be estimated by fitting the autocorrelation function to a Lorentzian function; this can be seen from our simulated chaotic spectrum in Fig. 4.4 as well as its autocorrelation function in Fig. 4.15(b).

In the work of G. Stania and H. Walther [16] as well as J. Madronero and A. Buchleitner [17], an autocorrelation function with a Lorentzian shape for small displacements was used to prove the observation of Ericson fluctuations. However, the the question of comparable amplitudes for the transitions was not carefully addressed. The present case of helium shows that this omission may lead to wrong conclusions if there is – contrary

to an assumption – an unexpected hierarchy in the intensities of the different resonances.

4.5.2 Calculated K values up to I_{17}

In the last section, we concluded from the describing fits that Ericson fluctuations do not occur although the conditions for the Ericson regime is fulfilled, as shown in Fig. 4.8; i.e. the spectra are still dominated by the principal series $N, K_{n'}$, with $K = N - 2$, at least up to the SIT I_{14} . The spectral features in this energy region were assigned using the approximate quantum numbers $N, K_{n'}$. However, this does not mean that approximate quantum numbers are still valid for all resonances. As mentioned before, the complex-rotation method has the advantage that the K values for each resonance can be calculated directly. With this theory, Delande [27] has performed calculations for K values up to the SIT I_{17} , as well as for the TCS below the SIT I_{14} . The accuracy of these calculations is confirmed by our recent experimental results as discussed in the previous section. Here, we shall discuss the approximate quantum numbers $N, K_{n'}$ on

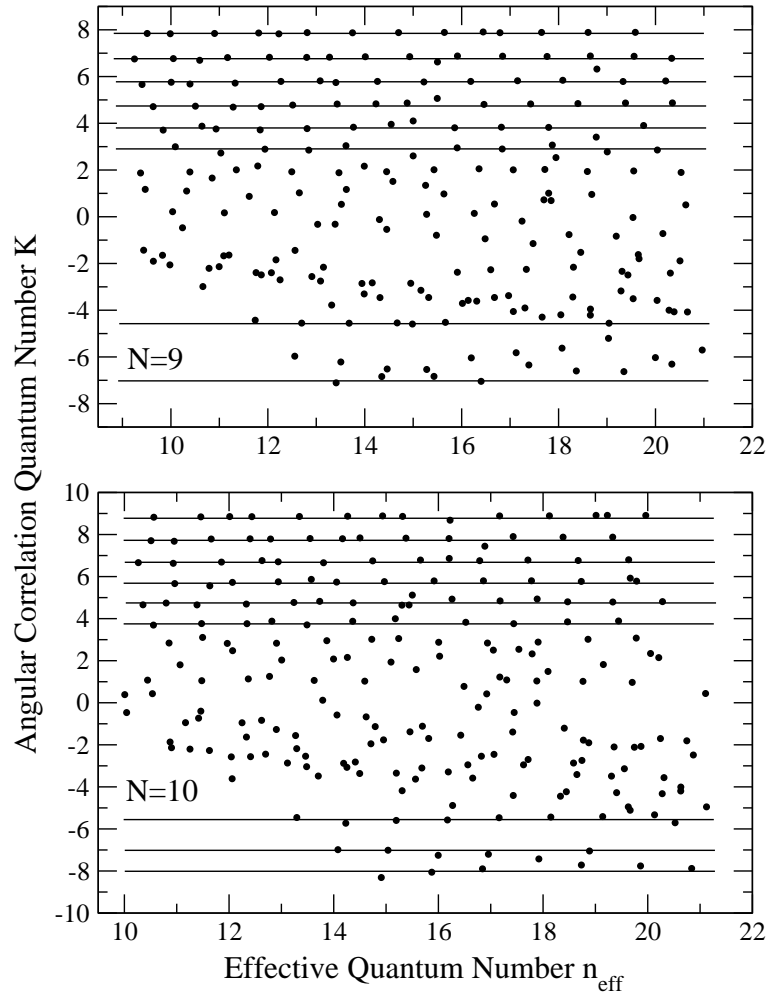


Figure 4.16: Angular correlation quantum numbers K calculated by D. Delande [27] below the SITs I_9 and I_{10} as a function of effective quantum number. Each point represents one resonance and the horizontal lines imply Rydberg series specified by individual K values.

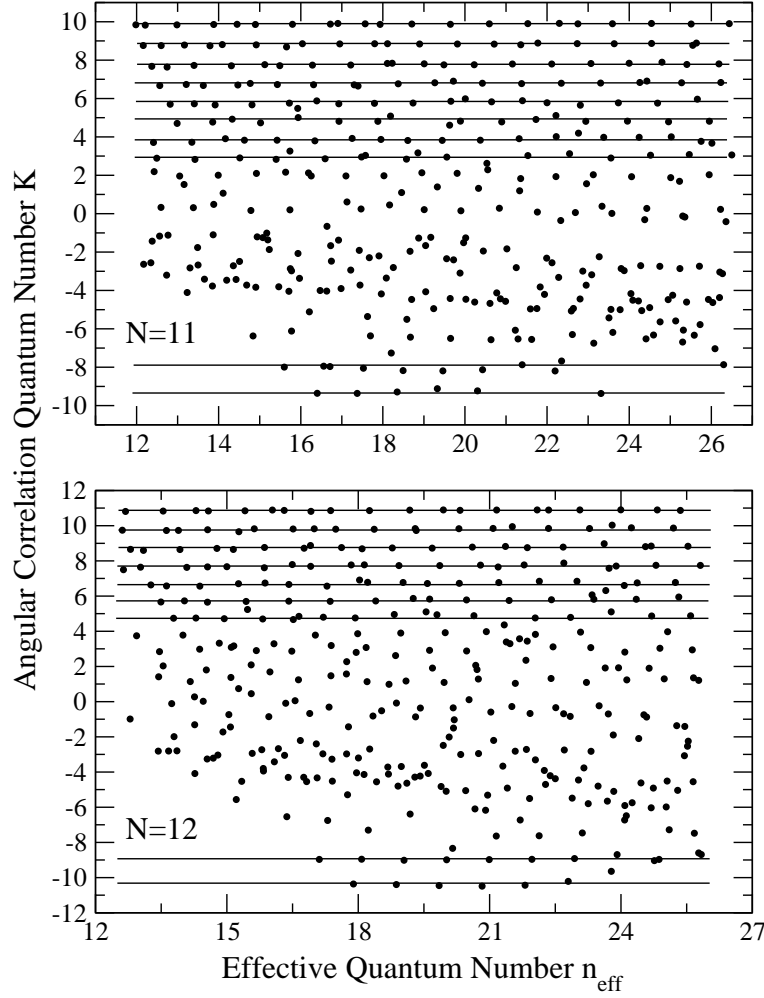


Figure 4.17: Calculated angular correlation quantum numbers K below the SITs I_{11} and I_{12} as a function of the effective quantum number. For details, see Fig. 4.16.

the basis of reliable K values. This will help to understand the statistical properties of the NNSs between the resonances, which will be presented in the next section.

The calculated angular correlation quantum numbers K for the doubly excited resonances from the SITs I_8 to I_{17} as a function of the effective quantum numbers n_{eff} are plotted in Figs. 4.16 to 4.20. Each solid point in these figures represents a resonance specified by the K -value and the energy given in units of the effective quantum number. The horizontal lines indicate Rydberg series, which can be identified by individual K values. The spectra were rescaled to the effective quantum numbers by Eq. (4.2) in order to study the radial quantum numbers N and n' . According to quantum defect theory [25], all resonances in a regular Rydberg series, which are specified by various n' , should have the same quantum defect. This results in the energy level spacings to be equal to one on the rescaled energy axis, and implies the radial quantum numbers N and n' to be good quantum numbers. Otherwise, for irregular level spacings, N and n' are assumed to be strongly mixed, i.e. N and n' lose their meanings as the principal quantum numbers of the inner and outer electron in an independent particle picture.

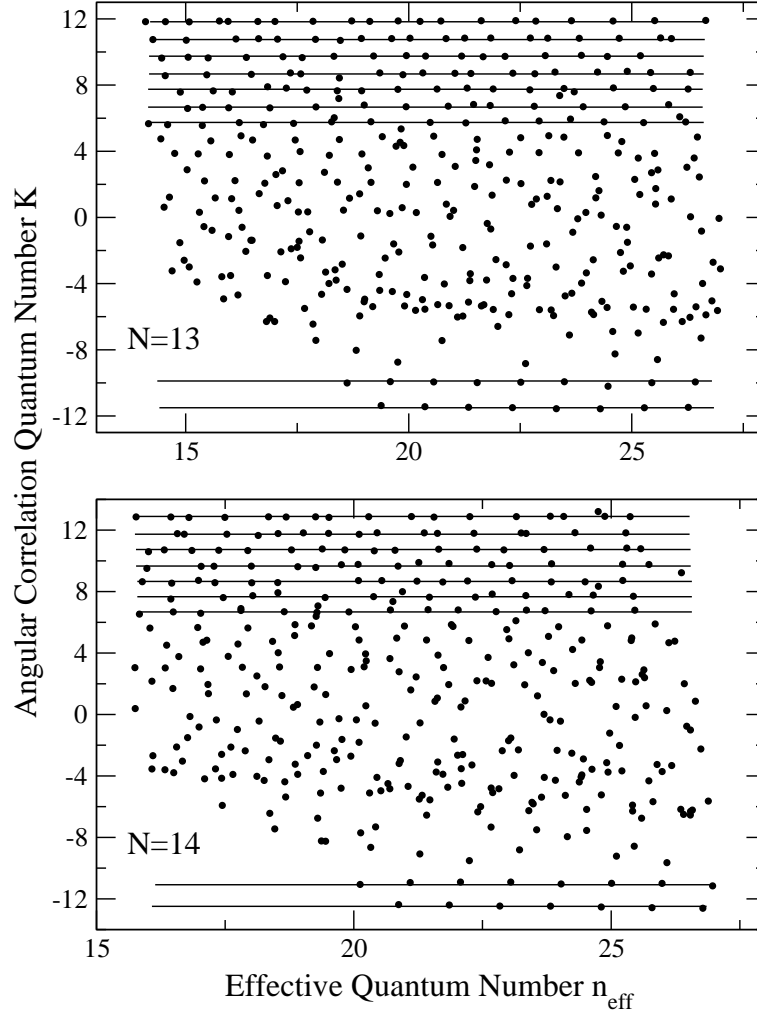


Figure 4.18: Calculated angular correlation quantum numbers K below the SITs I_{13} and I_{14} as a function of the effective quantum number. For details, see caption of Fig. 4.16.

From these figures it can be clearly seen that—for the resonances with K values close to K_{max} —the angular correlation quantum number K has well-defined value. This is indicated by horizontal lines in Figs. 4.16 to 4.20 and allows to define independent Rydberg series. Therefore, in these cases K can be considered to be a good quantum number. The second top horizontal lines represent the principal series with $K = N - 2$ below the various SITs, I_N . From the expression (3.16), the angle between two electrons $\theta_{12} \rightarrow 180^\circ$ as $K \rightarrow K_{max}$, and this corresponds to the classical eZe configuration. As discussed in Sect. 4.3, this configuration is stable towards a perturbation in the angular direction, which results in K being a good quantum number. Therefore, theoretical results for K values agree well with this prediction for the eZe configuration. The energy level spacings of the resonances, which belong to the Rydberg series with constant K , are irregular; they are not equal to unity, which indicates that the radial quantum numbers N and n' start to dissolve for these Rydberg series. This can also be understood by the classical eZe configuration, since this configuration is unstable against perturbations along the axis defined by the two electrons and the nucleus. Interestingly, the number

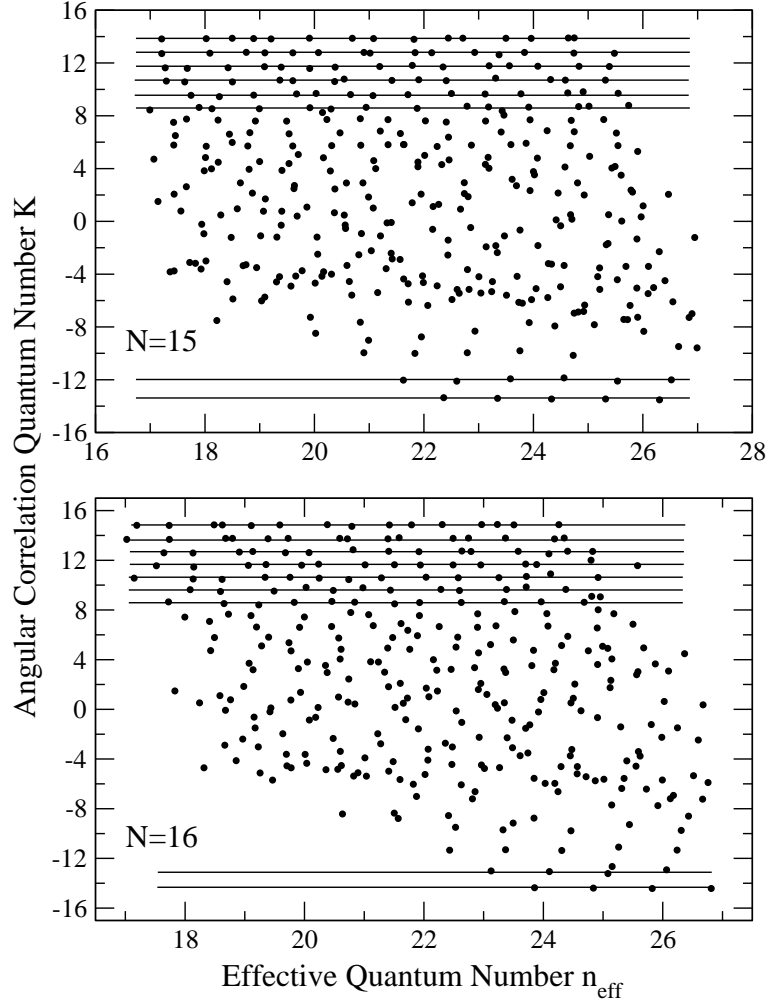


Figure 4.19: Calculated angular correlation quantum numbers K below the SITs I_{15} and I_{16} as a function of the effective quantum number. For details, see caption of Fig. 4.16.

of Rydberg series with good K values in the region of $K \rightarrow K_{\text{max}}$ does not decrease dramatically up to the SIT I_{17} as expected before. The basis for this expectation was the assumption K could break down rather quickly above the SIT I_9 .

K is also found to be a good quantum number for Rydberg series in the region of $K \rightarrow K_{\text{min}}$, in particular for the higher photon energy region above the SIT I_{10} (see Figs. 4.17 to 4.20). This is indicated by horizontal lines in the lower parts of the figures. In addition to that, the energy level spacings of these Rydberg series are always close to one, which proves that the radial quantum numbers N and n' are good quantum numbers. $\theta_{12} \rightarrow 0^\circ$ and $K \rightarrow K_{\text{min}}$ correspond to the classical *Zee* configuration. The *Zee* configuration is also identified by the *frozen planet* orbits [2] and is stable with respect to perturbations in both directions, namely the angular direction and the radial direction. Therefore, the classical *Zee* configuration allows us to understand why K and N are good quantum numbers for Rydberg series in the region of $K \rightarrow K_{\text{min}}$. Note that the calculations below the SIT I_{17} , shown in Fig. 4.20, were not yet completely carried out, i.e. only data for the effective quantum number $n_{\text{eff}} < 24$ are available

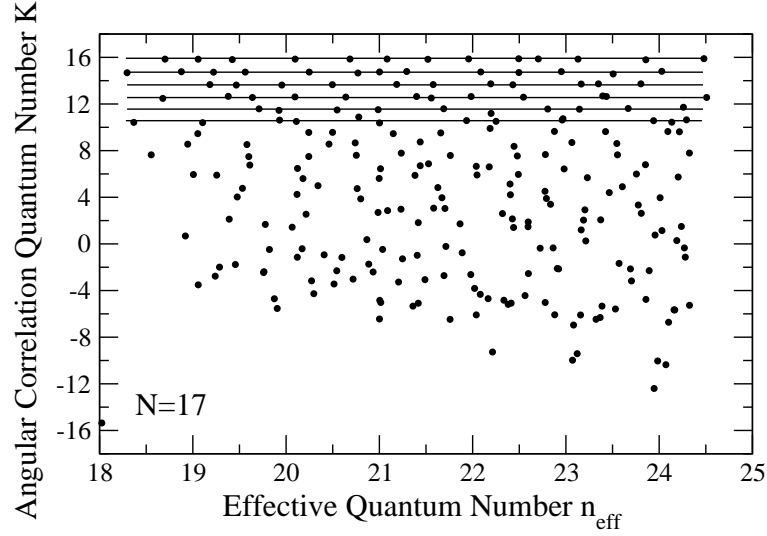


Figure 4.20: Calculated angular correlation quantum numbers K below the SIT I_{17} as a function of the effective quantum number. For details, see caption of Fig. 4.16.

at the moment. From the figures showing data for lower SITs, one can see that the corresponding Rydberg series with K_{min} values start at relatively high effective quantum numbers. This is the reason why the resonances for $K \rightarrow K_{min}$ are not yet available below the SIT I_{17} , but we expect them to have good K quantum numbers.

It is obvious from Figs. 4.17 to 4.20 that there is a strong mixing of K in the regions around $K = 0$, i.e. $\theta_{12} \cong 90^\circ$. More studies are needed to figure out the behavior of quantum number N . The present results on changes of the approximate quantum numbers $N, K_{n'}$ are in agreement with the discussion for $1S^e$ doubly excited state of helium below the SIT I_{10} given by Bürgers *et al.* [81], but they explore the energy region much closer to the double-ionization threshold.

In Fig. 4.21, all calculated $\langle \cos \theta_{12} \rangle$ below the SIT I_{17} , related to K -values by the expression (3.16), are plotted as a function of photon energy. The principal Rydberg series is marked by a solid curve through the resonance points. From this figure, one can clearly conclude that K does not break down as a good quantum number in the energy regions below the SITs I_9 to I_{17} , as expected before; this is particularly true for the regions $K \rightarrow K_{max}$. In addition, we note that the K values for the Rydberg series in the regions $K \rightarrow K_{max}$ increase slowly but constantly. This can be caused by the influences of perturbers with large K values that belong to Rydberg series below the next higher threshold. An increase is also observed at each threshold, which can be understood from the formula given in Eq. (3.16). The same data as in Fig. 4.21 are plotted in Fig. 4.22 in a polar coordinate representation. From this figure, we can see that K is a good quantum number for the regions $\theta_{12} > 100^\circ$ and $\theta_{12} < 50^\circ$, but mixes strongly in the region from $60^\circ < \theta_{12} < 100^\circ$. We note that θ_{12} for the resonances of the principal Rydberg series vary from the angles 135° to 150° in the present energy region. This energy-dependent angular correlation distribution of the principal Rydberg series is related to that of doubly ionized states, which will be presented later. The

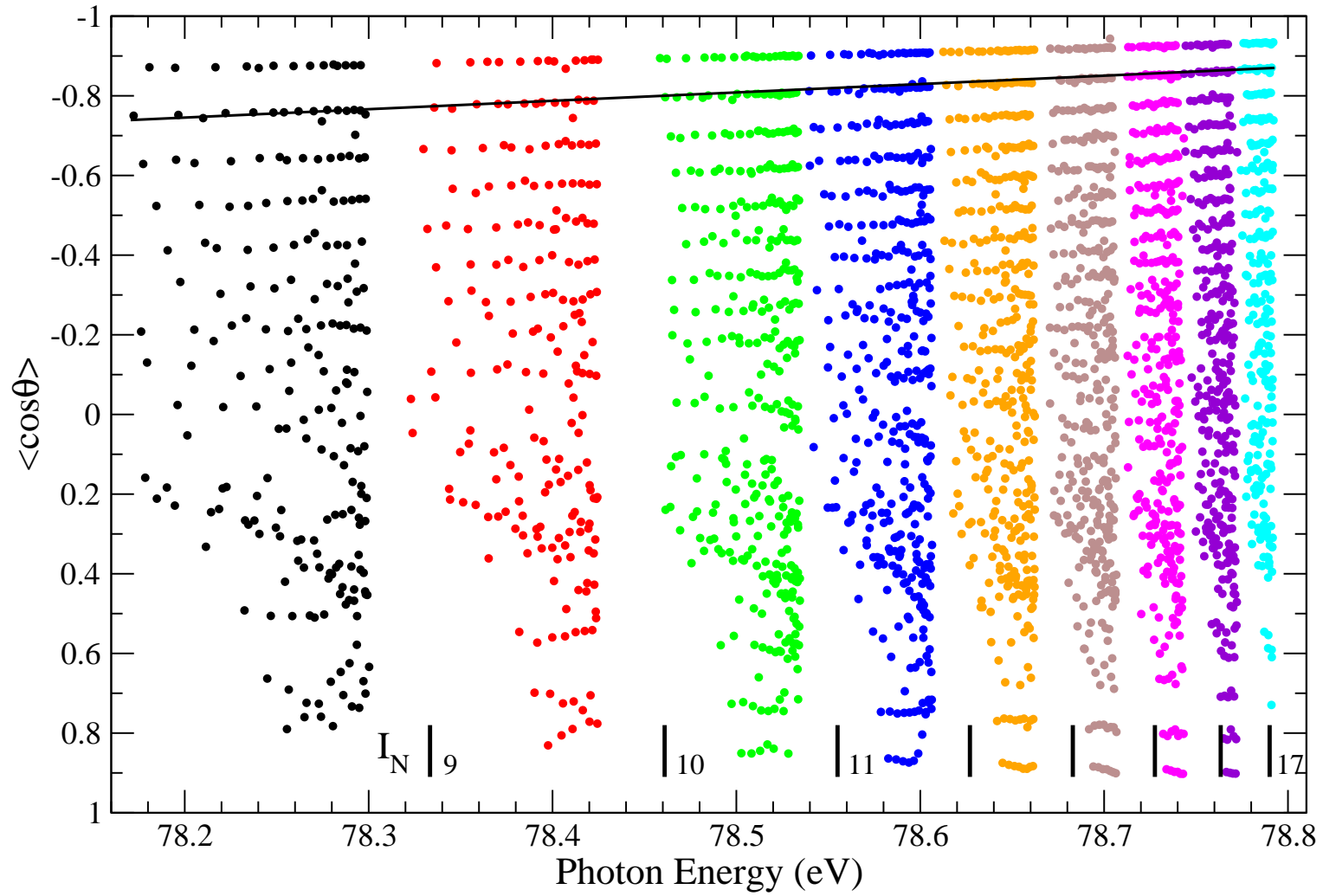


Figure 4.21: Calculated $\langle \cos \theta_{12} \rangle$ values as a function of photon energy below the SIT I_{17} . Each point represents one resonance, and the positions of single photoionization thresholds I_N are marked by thick vertical bars in the lower part of the figure. The principal Rydberg series is indicated by a solid black line.

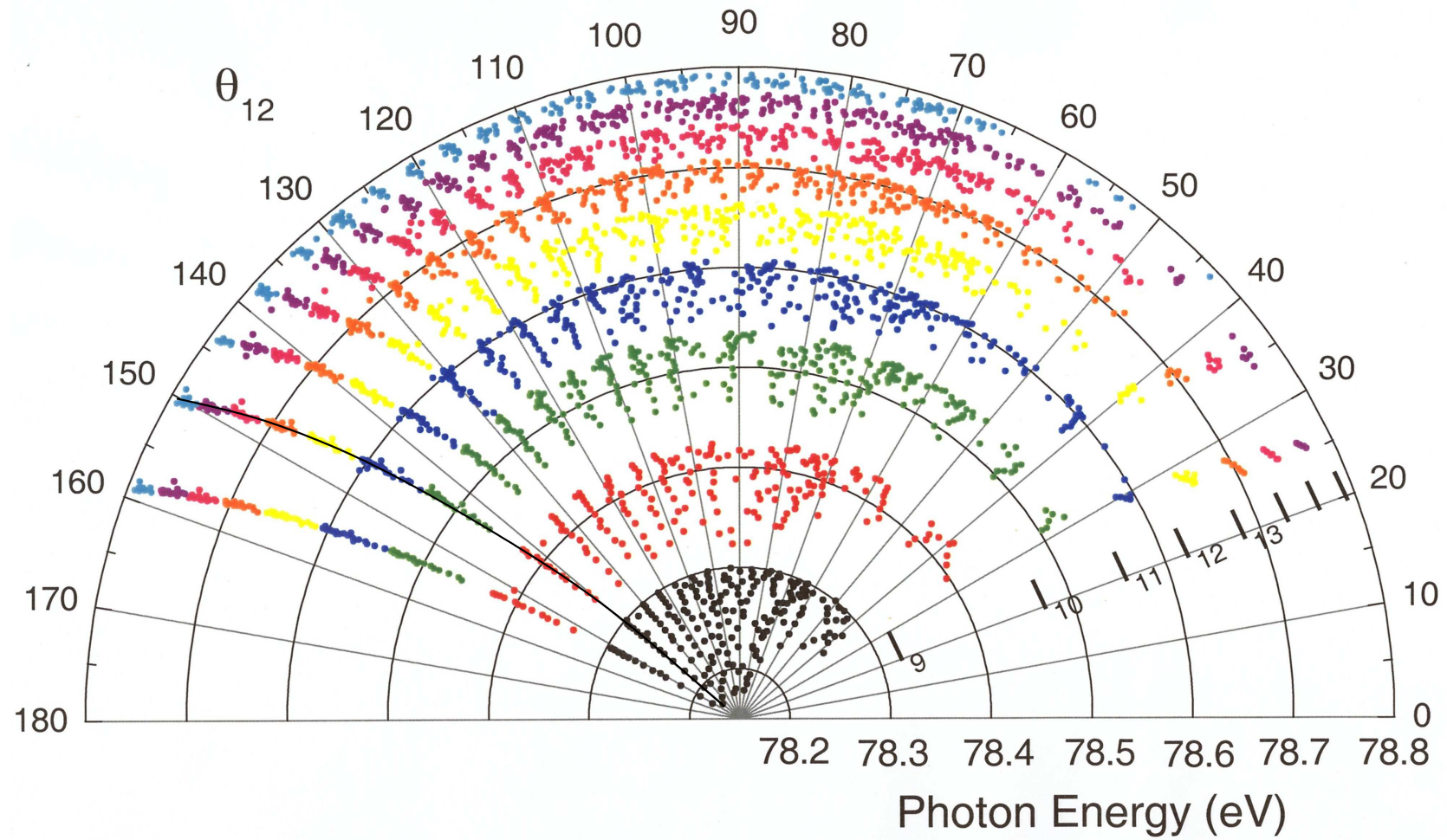


Figure 4.22: Calculated θ_{12} as a function of photon energy below the SIT I_{17} in a polar coordinate scheme. The principal Rydberg series is indicated by a solid black curve. This figure displays the same data as Fig. 4.21.

present discussion on the approximate quantum numbers N, K will be confirmed by the statistical analysis of the NNSs between resonances presented in the next section.

Under the assumption that all resonances are of comparable intensities, the cross section cannot be described by individual resonances. Instead, the cross section consists of fluctuations with a width equal to the typical linewidth, and it is composed of a large number of individual resonances. For helium, the prerequisite for Ericson fluctuations to be observed, which is the condition that the mean linewidth is much larger than the mean level spacing, is already fulfilled below the SIT I_9 [32]; this can be seen from an inspection of the data below the SIT I_{10} presented in Fig. 4.8. Therefore, the existence of Ericson fluctuations depends additionally on the condition that all resonances contribute equally to the spectra. From the previous discussion we know, however, that the spectra up to the SIT I_{14} are still dominated by the principal series ($K = N - 2$), and its K value is still a good quantum number. This is the reason why Ericson fluctuations cannot be found in this moment although the region concerned is in the Ericson regime. As mentioned before, we conclude in this dissertation it is very dangerous to discuss the Ericson fluctuations by an autocorrelation function fitted by a Lorentzian form before one is able to really confirm the prerequisites of the Ericson fluctuations, in particular for comparable intensities of resonances.

4.5.3 Statistical analysis of nearest-neighbor spacings

In the previous section, we concluded that K is a good quantum number for resonances with $K \rightarrow K_{max}$ and $K \rightarrow K_{min}$, but not for resonances with $K \rightarrow 0$. In addition, we found that N and n' are good quantum numbers only for resonances with $K \rightarrow K_{min}$. In this section, we shall employ statistical tools for the analysis of NNSs between resonances, linewidths, and Fano q parameters of resonances in order to further confirm these findings.

The integrated NNS distributions from a global analysis of resonances below the different SITs up to the SIT I_{16} , together with Wigner and Poisson distributions, are plotted in Fig. 4.23. For a clearer presentation, only curves for $N = \text{even}$ are plotted. Note that the thresholds with $N = \text{odd}$ exhibit the same distribution. In this context, “global” means that all resonances below a given ionization threshold, I_N , are taken into account without any restrictions for K . For example, the dotted line marked with $N = 10$ in the text of the figure is extracted from the NNSs between all resonances below the SIT I_{10} . In order to avoid misleading results from possibly missing resonances caused in the region close to each SIT, I_N , or in the beginning of each threshold, which can be caused by convergent problems in the calculations, only the resonances in the middle values of the n_{eff} range were considered in the statistical analysis. Below I_{10} , the dotted line was constructed only from resonances with $n_{eff} = 11$ to 20. An additional reason could be that the Rydberg series become more and more regular due to a small number of perturbers in the region extremely close to each SIT. However, the present calculated data cannot yet reach this region, which can be seen in Fig. 4.8 from the data below the I_{10} . All global NNS distributions below the SIT I_{16} , presented in Fig. 4.23, reveal a

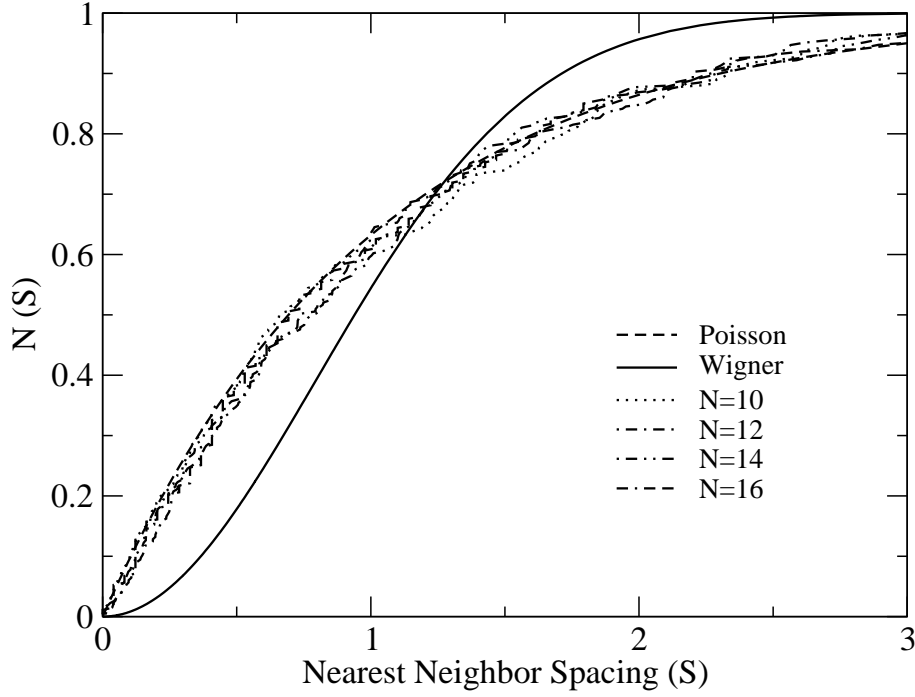


Figure 4.23: Integrated nearest-neighbor spacings (NNS) distributions $N(s)$ for the resonances below the SIT I_{16} using a global analysis. The global NNS distributions $N(s)$ for the resonances below the various SIT I_N are displayed together with a Wigner and a Poisson distribution representing a chaotic and a regular system, respectively.

Poisson form, which indicates that there are still independent subsystems, which can be classified by quantum numbers. From the discussion in the previous section, we know that K and N do not break down completely; there are some regions where they work quite well. In this case, the resonances can be considered to constitute several Rydberg series that are uncorrelated and may be distinguished by different quantum numbers K . Note that although K is mixed for the resonances with $K \rightarrow 0$, all of them can be regarded as one special "Rydberg series" equal to the one with a good K value. In summary, independent and uncorrelated Rydberg series constitute a "regular" system, whose the NNS distribution has a Poisson form. These independent and uncorrelated Rydberg series can be regular or chaotic [10]. In this way, the highest probability $P(S)$ for the NNSs of resonant energy levels occurs at $S = 0$, and then global NNS distributions exhibit a Poisson form (for details, see Sect. 4.2). In previous experimental and theoretical studies for the TCSs, Püttner *et al.* found a transition towards quantum chaos below the SIT I_9 [18]. The Poisson form of the NNSs up to I_{16} in the present study indicates that the transition region from integrability to chaos is much larger, since the quantum number K seem to dissolve rather slowly. Full chaos in $^1P^o$ doubly excited helium may appear at the double-ionization threshold. The trend approaching chaos is analogous to the situation in $^1S^e$ doubly excited helium [19].

The integrated individual NNS distributions for the resonances with $K \rightarrow K_{max}$ below the SIT I_{16} are given in Fig. 4.24. In addition, the curve for the regular Rydberg series

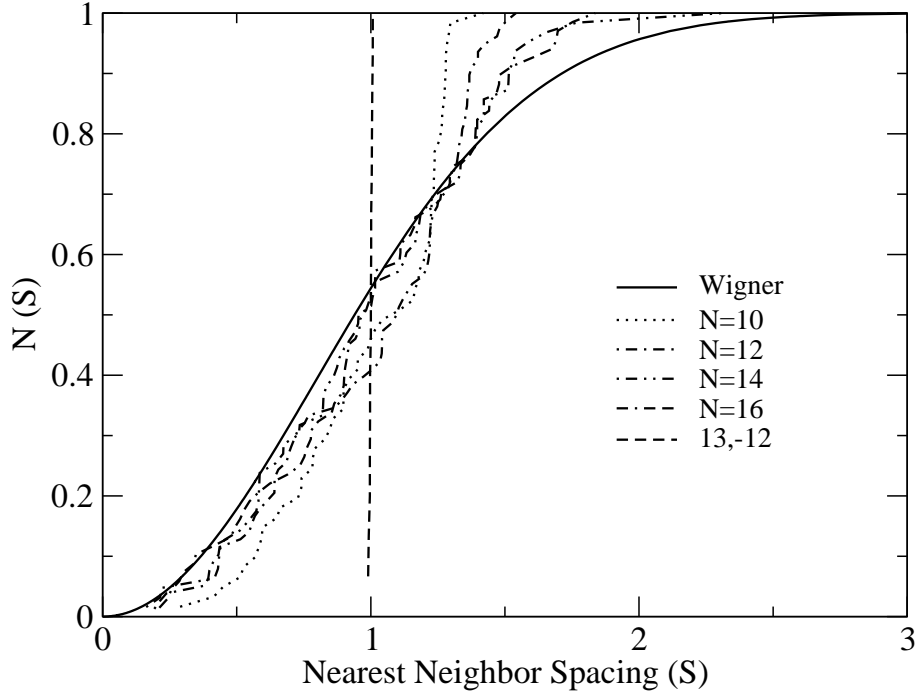


Figure 4.24: Integrated nearest-neighbor spacings (NNS) distributions for the resonances $K \rightarrow K_{max}$ below the SIT I_{16} using an individual analysis. The individual NNS distributions obtained for the resonances below the various SIT I_N , classified by good quantum numbers K , are shown together with a Wigner distribution representing a chaotic system. For comparison, the integrated NNS distribution for the regular Rydberg series $13, -12_{n'}$ is also shown.

$13, -12_{n'}$ is also displayed in this figure. In this context, “individual” means that the NNS distributions were obtained from the resonances below a given ionization threshold I_N that belong to a Rydberg series $N, K_{n'}$ with well-defined N and K . In a first step, the NNS distribution is obtained individually for each Rydberg series with well-defined K in the region of $K \rightarrow K_{max}$. In order to improve the statistics, the results obtained for the different Rydberg series are added, which results in the plots given in Fig. 4.24. For comparison, the NNS distribution for the regular Rydberg series $13, -12_{n'}$ is also given, which shows a perfect step function. The NNS distributions for the individual analysis of the Rydberg series with K close to K_{max} below the SITs I_{10} to the I_{16} exhibit a form between a step function and a Wigner function. Moreover, the NNS distributions approach a Wigner-like form with increasing ionization threshold I_N , which indicates that the radial quantum numbers N and n' dissolve completely in this region and lose their physics meanings. Since one K -selected Rydberg series, i.e. with the angle between the two electrons and nucleus fixed, can be considered to be a “1-D” case in 3-D helium, a Wigner-like form of K -selected NNS distributions for Rydberg series with $K \rightarrow K_{max}$ values is a quantum signature of chaos for the “1-D” case in real 3-D helium. These “1-D” cases in 3-D helium agree very well with those obtained from 1-D helium presented by Püttner *et al.* [18] and confirm their predictions that full Wigner distribution will be found around I_{17} .

In the region for $K \rightarrow 0$, Rydberg series with well-defined K values cannot be iden-

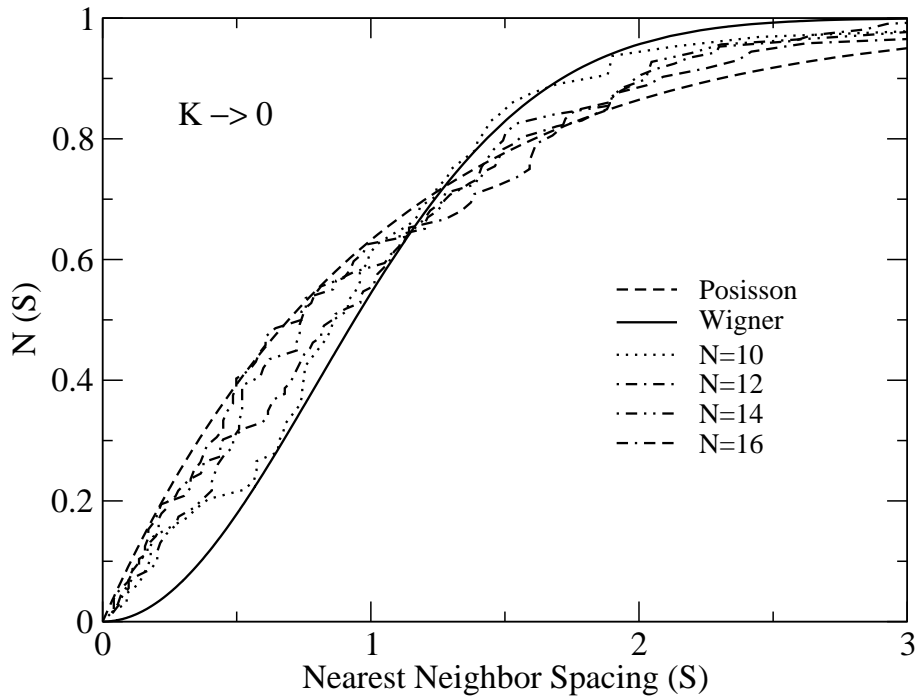


Figure 4.25: Integrated nearest-neighbor spacings (NNS) distributions $N(s)$ for the resonances $K \rightarrow 0$ below various thresholds up to the SIT I_{16} . The NNS distributions $N(s)$ for the resonances with $-4 < K < 2$ below a given SIT I_N are displayed together with a Wigner distribution and a Poisson distribution representing a chaotic and a regular system, respectively.

tified (see Figs. 4.16 to 4.20). Therefore, one would expect that a perfect Wigner distribution should be found in a statistical NNS analysis. Fig. 4.25 presents the NNS distributions for the resonances in the region of $K \rightarrow 0$ ($-4 < K < 2$) below the various SITs up to the SIT I_{16} . The NNS distribution for resonances below I_{10} is in quite good agreement with the Wigner form. Interestingly, the NNS distributions of resonances below higher ionization thresholds match a Poisson form quite well, see e.g. the curve obtained for the region below I_{16} . This is not understood at present.

In very recent calculations by Le *et al.* [19], statistical studies of the NNSs for $^1S^e$ doubly excited states were performed up to the SIT I_{19} , and the rate approaching a Wigner distribution was found to be slow, in agreement with the present situation for $^1P^o$ doubly excited states; this means that the transition region from integrability to chaos is much broader than previously expected.

4.5.4 Porter Thomas distribution of linewidths

The wave function of discrete states describing the doubly excited resonances can be regarded as representing the eigenvector in a Gaussian orthogonal ensemble (GOE), i.e. it can be described as the random element of matrices. Each eigenvector is of unit norm, and the statistical properties for the components of the eigenvector display a Porter-Thomas distribution [64, 82]. Since the widths Γ of the resonances are related to the eigenvector by Eq. (3.4), one has to assume that the probability $N(x)$ for width Γ exhibits

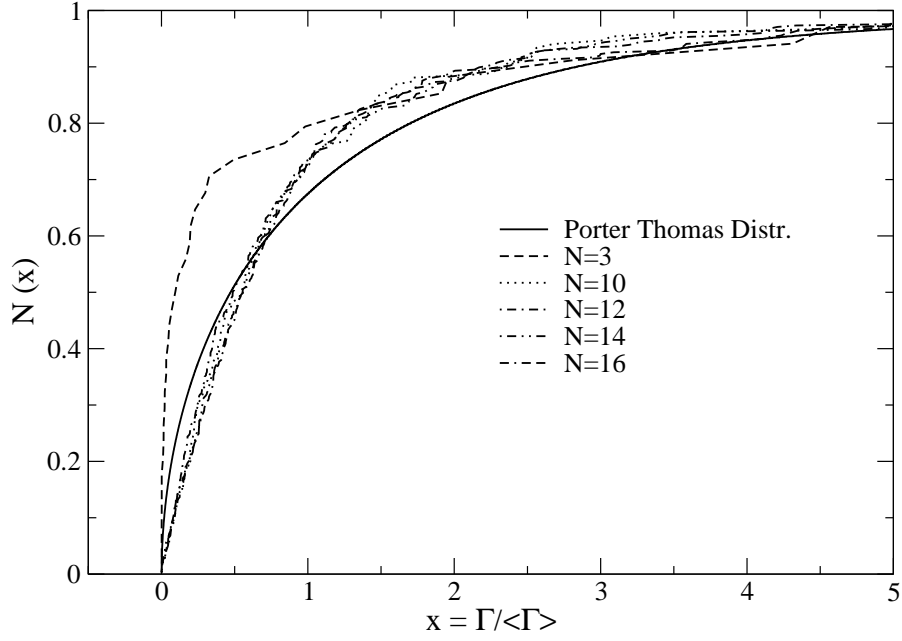


Figure 4.26: Statistical distributions $N(x)$ of resonant linewidths as a function of reduced width in the region below the SIT I_{16} . An integrated Porter-Thomas distribution, representing a chaotic system, is also plotted (solid line).

also a Porter-Thomas distribution [64, 82, 83] given by

$$P(x) = \frac{1}{\sqrt{2\pi x}} \exp(-x/2), \quad (4.13)$$

where $x = \Gamma/\langle\Gamma\rangle$ is the reduced linewidth. One can easily see that the smallest widths have the highest probability. This means that the strong statistical fluctuations in the random matrix tend to compensate each other, and the most probable value of a matrix element is zero. In order to improve statistics, we analyze the integrated form $N(x) = \int_0^x dx' P(x')$.

In Fig. 4.26, the statistical probability for the linewidth as a function of reduced width is displayed for the regions below the SITs I_3 and I_{10} up to I_{16} , together with the Porter-Thomas distribution that is plotted as a solid line. The shape of the distributions above I_{10} are almost identical and exhibit a fair agreement with the Porter-Thomas curve. Note that—for a clearer presentation—these statistical distributions are given only for thresholds I_N with $N = \text{even}$; the curves for $N = \text{odd}$ would show very similar shapes. The $N = 3$ region is regular, with five regular Rydberg series and no perturbors. The statistical probability distribution of the linewidths for the $N = 3$ region is quite different from the results below higher SITs. Interestingly, the eigenvector statistics for a kicked top under conditions that leads to a regular motion in the classical limit, which was presented in Fig. 4.3 of Ref. [65] shows a similar shape as the results for the $N = 3$ region of doubly excited helium given in Fig. 4.26. The lithium atom in a magnetic field was studied in Ref. [83], and the statistical properties of the observed linewidths were also well described by random matrix theory. So far, there are only rather limited data available for statistical studies of linewidths.

4.5.5 Lorentzian distribution of Fano q parameters

So far, we have focused on the statistics of level spacings and linewidths. A distribution of Fano q parameters in a chaotic system had been first derived by W. Ihra in 2002 [84]. According to Ihra's studies, the distribution of Fano q parameters can be derived under two prerequisites: First, the classical motion of high double-excitation resonances has to be chaotic. This ensures that the eigenstates of double-excitation resonances can be described by matrices taken from a Gaussian orthogonal ensemble in random matrix theory [84]. The statistical properties of the Fano q parameter are assumed to be determined by that of the eigenstates. Second, the excitation process and the coupling between a discrete state and final continuum states are assumed to be separated. Therefore, $x \equiv \langle \nu | r | i \rangle / \langle f | r | i \rangle$ and $y \equiv \pi \langle \nu | V | f \rangle$ can be taken as statistically independent random variables [84], where $q = x/y$ given in Eq. (3.5) and i , ν , and f are initial state, discrete state, and final continuum state, respectively. r represents the dipole operator, and the Coulomb operator V controls the autoionization process. The probability distribution for q is given by a Lorentz distribution [84]

$$P(q; w) = \frac{1}{\pi} \frac{w}{w^2 + (q - \bar{q})^2}, \quad (4.14)$$

where $w \equiv \sigma_x / \sigma_y$ is the width of the probability related to the coupling strength V between the discrete states and the continuum states as well as the ratio of the dipole transition matrix to the discrete state and the final continuum states. $\sigma_x(\sigma_y)$ are the variances of the variables $x(y)$. For a strong coupling to the continuum state, i.e. for σ_y being large, the Lorentzian distribution has a small width centered around \bar{q} . The same holds if direct photoexcitation dominates over the indirect process because of small σ_x . Of course, in most cases the change of w depends on the competition between direct

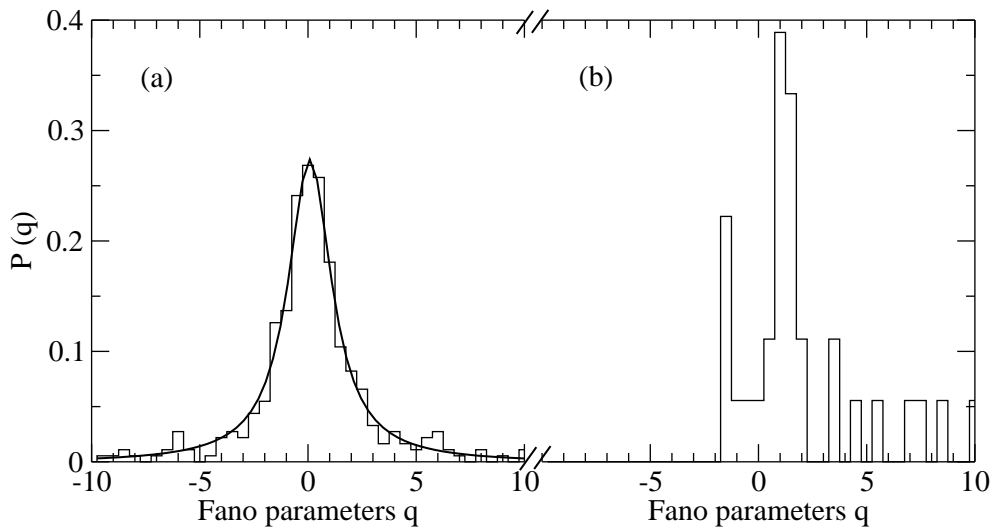


Figure 4.27: Statistical distributions of Fano q parameters (a) below I_{14} and (b) below the SIT I_3 . The statistical distribution of q below the SIT I_{14} is fitted by a Lorentzian function plotted as a solid line.

photoexcitation and indirect photoexcitation paths because normally the variations in both decays follow the same direction.

Table 4.1: Widths w and average value \bar{q} extracted from Lorentzian fits to the distributions of Fano q parameters for the various SITs up to I_{17} . The values for the Fano q parameter were taken from the results of the complex-rotation calculations [27].

SITs	w	\bar{q}
I_9	2.7	-0.28
I_{10}	2.1	-0.02
I_{11}	2.3	-0.09
I_{12}	2.7	0.10
I_{13}	2.2	0.03
I_{14}	2.5	0.09
I_{15}	2.2	-0.07
I_{16}	2.0	0.15
I_{17}	2.1	-0.05

Statistical distributions of Fano q parameters up to the SIT I_{17} were performed; the results obtained for the SIT I_{14} are shown in Fig. 4.27(a), as an example. The distribution of q below the SIT I_{14} can be described quite well by a Lorentzian function, with \bar{q} close to 0, as predicted by W. Ihra [84]. The distributions in the region between I_9 and I_{17} also match quite well a Lorentzian distribution, with \bar{q} close to 0. In contrast to the distribution of q in the regions of high doubly excited helium, the distribution of q below the SIT I_3 is plotted in Fig. 4.27(b). This statistical distribution is dominated by three peaks around q values of -1.5 , 1.0 , and 1.5 , which correspond to the three regular Rydberg series $3, -2_{n'}$, $3, 0_{n'}$, and $3, 1_{n'}$, respectively. Normally, all members of a regular Rydberg series have similar values of q and, therefore, their distributions do not match a Lorentzian form. The widths w of the statistical distribution for all regions below I_9 to I_{17} are obtained from the fits, and they are summarized in Tab. 4.1. Due to increasing coupling strength to continuum states, w slowly decreases with increasing ionization threshold. These spectra are predicted by Eq. (4.14), while the corresponding classical system is chaotic. To our knowledge, this is the first confirmation of this prediction, and further detailed studies have to be done in the near future.

4.6 The angular correlation mechanism around the double-ionization threshold

The study of electron correlation in the photon-induced double-ionization process of helium has been a topic of considerable interest in the last couple of decades [85–101].

In particular in the vicinity of the double ionization threshold (DIT), it is expected that the double-ionization process is related to a single-ionization process enhanced by the doubly excited states. In 1999, Qiu and Burgdörfer [97] extended the group-theoretical approach for a classification of doubly excited states below the DIT, discussed in Sect. 3.2, to two-electron continuum states above this threshold. This extension allows an extrapolation of angular correlation properties of doubly excited states beyond the DIT, with the result that they can be used to describe doubly ionized states. The propensity rules for the $A = +1$ or -1 symmetries, known for doubly excited resonances, were also found to be suited to perfectly describe the near-threshold behavior of the photon-induced double-ionization process [94]; an interpretation of the quantum number A has been given in Sect. 3.2.2. In this dissertation, we shall show how the angular correlation behavior of doubly excited states below the DIT is extrapolated to doubly ionized states beyond the DIT. Here, we first discuss the triple differential cross section (TDCS) patterns for the double ionization process, from which the angular correlation patterns can be derived.

For linearly polarized light, Huetz *et al.* [90] first established the TDCSs as

$$d\sigma(E_1, E_2, \theta_{12}) = |a_+(E_1, E_2)(\cos\theta_1 + \cos\theta_2) + a_-(E_2, E_1)(\cos\theta_1 - \cos\theta_2)|^2, \quad (4.15)$$

where θ_{12} is the angle between the two outgoing electrons. The angles θ_i ($i = 1$ and 2) are the angles of the two electrons with respect to the polarization vector of the light and $E_{1,2}$ are their respective kinetic energies. The amplitudes a_+ and a_- describe transitions to states with $A = +1$ and -1 , respectively. Note that quantum number A corresponds to the symmetry of the wave function for doubly excited states under the exchange $r_1 \leftrightarrow r_2$, and that it has the same value as for doubly ionized states under the equivalent exchange $E_1 \leftrightarrow E_2$ [98]. Here, $r_{1,2}$ represent the absolute values of the distances between the two electrons and the nucleus. For equal energy sharing, i.e. $E_1 = E_2 = E_{ex}/2$, it has been observed [92, 93, 96, 99] that the second amplitude in Eq. (4.15) vanishes if one approaches the DIT, in agreement with the Wannier law [85, 87, 91]. Therefore, for equal energy sharing the TDCSs, given in Eq. (4.15), are written as

$$d\sigma(E_{ex}, \theta_{12}) = C_{E_{ex}}(\theta_{12})(\cos\theta_1 + \cos\theta_2)^2. \quad (4.16)$$

The correlation factor,

$$C_{E_{ex}} \propto \exp(-4\ln 2(\theta_{12} - 180^\circ)^2/\theta_{FWHM}^2), \quad \text{with } \theta_{FWHM} = \theta_0 E_{ex}^{1/4}, \quad (4.17)$$

has a Gaussian distribution with a width θ_{FWHM} that is related to the excess energy, E_{ex} . The value of the scaled width parameter, θ_0 , obtained by different authors, varies from $\theta_0 = 103 \text{ deg (eV)}^{-1/4}$ [86] to $66.7 \text{ deg (eV)}^{-1/4}$ [88]. Equation (4.16) for the case of equal energy sharing can also be used as a good approximation for unequal energy sharing if $E_{ex} \rightarrow 0$ [98]; this has been confirmed by experimental data [90, 92, 93, 96, 99]. It implies that in this region the amplitude a_- in Eq. (4.15) is much smaller than a_+ , and in addition, a_+ is insensitive to E_1/E_2 , i.e. $a_+(E_1 = E_2) \cong a_+(E_1 \neq E_2)$. Here, the cases of equal energy sharing ($E_1 = E_2$) and of unequal energy sharing ($E_1 \neq E_2$) of doubly

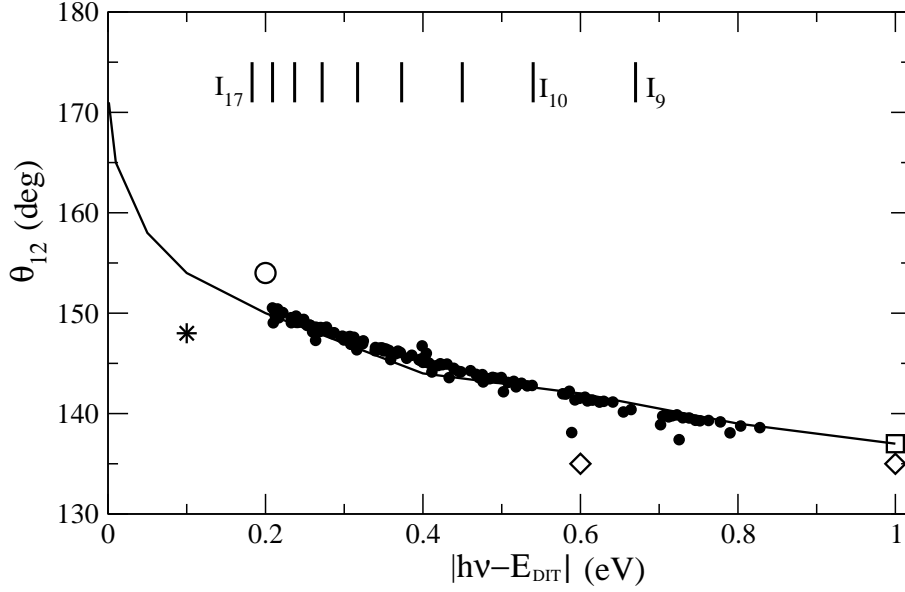


Figure 4.28: Angular correlation parameter, θ_{12} , as a function of energy close to the double-ionization threshold. The filled points represent the calculated doubly excited resonances of the principal Rydberg series $K = N - 2$ from the SITs I_9 to I_{17} ; these were indicated in Figs. 4.21 and 4.22 by solid lines. The solid line represents the angular correlation parameter of doubly ionized states taken from Eq. (4.16) by setting $\theta_0 = 80 \text{ deg (eV)}^{-1/4}$. Experimental data for doubly ionized states with $E_{ex} = 2E_1 = 2E_2 = 0.1, 0.6$, and 1.0 eV , respectively, are given by a star [99], an open diamond [93], and an open box [96]; in addition, an open circle represents the result of theoretical calculations by Qiu and Burgdörfer [97]. The positions of single photoionization thresholds, I_N , are marked by vertical bars in the upper part of this figure.

ionized states are equivalent to doubly excited states for two electrons with the same and the different values of the principal quantum numbers N and n' , respectively.

In the previous section, we confirmed that the cross section below the DIT is dominated – at least up to the SIT I_{14} – by the principal series $K = N - 2$, which corresponds to the classical collinear eZe configuration. Close to the double-ionization threshold, the angle θ_{12} for the principal series $K = N - 2$ increases strongly and reaches 180° directly at the DIT (see Fig. 4.22). Therefore, the collinear eZe configuration can be considered to be the most likely one in the vicinity of the DIT. We want to point out that the wave function for the principal series $K = N - 2$ is of $A = +1$ symmetry matching perfectly with the most intense double ionization channels above the DIT, where the amplitude with $A = +1$ symmetry dominates the TDCSs resulting in Eq. (4.16).

In the following, We discuss similarities in the angular correlation properties of the doubly excited states below the DIT and of the doubly ionized states above this threshold. Figure 4.28 displays the energy-dependent angular distribution near the DIT, i.e. the value of θ_{12} as a function of the relative energy, $|h\nu - E_{DIT}|$, for an approach from above and below this threshold. $E_{DIT} \cong 79 \text{ eV}$ is the DIT of helium. The filled points represent the calculated doubly excited resonances of the principal Rydberg series $K = N - 2$ from

below the SITs I_9 to I_{17} , which are indicated in Figs. 4.21 and 4.22 by solid lines. The changes of θ_{12} for the principal Rydberg series of the doubly excited states are in good agreement with theoretical values for the doubly ionized states, which is given by the solid curve taken from Eq. (4.16) by setting $\theta_1 = 90^\circ$ and $\theta_0 = 80 \text{ deg (eV)}^{-1/4}$. The value $\theta_0 = 80 \text{ deg (eV)}^{-1/4}$ agrees with the experimental [93] and theoretical [89] values at $E_{ex} \cong 0.6 \text{ eV}$. The experimental data for $E_{ex} = 0.1, 0.6$, and 1.0 eV , respectively, are represented in this figure by a star [99], an open diamond [93], and an open box [96]. The open circle is taken from the theoretical predictions for the doubly ionized states given by Qiu and Burgdörfer [97]. We note from Eq. (4.16) that θ_{12} depends only slightly on θ_1 , but shows a strong dependence on E_{ex} . The simulation on the basis of this equation showed that θ_{12} has a maximum value at $\theta_1 = 90^\circ$ for a constant value of E_{ex} . The experimental TDCSs of Ref. [93] were not measured at $\theta_1 = 90^\circ$, which have resulted in smaller values of θ_{12} as indicated by the open diamond in Fig. 4.28. In fact, the angular distribution parameter, β , has been confirmed to approach -1 by approaching the DIT from both above [94, 95] and below [102], i.e. the highest probability for the outgoing electrons is at $\theta_1 = 90^\circ$ with respect to the polarization of light.

In addition, the excess energies, E_{ex} , of the two ionized electrons above the DIT correspond to the binding energies of the doubly excited states below the DIT. Therefore, the doubly excited resonances close to single ionization, i.e. the ones with $n' \gg N$, can be regarded as the counterpart of unequal energy sharing in the double-ionization process. The theoretical results for doubly excited states, presented in Fig. 4.28, show that θ_{12} does not change much below one single ionization threshold. This observation corresponds to the fact that for doubly ionized states close to the DIT θ_{12} is also insensitive to the ratio E_1/E_2 [92, 93]. Considering all these facts, the available experimental results above the DIT and the theoretical results below the DIT are in agreement with those derived from the analytical expression given in Eq. (4.16). Figure 4.28 shows clearly that the angular correlation around the DIT has a mirroring behavior taking the DIT as the mirroring axis. This mirroring angular correlation dynamics around the DIT further improves the understanding to the double-ionization dynamics of helium: the preferential double-ionization path should be the one where the two electrons escape symmetrically and back-to-back. In order to confirm this prediction on the mirroring angular correlation dynamics, more experimental and theoretical work on the TDCSs at $E_{ex} \leq 1 \text{ eV}$ is needed, in particular for $\theta_1 = 90^\circ$.

Because of the $^1P^\circ$ symmetry, θ_{12} for the equal-energy-sharing case is not equal to 180° , even at the DIT, i.e. the TDCSs have a node at $\theta_{12} = 180^\circ$ on the basis of standard quantum mechanics [98]. As mentioned in Append. A, in the limit of the DIT, the quantum description of helium should lead to a classical mechanical case (Bohr's correspondence principle). This may be considered to be the signature of classical mechanics in the quantum helium system, when E approaches the DIT.

Chapter 5

Photoionization spectroscopy by TOF measurements

In the preceding chapter, we have discussed the present experimental results for the TCS up to the SIT I_{15} along with theoretical calculations up to the SIT I_{17} of helium. The most important physics is the observation of features caused by quantum chaos in the simplest multibody system, namely the two-electron system such as He atom. However, all these studies were performed with statistical tools, such as the NNS distribution of energy levels, the Lorentzian distribution of Fano q parameters, and the Porter-Thomas function of resonant linewidths. Since only a small fraction of the resonances can be observed experimentally, most of these statistical studies were made on the basis of theoretical results. Therefore, experimental studies of the PCSs σ_n and ADPs β_n can substantiate theoretical methods and assure the validity of these statistical analysis derived from theoretical data. In addition, since the PCSs and ADPs carry additional coupling information of the outgoing channels, quantum chaos is expected to manifest itself more easily or in different ways than in the TCSs. Vice versa, the success of the present experimental and theoretical studies on the TCSs in this highly excited region will encourage studies of PCSs and ADPs.

Due to various couplings among the outgoing channels, the PCSs, σ_n and the ADPs, β_n , are more sensitive to the quality of the wave functions and theoretical methods than the TCS, σ_T , and therefore represent the most critical assessment of the theoretical methods. Moreover, because each decay channel can be influenced in a different way, the σ_n and β_n are more sensitive to the influences of perturbers. As a result, more resonances with pronounced variations are expected in σ_n than σ_T . As an example, the resonance $8, 4_{10}$ of the secondary series is resolved in the present PCS measurements in contrast to the TCS data, although latter were measured with better resolution and signal-to-noise ratio [30].

Similarities in the variations of the PCSs and the ADPs caused by the resonances in the energy region up to the SIT I_5 were observed for the first time by Menzel *et al.* [34, 35]. These so-called 'general patterns' can be well understood by the propensity rules for autoionization based on the molecular adiabatic approximations [33] (see Sect.

5.3.3). As the photon energy increases, the structures in the PCSs get more complicated due to interferences caused by an increasing number of perturbors, and the general patterns begin to dissolve. An experimental confirmation of these theoretical predictions requires high-resolution photoemission measurements at the energies beyond the ionization threshold I_5 .

In addition, in the photon energy region below the SIT I_6 , the mirroring behavior in the PCSs for the double-excitation resonances has become an interesting topic in recent years since Liu and Starace developed an analytical expression for it [36]. The mirroring behavior means that the variations in the vicinity of a resonance between any two PCSs exhibit a very similar behavior. The sum of these two PCSs is the TCS. In this dissertation, we shall extend the analytical expression of Ref. [36] to a general case, which allows us to understand completely the mirroring behavior in the n -specific PCS as well as in the l -specific PCS given in last chapter of the dissertation.

Due to the reasons mentioned above, the PCSs in region of the last eV below the double-ionization threshold have drawn considerable attention both in experimental and theoretical studies. The incentive for the present work was the insight that an analysis of the propensity rules and of the mirroring behavior of PCSs as well as the ADPs of autoionizing double-excitation states in helium can provide a deep understanding of the decay dynamics of two-electron atoms. First measurements of PCSs of He had been performed by Lindle *et al.* [103]; these studies, however, were limited to excitations approaching the ionization limit I_3 , due to the low photon intensities achieved at the first-generation light sources available at that time. Menzel *et al.* then reported on the measurements of PCSs and ADPs up to the SIT I_5 employing two spherical-sector-plate electrostatic analyzers [34, 35]. Czasch *et al.* [102] studied the photon energy region from the SITs I_9 to I_{16} . In the present dissertation, we extend the experimental studies of PCSs up to the SIT I_9 [37, 104] and of ADPs up to the SIT I_7 , filling the gap between Menzel's measurements and the experimental results of Czasch *et al.*. The PCSs and ADPs presented in this dissertation were derived from photoemission spectra taken by a TOF electron spectrometer. The results of state-of-the-art R-matrix calculations, performed by T. Schneider and partly presented in Ref. [33], are also displayed along with the experimental results for the PCSs. Other calculations were performed by van der Hart *et al.* [63], who published their results for σ_n up to the SIT I_9 . To our knowledge, no calculations and measurements are available for a comparison with the present experimental results for the ADPs above the SIT I_5 .

5.1 Experimental set-up

State-of-the-art high-resolution monochromators in combination with TOF photoelectron spectrometers allow one to explore the autoionization of resonances in the highly excited region. Here, we present photoelectron emission measurements and extract the various PCSs below the SIT I_9 and the ADP below the SIT I_7 from the recorded spectra. The experiments were performed at the undulator beamline U125/2-SGM (BUS-

beamline) [50] of the Berliner Elektronenspeicherring für Synchrotronstrahlung (BESSY) using a photon energy resolution of $\Omega \cong 6$ meV (FWHM). The optical layout of the BUS beamline is displayed in Fig. 2.4, and the exit slit was set to a value of $\cong 40$ μm . A needle (10 cm long, less than 500 μm inner diameter) directs an effusive jet of gas to the interaction region; the background pressure in the chamber was $\cong 10^{-4}$ mbar. From the count rate and calculated cross sections, we estimate the pressure in the interaction region to be of the order of 10^{-2} mbar.

For the measurements of the PCS, one TOF spectrometer [22] was mounted at the magic angle, i.e. in the dipole plane at an angle of $\theta = 54.7^\circ$ relative to the polarization direction of the incoming light. The schematics of the experimental set-up for a measurement of PCSs and a corresponding photograph from the inside of the experimental chamber is displayed in Fig. 5.1. The TOF spectrometer shown in this figure was used for the PCS measurements. For this geometry equation (1.22) reveals that the angular distribution causes no effect on the derived PCSs.

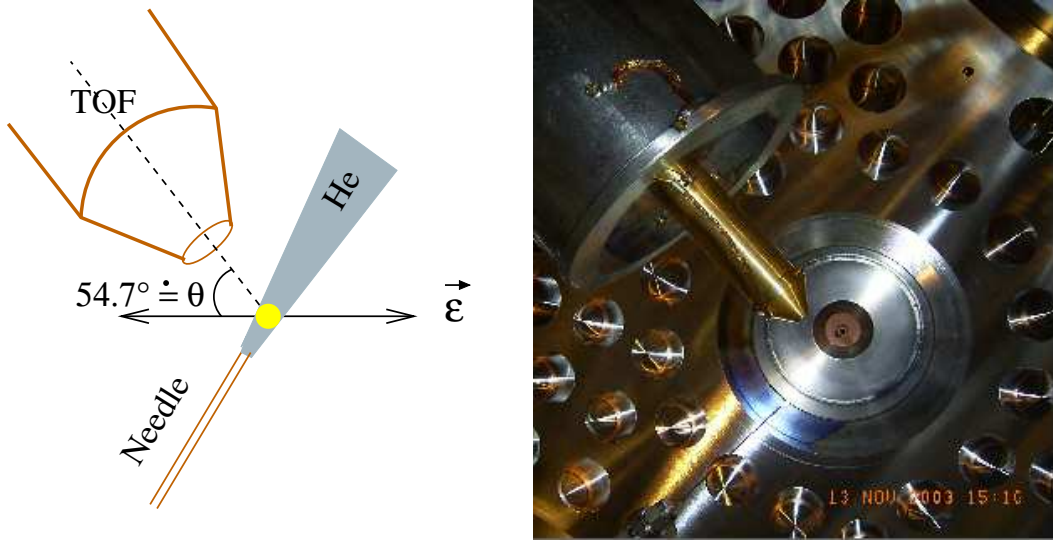


Figure 5.1: Schematics of the experimental set-up for PCS measurements and corresponding photograph from the inside of the experimental chamber. The propagation direction of the light is out of the paper plane; the polarization is horizontal as shown in the drawing on the left hand side.

Equation (1.22) contains the two parameters, σ_n and β_n . For a measurement of the β -parameters, at least two TOF detectors are needed to take differential cross sections (DCS) $d\sigma/d\Omega$. To improve the statistics and to reduce systematic errors, more analyzers can be mounted and used for taking data simultaneously. Figures 5.2 and 5.3 show photographs of the experimental ball chamber from the outside and from the inside, respectively; this chamber was used for the measurements of β -parameter below the SIT I_7 . A number of TOF spectrometers [22] were mounted at various angles in the dipole plane perpendicular to the propagation of light. The TOF spectrometers mounted on the upper half of ball chamber can be seen in Figs. 5.2. The structure of these TOF

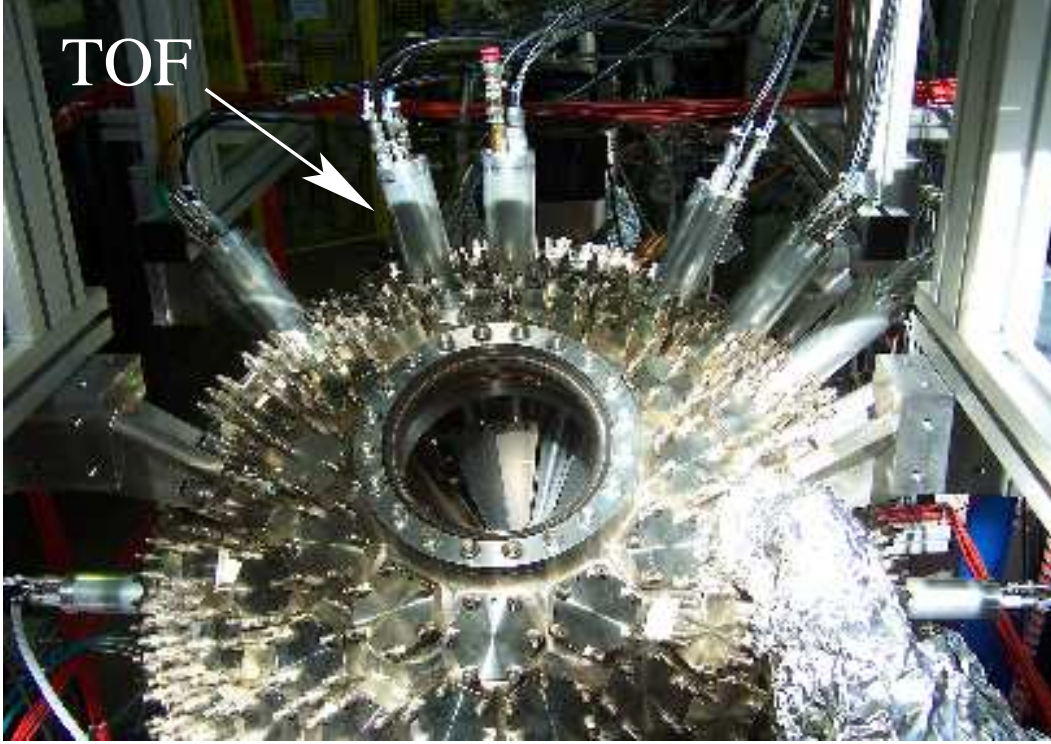


Figure 5.2: The outside of the ball-chamber for the measurements of the DCSs and ADPs. 8 TOF photoelectron spectrometers are seen in the figure.

spectrometers is identical, and the flight tube inside the chamber is about 30 cm long. A ring centered inside the chamber ensures that all TOF spectrometers are mounted at equal distances. One of the TOF spectrometers is normally mounted at the magic angle, and can be used to determine the PCSs directly.

To increase the transmission for the electrons with low kinetic energies, three accelerating voltages were applied on each TOF spectrometers, and normally their values were set individually between 1 and 3 V (see Fig. 2.7). In addition, a potential of $\cong 0.5$ V could be applied to the needle of gas inlet in order to increase the transmission. To compensate the earth magnetic field, three pairs of Helmholtz coils were installed. This is necessary because the order of the magnetic field of the earth in the interaction region would strongly reduce the photoelectron transmission, in particular for those photoelectrons with low kinetic energy. With $\beta_2 \cong 0$ [105], the $n = 2$ satellite of the time spectrum of helium in the photon energy region directly above the SIT I_2 can be used for the adjustments of the magnetic compensation since the corresponding electrons have a very low kinetic energy and a quite high count rate. For the ADP measurements, a number of TOFs was mounted at various angles. Under this condition, the adjustment of magnetic field compensation leads normally to an increase in the transmissions of some TOF spectrometers, while for others the transmission gets worse. Therefore, after the general adjustment of magnetic fields, the relative transmission of each individual TOF

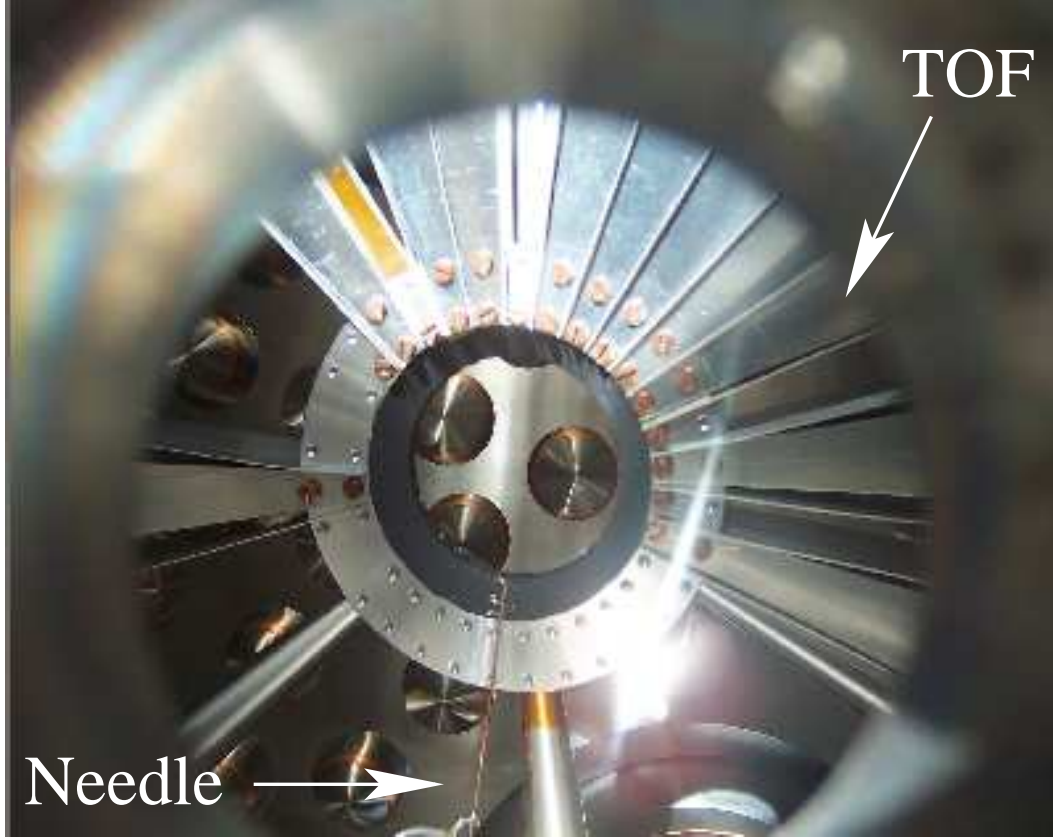


Figure 5.3: The inside of the ball-chamber with 12 TOF photoelectron spectrometers mounted.

has to be determined; this will be discussed later.

5.2 Data acquisition

In order to eliminate the influences caused by the decrease of the ring current and fluctuations of the gas pressure in the interaction region during data taking, the time spectra have to be normalized before converted into energy spectra by the time-to-energy conversion introduced in Sect. 2.4.3. Ideally, we could use the 1s-line of the various TOF spectrometers, mounted at different angles to normalize the intensities of the other satellite lines, since σ_1 can be assumed to be structureless. However, according to $\beta_{1s} = 2$, the 1s-line is absent in the 90°-TOF spectrum. Assuming that the count rates of all satellites in all TOF spectra are influenced in the same way by the photon flux and the target pressure, one can also use the intensity of the 1s-line of any TOF spectrum for normalization of the time spectrum of the 90°-spectrometer. In practice, the 1s-line of the 0°-TOF spectrometer is used for normalization because of the highest count rate. Based on theoretical results which show some weak resonances in σ_1 , we can estimate that the error produced by this procedure is $\leq 10\%$ for measurements below

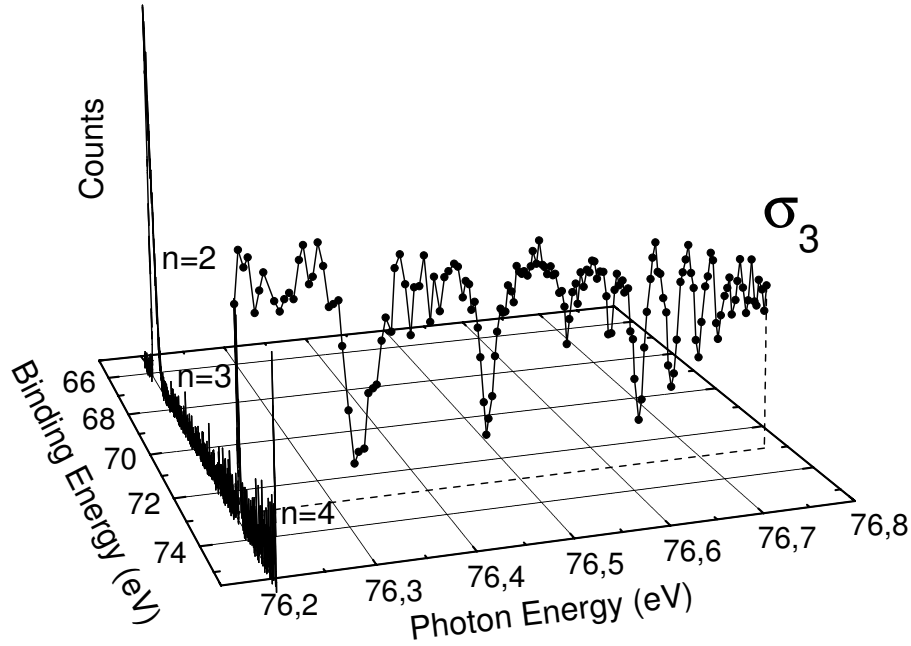


Figure 5.4: The spectrum along the binding energy axis represents an experimental photoemission spectrum recorded at $h\nu = 76.2$ eV, with the satellites $n = 2$ to 4 representing the ionic final states of $\text{He}^+(n)$. The solid curve through the data points represents the PCS σ_3 that can be derived from a large number of such photoemission spectra (not shown here) recorded at different photon energies. For details see text.

the ionization threshold I_5 , $\leq 6\%$ below I_6 , $\leq 7\%$ below I_7 , $\leq 3\%$ below I_8 , and $\leq 2\%$ below I_9 .

After normalization, the second step of the data analysis procedure is to determine the efficiency factors for the different TOF spectrometer. This is particularly important for measurement of the β parameter. These efficiency factors are determined by comparing the intensities of the $1s$ line due to its high kinetic energy and the energy independence of the efficiency factor of a TOF (see Sect. 2.4.3).

As an example, an experimental photoemission spectrum (PES), taken with $h\nu = 76.2$ eV, is presented in Fig. 5.4 in form of a three-dimensional plot. From the PES, the integral intensities of the satellite peaks, i.e. $n \geq 2$, can be extracted and plotted as a function of photon energy, resulting in the PCS σ_n . As shown in Fig. 5.4 for the example of σ_3 , the PCS was derived from approximately one hundred PESs, and each point in the PCS corresponds to one PES with different photon energies. Since the measuring time for one PES spectrum is of the order of 5 to 10 minutes, the data acquisition for the PCSs below one ionization threshold takes several ten hours.

5.3 Channel-resolved measurements up to I_9

In this section, we present the results of PCS measurements below the SITs I_5 to I_9 of He. General pattern and mirroring behavior in the PCSs will be the topics in this part of

the dissertation. With these PCS studies, we are expecting to improve the understanding for electron correlations and autoionization decay dynamics in this two-electron system.

5.3.1 Partial cross sections

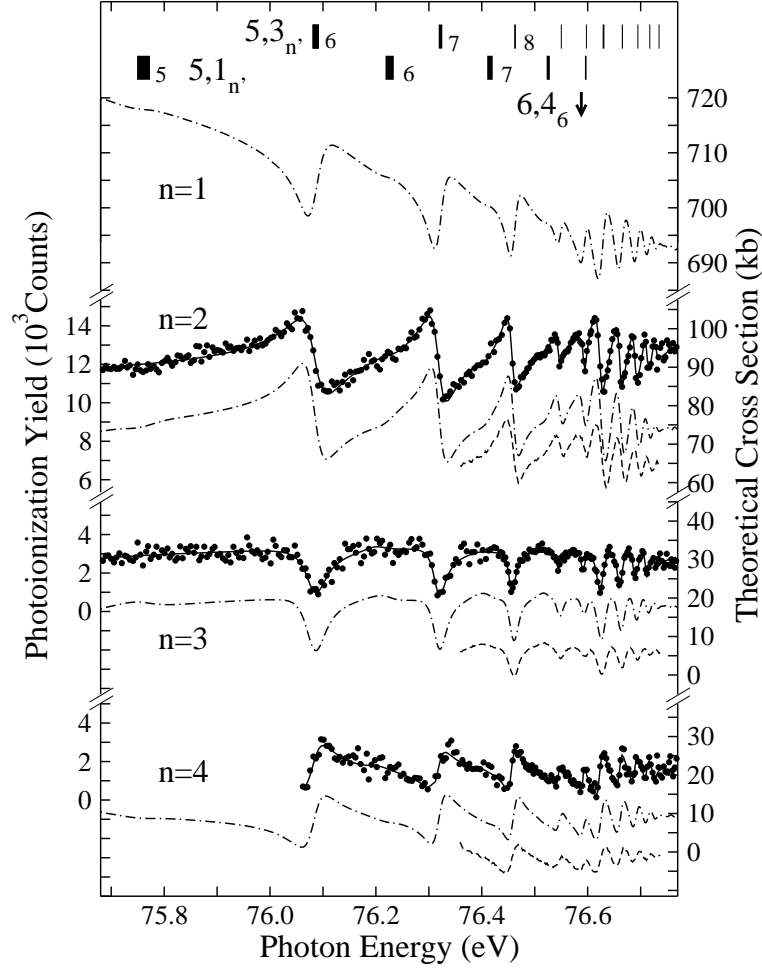


Figure 5.5: Experimental partial cross sections, σ_n^5 , leading to the final states $\text{He}^+(n)$, with $n = 2, 3$, and 4 , along with the results of the eigenchannel R-matrix calculations performed by T. Schneider [33]. The data were taken in the photon-energy region between 75.68 eV and 76.77 eV. The two vertical-bar diagrams in the upper part of the figure give the assignments of the double-excitation resonances by specifying n' ; with the widths of bars being proportional to the linewidths of the corresponding resonances [31]. The vertical arrow in the upper right corner marks the calculated energy of the perturber $6, 4_6$. The filled data points are the present experimental results, with the solid curves through the data points representing the fit results. The dashed curves represent the data by Menzel *et al.* [34] and the dash-dotted curves the results of the R-Matrix calculations convoluted with a Gaussian of 6 meV width (FWHM) to simulate finite experimental resolution.

As mentioned before, the Fano formula given in Eq. (3.3), which has been developed for describing the lineshapes of resonances in the TCS, has the same mathematical structure as the exact formula by Starace given in Eq. (3.8) for describing the resonances

in the PCS [59]. As a consequence, it is possible to describe the PCS by the Fano formula, but in this case, q represents only an effective parameter without a deeper physical meaning. In analyzing our data, we fitted the various PCSs for a given energy region by the Fano formula in a parallel least-squares fit procedure using a single Gaussian to simulate the experimental resolution function. In this way, the σ_n leading to different final states of $\text{He}^+(n)$ were fitted to Eq. (3.3) with the same experimental resolution Ω , energy position E_r , and linewidth Γ , but different Fano q parameters. The results of this fit procedure are given as solid curves through the data points in Figs. 5.5 to 5.9. The data below the SITs I_5 to I_7 were calibrated at the energy of resonance $5, 3_6$ (76.083 meV) as given by Domke *et al.* [30], and photon energies below the SITs I_8 and I_9 were calibrated to theoretical results [32].

The present experimental data together with theoretical calculations from the eigen-channel R-matrix calculations by Schneider *et al.* [33] and previous measurements by Menzel *et al.* [34] are presented in Figs. 5.5 to 5.9 by the solid points, dash-dotted curves, and dashed curves, respectively. The least-squares-fit results are described by solid lines through the data points in these figures. The results of R-matrix calculations are convoluted with a Gaussian of 6 meV width (FWHM) to simulate experimental resolution; they are given in units of kb on the right ordinate. The basic idea of the R-matrix method has been described in chapter 6.1, and the details for the configurations of the target are in the publication of Schneider *et al.* [33]. Note that, in order to match the experimental data to the theoretical PCSs below the SITs I_6 to I_9 , the latter had to be shifted to higher energy by 4 meV, 12 meV, 12 meV, and 10 meV, respectively.

Note that for convenience we employ in our discussion the notation σ_n^N to label the different PCSs. As defined above, the lower index n ($n = 1, 2, 3, \dots, N - 1$) refers to the principal quantum number of the single electron in the ionized final state, $\text{He}^+(n)$. N is the quantum number of the inner electron in the doubly excited states, i.e. the corresponding data are measured below the ionization threshold I_N . Fig. 5.5 displays the results of the present work for the PCSs σ_n^5 (with $n = 2, 3$, and 4). The error bars in the cross sections were estimated in the least-square fit procedures to be $\pm 2\%$ for σ_2^5 , $\pm 10\%$ for σ_3^5 , and $\pm 15\%$ for σ_4^5 . This behavior can be readily understood on the following facts: (i) the lower decay channels have larger cross sections; (ii) the corresponding photoelectrons have higher kinetic energies leading hence to a higher transmission through the TOF spectrometer. Both facts give rise to higher count rates and therefore to smaller error bars. The principal series $5, 3_{n'}$ is observed up to resonance $n' = 15$. The present relative measurements agree well with those of Menzel *et al.* with respect to lineshapes and energy positions of the resonances in all three decay channels. The previously in σ_3^5 and σ_4^5 unobserved resonances $5, 3_6$ and $5, 3_7$ are related to photoelectrons with relatively low kinetic energies, demonstrating the enhanced capability of the TOF analyzers used here in detecting photoelectrons with kinetic energies as low as 350 meV at sufficiently high count rates. In the $n = 2$ channel, the resonances $n' = 6, 7$, and 8 of the secondary series $5, 1_{n'}$ could be detected in the fit analysis with the present monochromator resolution of $\cong 6$ meV (FWHM).

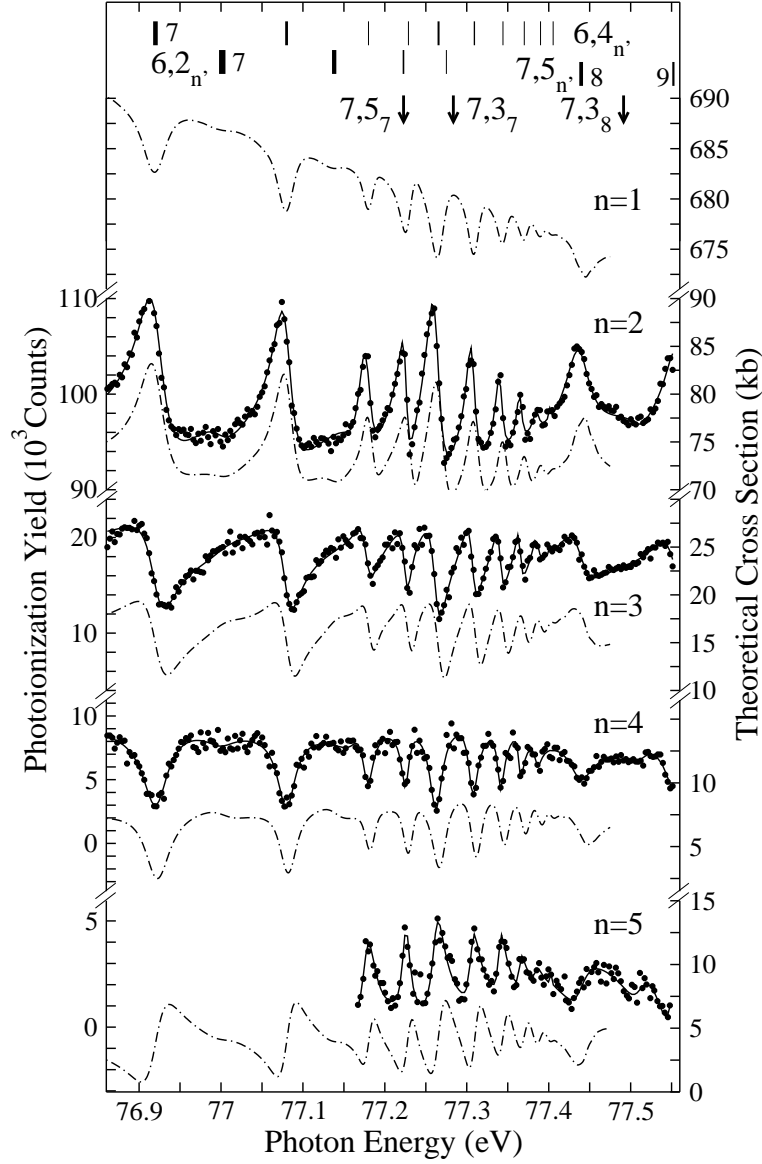


Figure 5.6: Experimental partial cross sections σ_n^6 leading to the final states $\text{He}^+(n)$, with $n = 2, 3, 4$, and 5 , respectively, in the energy region from 76.85 eV to 77.56 eV, along with the results of the eigenchannel R-matrix calculations; for details, see the caption of Fig. 5.5.

The PCSs below the ionization threshold I_6 , with the perturbers $7,5_8$ and $7,5_9$, and below the ionization threshold I_7 , with the perturber $8,6_{10}$, are shown in Figs. 5.6 and 5.7, respectively. The principal series $6,4_{n'}$ and $7,5_{n'}$ are observed up to the resonances $n' = 16$ and 19 , respectively. Note that the resonances $7,5_{10}$ and $7,5_{15}$ are almost completely suppressed due to interferences with the perturbers $8,6_8$ and $8,6_9$, respectively. These findings agree well with the results of earlier studies of the total photoionization cross sections [30]. The error bars in the PCS curves were estimated to be $\pm 1\%$ (σ_2^6), $\pm 1\%$ (σ_2^7), $\pm 3\%$ (σ_3^6), $\pm 2\%$ (σ_3^7), $\pm 6\%$ (σ_4^6), $\pm 5\%$ (σ_4^7), $\pm 11\%$ (σ_5^6), and $\pm 10\%$ (σ_5^7). Again, the resonances $6,2_7$, $6,2_8$, and $7,3_8$ of the secondary series are observed in the fit analysis of σ_2^6 and σ_4^7 , respectively. Due to small partial cross sections

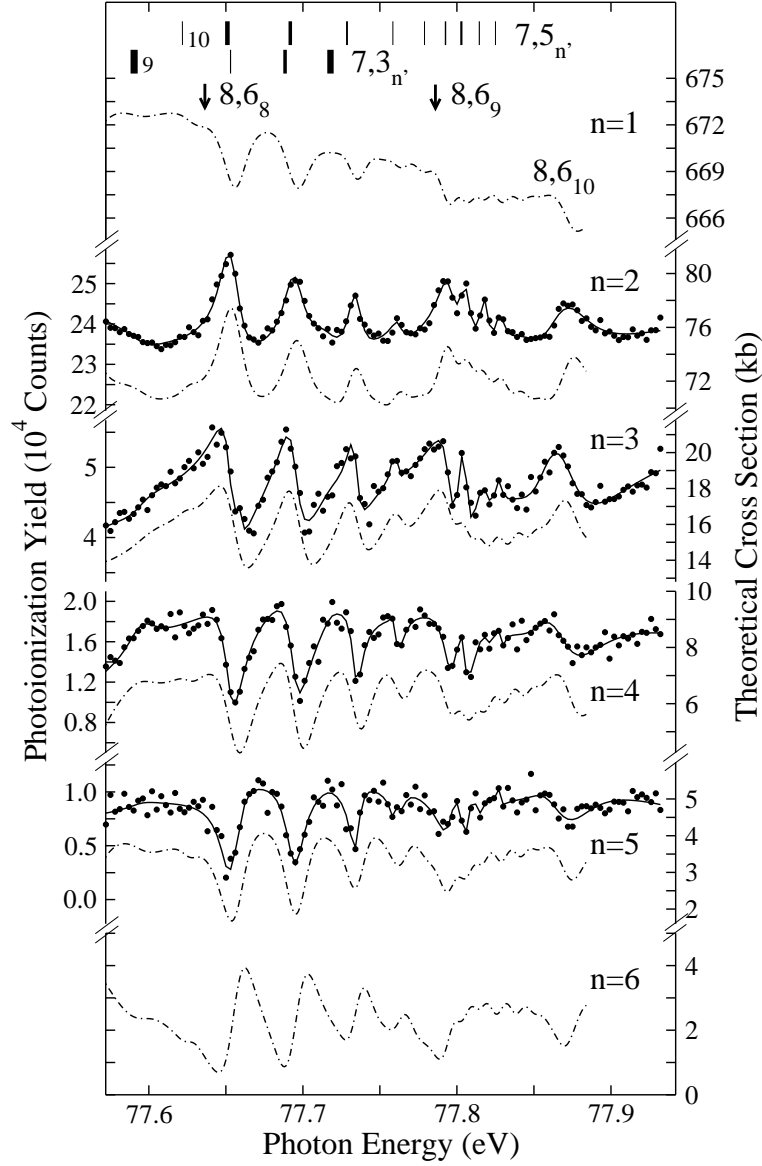


Figure 5.7: Experimental partial cross sections σ_n^7 leading to the final states $\text{He}^+(n)$, with $n = 2, 3, 4$, and 5 , respectively, in the energy region from 77.56 eV to 77.92 eV, along with the results of the eigenchannel R-matrix calculations. Note that the plotted theoretical results were shifted by 12 meV to lower energies; for details, see the caption of Fig. 5.5.

and relatively low transmission rate of the TOF spectrometer for slow electrons, the PCS σ_5^6 in the energy region below 77.155 eV (Fig. 5.6) and the PCS σ_6^7 (Fig. 5.7) could not be obtained from the present measurements.

Figures 5.8 and 5.9 display for the first time the experimental PCSs σ_n^8 and σ_n^9 (with $n = 2 - 6$). The energy positions of the perturbers $9, 7_9$, $9, 7_{10}$, $10, 8_{10}$, and $10, 8_{11}$ are also marked in the figures. In general, there is good agreement for the variations in the lineshape, the amplitudes, and the relative positions of the resonances between the experimental and theoretical spectra. Statistical error bars in the PCS curves were estimated to be $\leq \pm 1\%$ (σ_2^8 and σ_2^9), $\pm 1\%$ (σ_3^8 and σ_3^9), $\pm 3\%$ (σ_4^8), $\pm 2\%$ (σ_4^9), \pm

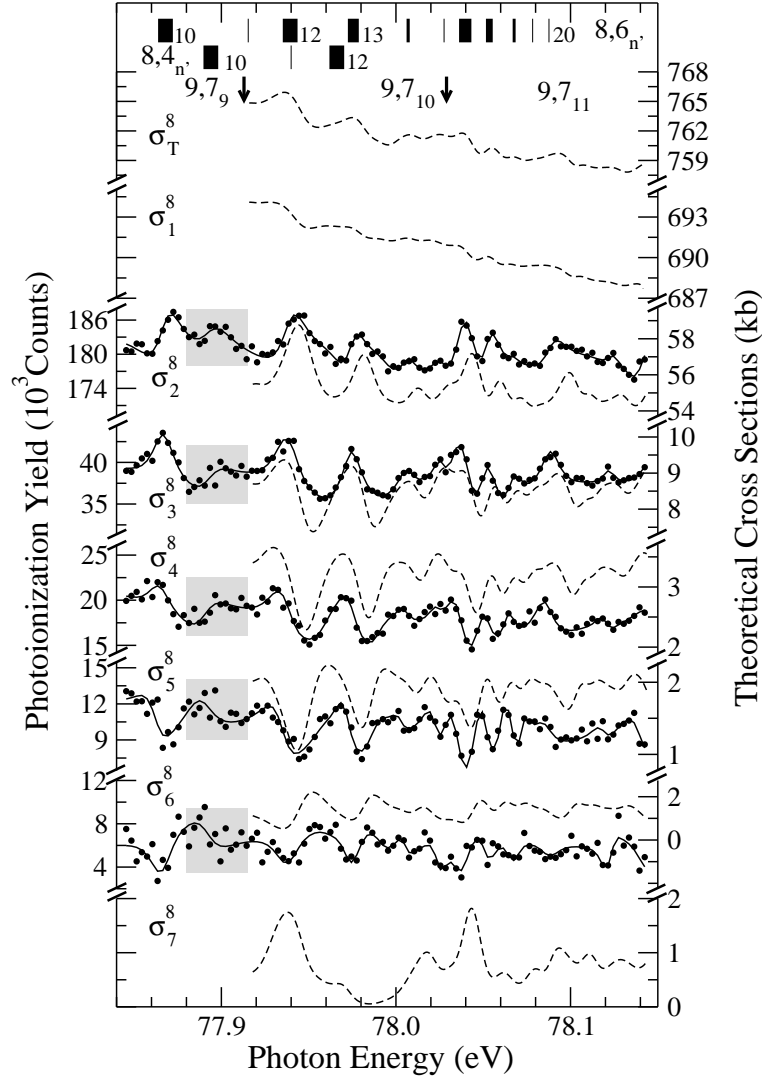


Figure 5.8: Experimental partial cross sections, σ_n^8 , leading to the final states $\text{He}^+(n)$, with $n = 2 - 6$, respectively, in the photon-energy region between 77.84 eV and 78.15 eV, along with the results of the eigenchannel R-matrix calculations. The energy position of the resonance $8,4_{10}$ of the secondary series is marked with grey bars. For details, see the caption of Fig. 5.5.

6% (σ_5^8), $\pm 4\%$ (σ_5^9), $\pm 11\%$ (σ_6^8), and $\pm 7\%$ (σ_6^9). Note that the possible systematic fluctuations caused by normalizing the spectra to σ_1 are not taken into account in these numbers. The increase of the error bar with higher excitation can also be understood by taking into account its lower cross section and correspondingly lower transmission through the TOF spectrometer, which is consistent with the results below the SIT I_7 . Due to small PCSs and the relatively low transmission rate of the TOF spectrometer for very slow electrons, the PCSs σ_7^8 , σ_7^9 , and σ_8^9 could again not be obtained from the present measurements.

Energy position and width of the resonance $8,4_{10}$ of the secondary series are marked by grey bars in figure 5.8, which is zoomed out together with the resonance $8,6_{10}$ in figure 5.10. The experimental total cross section [30] in the region was also plotted in

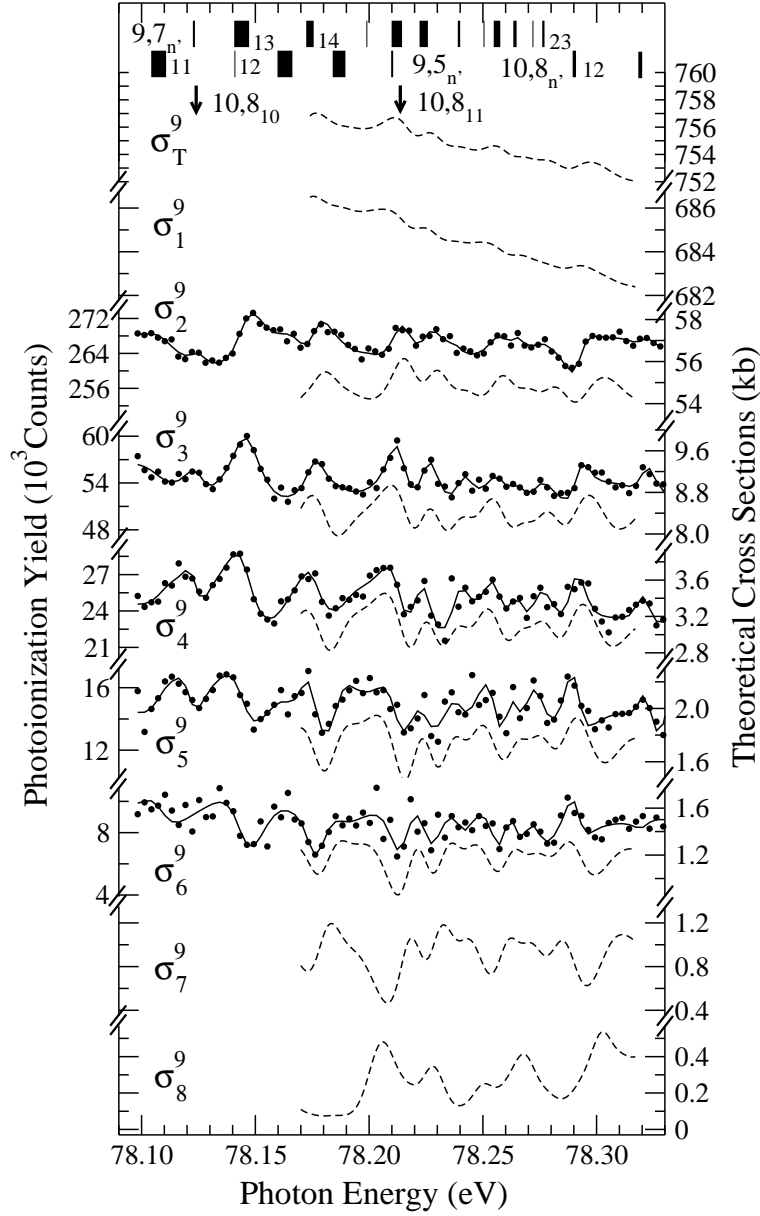


Figure 5.9: Experimental partial cross sections, σ_n^9 , leading to the final states $\text{He}^+(n)$, with $n = 2 - 6$, respectively, in the photon-energy region between 77.84 eV and 78.15 eV. For details, see the caption of Fig. 5.5.

this figure. Interestingly, although the TCS displays good statistics and high resolution, $\cong 4$ meV for TCS and $\cong 6$ meV for PCS, the resonance $8,4_{10}$ is observed clearly in all decay channels below the SIT I_8 in contrast to its absence in the TCS, which could be completely suppressed due to interferences with the perturbbers. This is due to the fact that the resonance $8,4_{10}$ shows quite different lineshapes in the partial cross sections which cancel out in the TCS. These different lineshapes are due to different coupling to various σ_n . In figure 5.10(f), the signal-to-noise ration is therefore very low, which traces of the resonance $8,4_{10}$ can only be identified by the fit curve. The present PCS measurements below the SITs I_7 and I_9 were published in Refs. [37] and [104].

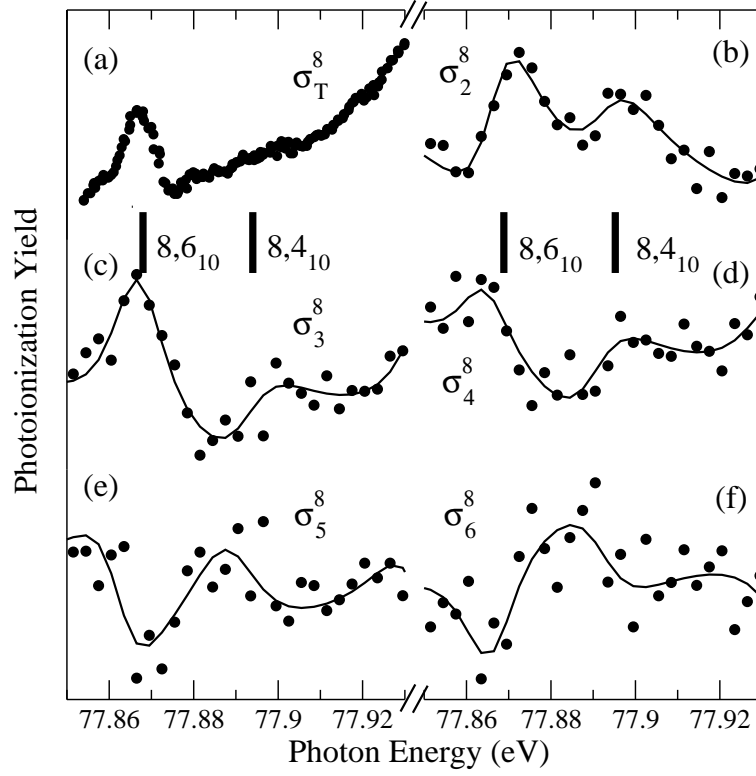


Figure 5.10: Experimental partial cross sections σ_n^8 for resonances $8,6_{10}$ and $8,4_{10}$ in the energy region from 77.85 eV to 77.93 eV. (a) for previous total cross section [30], (b) for σ_2^8 , (c) for σ_3^8 , (d) for σ_4^8 , (e) for σ_5^8 , and (f) for σ_6^8 . For details see figure 5.5.

5.3.2 General pattern

In 1995, Menzel *et al.* [35] found from their experimental PCSs for doubly excited helium below the SIT I_5 that the resonances below different ionization thresholds exhibit similar variations when $N - n$ is of the same value; this observation is called 'general pattern'. Later, these patterns in the PCSs were discussed theoretically up to the SIT I_9 by Schneider *et al.* [33] and van der Hart *et al.* [63]. With propensity rules that can be derived from the molecular adiabatic approximation introduced in Sect. 3.2.1, Schneider *et al.* [33] were able to understand these general patterns in the PCSs very well. In the present work, we shall confirm these general patterns experimentally and discuss them on the basis of the propensity rules.

As we discussed before in Sect. 3.2.1, the adiabatic avoided-crossing potential curves can be identified by the approximate quantum numbers $[n_\lambda n_\mu m]$ in a molecular picture. The mechanism of autoionization relies on the nonadiabatic transitions between these adiabatic avoided-crossing potential curves, in full analogy to electronic transition in molecules. *Radial* transition are sensitive to the change of the wave function as a function of R , i.e. via the change of n_μ . Therefore, these transitions occur preferentially through an avoided-crossing of two potential curves. The second kind of non-adiabatic transitions due to *rotational* coupling, the change of m between potential curves. Finally, there is no explicit mechanism to change n_λ . Hence, decays with $\Delta n_\lambda \neq 0$ are strongly suppressed.

In this way, three propensity rules for the autoionization process can be derived. The different propensity rules caused by different decay mechanisms are given in the order of the efficiency of the underlying decay mechanism [31, 33]:

$$\begin{array}{ll}
 (A) & \text{reduction of } [n_\mu/2] \\
 (B) & \text{change of } m \\
 (C) & \text{reduction of } n_\lambda.
 \end{array} \tag{5.1}$$

The propensity rules (A), (B), and (C) of Eq. (5.1) group the $^1P^o$ resonant states of helium into three classes I-III with typical widths separated by at least two orders of magnitude, $\Gamma_I : \Gamma_{II} : \Gamma_{III} \approx 10^4 : 10^2 : 1$. According to Eq. (3.19), the two classification schemes $[n_\lambda n_\mu m]_{n'}$ and $N, K_{n'}$ are equivalent. Therefore, the propensity rules (A) given in expression (5.1) can be transformed into “reduction of N ”. One can apply the approximate quantum numbers $N, K_{n'}$ to describe not only bound states but also continuum states. Thus for the principal Rydberg series $K = N - 2$, the decay from bound states N, K to continuum states n, k can occur via the propensity rule (A) by $\Delta N = N - n = \Delta K = K - k = 1, 2, \dots$. The differences in the efficiency of the decay mechanisms are so strong that a decay via rule (B) or (C) shows only visible influence on the spectra if the decay processes on the basis of the preceding propensity rule (A) are not possible [31, 33]. The coupling matrix elements, which lead to the propensity rules, are essentially very similar to the matrix elements that are relevant for the resonance parameters [106]. We can, therefore, conclude that resonances, which decay via the same propensity rule and have the same change in nodal structure, show similar lineshapes. In particular, most of the spectral features in doubly excited helium are governed by propensity rule (A). In this case, we expect similar lineshapes for the resonances in different PCSs if the decay leads to the same change in ΔN and ΔK , i.e. the changes of the nodal structure in the radial wave functions are identical. For example, propensity rule (A) results in the expectation that the principal series in the PCS σ_4^6 exhibits the same resonance profile as that in the PCS σ_3^5 . This expectation was confirmed by Menzel *et al.* [35] for resonances up to the ionization thresholds I_5 .

Fig. 5.11 presents examples of such cross section patterns, namely σ_2^4 , σ_3^5 , σ_4^6 , and σ_5^7 ; in these PCSs, the resonances of the principal series decay by $\Delta N = N - n = 2$. In order to demonstrate the ‘general patterns’, the photon energies were scaled to the effective quantum numbers μ_N by the Rydberg formula given in Eq. (4.2). The similarities of the cross section curves are evident except for the energy regions of perturber states indicated by vertical arrows. As mentioned above, the perturber states affect the resonance energies and linewidths of the various resonances and, as a consequence, the regularities fade out in the vicinity of perturber states, but further away, the ‘general pattern’ is restored. In the present measurements below the ionization threshold I_9 , similar general patterns were observed in σ_4^5 and σ_5^6 , with $\Delta N = 1$, in σ_2^5 , σ_3^6 , σ_4^7 and σ_5^8 with $\Delta N = 3$ in σ_2^6 , σ_3^7 , σ_4^8 , and σ_5^9 with $\Delta N = 4$, σ_2^7 , σ_3^8 , and σ_4^9 with $\Delta N = 5$, as well as σ_2^8 and σ_3^9 with $\Delta N = 6$. However, in the energy region of the higher ionization thresholds, such as in the SITs

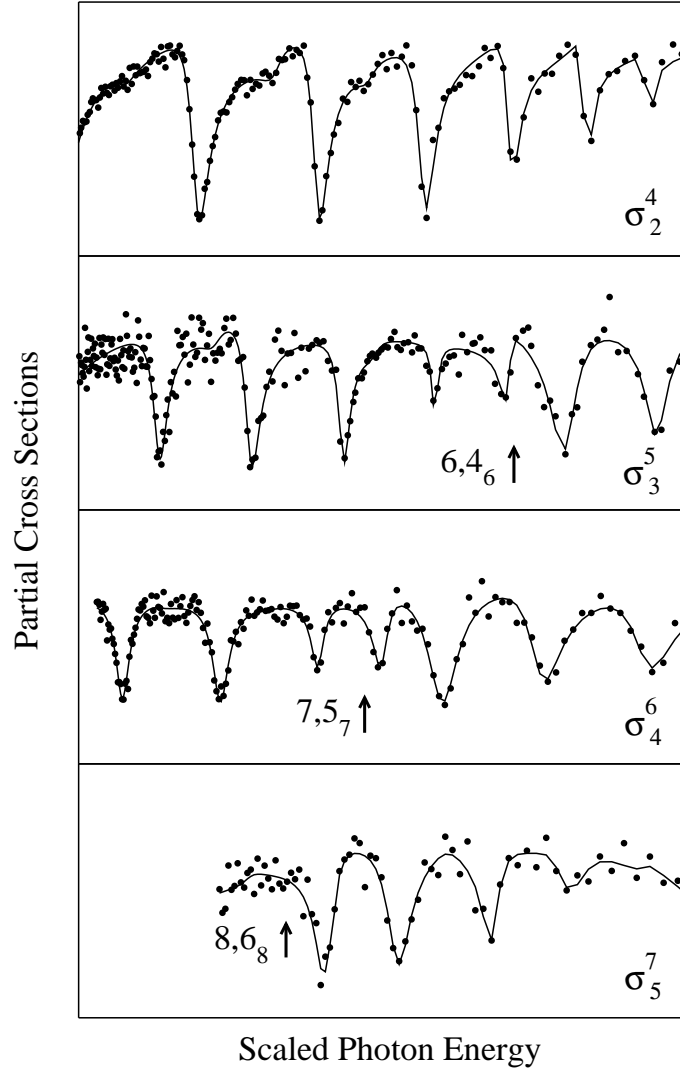


Figure 5.11: Partial photoionization cross sections σ_n^N as a function of scaled photon energy. For details see figure 5.5.

I_8 and I_9 , the general patterns become very weak due to the complex structures caused by interferences with two additional perturber states that interact with the principal Rydberg series.

5.3.3 Mirroring behavior

The TCS consists of a number of PCSs, which are defined by the quantum numbers of the outgoing electron and the remaining ion. After dividing the PCSs in any two groups P and Q , experimental and theoretical studies found that the variations in the vicinity of a resonance between the PCSs P and Q showed a similar variation [33, 36, 37, 38, 104]. This was called 'mirroring behavior' by Liu and Starace [36, 38], who first discussed it with an analytical expression for approximate conditions. Here, the energy axis is taken as the mirroring plane. These authors assume that this analytical expression can be used to understand mirroring behavior for any general case, not only in photoionization

process but also in photodetachment of negative ions [36, 38]. However, this explanation does not work for doubly excited helium.

If the TCS is regarded as the sum of two random groups of PCSs, denoted by P and Q , the PCS P can be expressed by Eq. (3.7), and for the PCS Q the same formula with P replaced by Q can be used. Note that the PCS P and the PCS Q can be individual PCSs or the sum of a number of individual PCS, which in the present case are the σ_n . By using Starace formula [59] which establishes relations between the parameters ρ and σ_T^0 in the Fano formula given in Eq. (3.6) for the TCS and the parameters σ_P^0 , σ_Q^0 , and α used in Eq. (3.7), namely,

$$\sigma_P^0 \langle |\alpha|^2 \rangle_P + \sigma_Q^0 \langle |\alpha|^2 \rangle_Q = \rho^2 \sigma_T^0, \quad (5.2)$$

$$\sigma_P^0 \text{Re} \langle \alpha \rangle_P + \sigma_Q^0 \text{Re} \langle \alpha \rangle_Q = \rho^2 \sigma_T^0, \quad (5.3)$$

$$\sigma_P^0 \text{Im} \langle \alpha \rangle_P - \sigma_Q^0 \text{Re} \langle \alpha \rangle_Q = 0, \quad (5.4)$$

Liu and Starace derived the PCS σ_Q [36]

$$\begin{aligned} \sigma_Q &= \sigma_Q^0 - \frac{\sigma_P^0}{1 + \epsilon^2} \{ 2\epsilon q \text{Re} \langle \alpha \rangle_P - 2q \text{Im} \langle \alpha \rangle_P + q^2 \langle |\alpha|^2 \rangle_P \} \\ &\quad + \frac{q^2 \rho^2 \sigma_T^0}{1 + \epsilon^2}, \end{aligned} \quad (5.5)$$

with the approximation $q\rho^2 \rightarrow 0$ when $\rho^2 \rightarrow 0$, but with $q^2\rho^2$ remaining finite. This has been shown by Nora Berrah and coworkers for two resonances of doubly excited Ar that are extremely weak in the TCS; in the PCSs, however, the resonances are clearly visible [107]. Although $\rho^2 \rightarrow 0$ is required for a mirroring behavior to occur, it has been observed in the theoretical photoionization cross section of Li^- even for ρ^2 as high as 0.3 [36]. In contrast to this, two sets of PCSs for helium in the double excitation region do not always mirror each other even for $\rho^2 \cong 0.001$ (see theoretical part in the dissertation), which can be understood well with a more general expression without any approximations

$$\begin{aligned} \sigma_Q &= \frac{\sigma_Q^0}{1 + \epsilon^2} \{ \epsilon^2 + 2\epsilon(q \text{Re} \langle \alpha \rangle_Q - \text{Im} \langle \alpha \rangle_Q) \\ &\quad + (1 - 2q \text{Im} \langle \alpha \rangle_Q - 2\text{Re} \langle \alpha \rangle_Q + (q^2 + 1) \langle |\alpha|^2 \rangle_Q) \} \\ &= \sigma_Q^0 + \frac{\sigma_Q^0}{1 + \epsilon^2} \{ 2\epsilon(q \text{Re} \langle \alpha \rangle_Q - \text{Im} \langle \alpha \rangle_Q) \\ &\quad + (-2q \text{Im} \langle \alpha \rangle_Q - 2\text{Re} \langle \alpha \rangle_Q + (q^2 + 1) \langle |\alpha|^2 \rangle_Q) \} \\ &= \sigma_Q^0 + \frac{\sigma_P^0}{1 + \epsilon^2} \{ 2\epsilon(-q \text{Re} \langle \alpha \rangle_P + \text{Im} \langle \alpha \rangle_P + q\rho^2 \sigma_T^0 / \sigma_P^0) + (2q \text{Im} \langle \alpha \rangle_P \\ &\quad + 2\text{Re} \langle \alpha \rangle_P - 2\rho^2 \sigma_T^0 / \sigma_P^0 - (q^2 + 1) \langle |\alpha|^2 \rangle_P) + (q^2 + 1) \rho^2 \sigma_T^0 / \sigma_P^0 \} \\ &= \sigma_Q^0 - \frac{\sigma_P^0}{1 + \epsilon^2} \{ 2\epsilon(q \text{Re} \langle \alpha \rangle_P - \text{Im} \langle \alpha \rangle_P) \\ &\quad - 2q \text{Im} \langle \alpha \rangle_P - 2\text{Re} \langle \alpha \rangle_P + (q^2 + 1) \langle |\alpha|^2 \rangle_P \} \\ &\quad + \frac{2q\rho^2 \sigma_T^0}{1 + \epsilon^2} \epsilon + \frac{q^2 \rho^2 \sigma_T^0}{1 + \epsilon^2} - \frac{\rho^2 \sigma_T^0}{1 + \epsilon^2}. \end{aligned} \quad (5.6)$$

Comparing Eq. (3.7) with Eqs. (5.5) and (5.6), one can realize that the second term plays a key role for the mirroring on the lineshape of the resonance between σ_P and σ_Q . The last three terms described the Fano-like variation of the resonances in the TCS determine whether the resonances in the PCS P and PCS Q exhibit a mirroring behavior. The resonances in the two groups P and Q of the PCSs mirror each other if the second term of Eq. (5.6) is dominant as compared to the last three terms. If $|q| \gg 1$ and $\rho^2 \rightarrow 0$, the third and fifth terms in Eq. (5.6) can be neglected in comparison with the fourth term. In this case, Eq. (5.6) results in Eq. (5.5) if one omits, in addition to the third and fifth term, all contributions of the second term that do not include q or q^2 . As discussed in Ref. [36], in this case the resonances display a Lorentzian profile in the TCS.

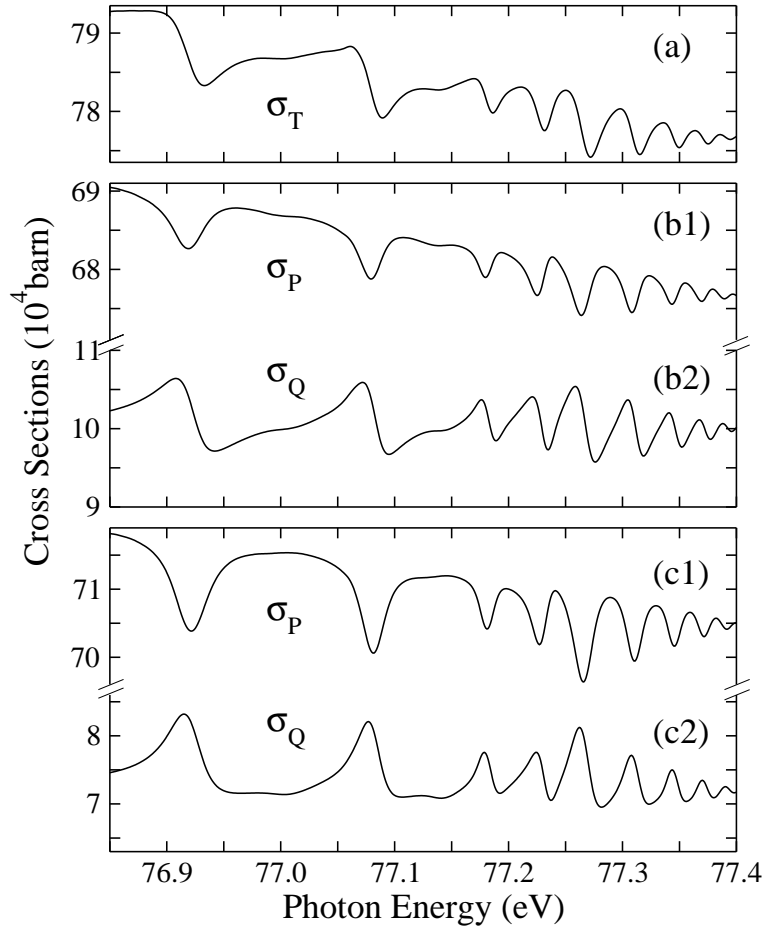


Figure 5.12: Cross sections below the ionization threshold I_6 obtained from eigenchannel R-matrix calculations [33] and convoluted with a Gaussian resolution function of 6 meV width (FWHM). (a) Total cross section σ_T . In (b) and (c) the PCS σ_P and σ_Q were established in different ways: (b1) $\sigma_P = \sigma_1$ and (b2) $\sigma_Q = \sigma_2 + \sigma_3 + \sigma_4 + \sigma_5$; (c1) $\sigma_P = \sigma_1 + \sigma_3 + \sigma_4 + \sigma_5$ and (c2) $\sigma_Q = \sigma_2$.

In the region between the SITs I_5 and I_7 of He^+ , the Fano parameter ρ^2 is of the order of 0.01 for the principal series (see Fig. 5.12 (a) for the theoretical TCS below I_6 [33]). In the other tablets of Figs. 5.12, we plot two examples, with the TCS $\sigma_T = \sigma_P + \sigma_Q$ being

separated into two groups. In the first example $\sigma_P = \sigma_1$ and $\sigma_Q = \sigma_2 + \sigma_3 + \sigma_4 + \sigma_5$ (b1, b2); in the second example, $\sigma_P = \sigma_2$ and $\sigma_Q = \sigma_1 + \sigma_3 + \sigma_4 + \sigma_5$ (c1, c2). In the second example, the PCS σ_P mirrors the PCS σ_Q very well [Figs. 5.12 (c1) and (c2)]. In contrast to this, the mirroring behavior is not well expressed in the first example [Fig. 5.12 (b1) and (b2)]. This can be understood as follows: A mirroring behavior is expected if the amplitudes of the resonances in the TCS are small compared to variations in the PCS, i.e. if terms three to five in Eq. (5.6) are small compared to term two. In helium, however, each single PCS σ_n exhibits amplitudes that are of the same order of magnitude as in σ_T . Since this holds for all ionization thresholds I_N up to $N = 9$ (see Fig. 3 in Ref. [33]), no general mirroring behavior will be expected in the double-excitation region of helium. Mirroring behavior occurs only accidentally, namely if the PCS σ_P already mirrors σ_T [see Fig. 6 (a) and (c1)]. In this cases, the second term in Eq. (5.6) mimics σ_T and a mirroring behavior is observed. Even in cases where σ_P is established by a number of σ_n , no general mirroring behavior is expected since the amplitude of the variation in σ_P will still not be large as compared to the variation in σ_T . In summary, for the existence of a general mirroring behavior the condition $\rho^2 \rightarrow 0$ is not sufficient. In addition to this it is also necessary that the amplitudes of resonances in the PCS are considerably larger than those in the TCS. However, as observed in the theoretical cross sections up to ionization threshold I_9 [33], the amplitudes in the PCS decrease by the same amount with increasing N as the amplitudes in the TCS. As a consequence, we do not expect a general mirroring behavior in helium below higher- N ionization thresholds I_N with ρ^2 even much smaller than 0.01. This conclusion will be further confirmed by the studies of the secondary and third Rydberg series below the SITs I_4 in the theoretical part of this dissertation.

Since the sum of any two PCSs can be expressed mathematically by the Fano formula, the analysis given above can also be employed to discuss and understand the mirroring behavior of any two individual PCSs although the sum of these will not be the TCS, such as in case of σ_2^6 and σ_4^6 as well as σ_3^6 and σ_5^6 (see Fig. 5.6). In these cases, the resonances in $\sigma_S = \sigma_2^6 + \sigma_4^6$ and $\sigma_S = \sigma_3^6 + \sigma_5^6$ are almost canceled out, and the σ_S are expected to be quite structureless. On the other hand, if any σ_S shows considerable structure, the contributing individual partial cross sections do not show mirroring behavior. In addition, the perturbers have no effect on the mirroring behavior between the PCS P and PCS Q . In addition, it should be noted that below the SITs I_5 to I_7 , the PCS σ_2^N mirrors the PCS σ_4^N and the PCS σ_3^N mirrors the PCS σ_5^N (not for $N = 5$). This behavior might be due to a relation between the propensity rules and the mirroring behavior and can be an interesting topic for future studies.

5.4 Angle-resolved measurements up to I_7

The ADP, β_n , and the PCS, σ_n , show different dependences on the dipole matrix element for excitation and the Coulomb matrix element for decay as well as on the phase shifts of various outgoing channels. Therefore, resonances can be clearly seen in the ADP, β_n , but

not in the PCS, σ_n , or vice versa. Consequently, the ADP can be used for an additional check on theoretical models, and one expects that additional resonances are resolved from the ADP. From the point of view of complete measurements, the ADP measurements are also necessary for a complete check on quantum mechanics.

5.4.1 Differential cross sections and β parameter

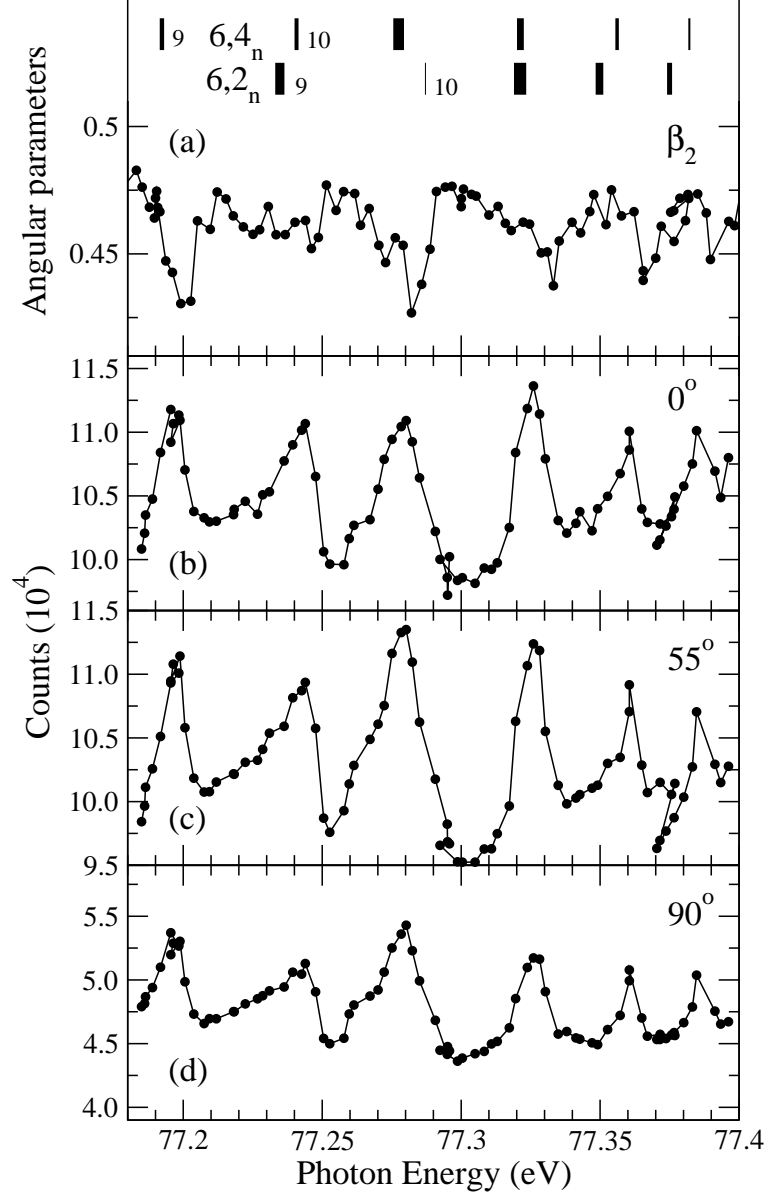


Figure 5.13: Differential cross sections, $d\sigma_2/d\Omega$, measured at angles (b) 0° , (c) 55° , and (d) 90° below the SIT I_6 and (a) corresponding angular distribution parameter β_2^6 . Solid points represent the present experimental results and solid lines through the data points serve as the guides to the eye. The two vertical-bar diagrams in the upper part of the figure give the assignments of the double-excitation resonances specified by n' , with the widths of bars being proportional to the linewidths of the corresponding resonances [31].

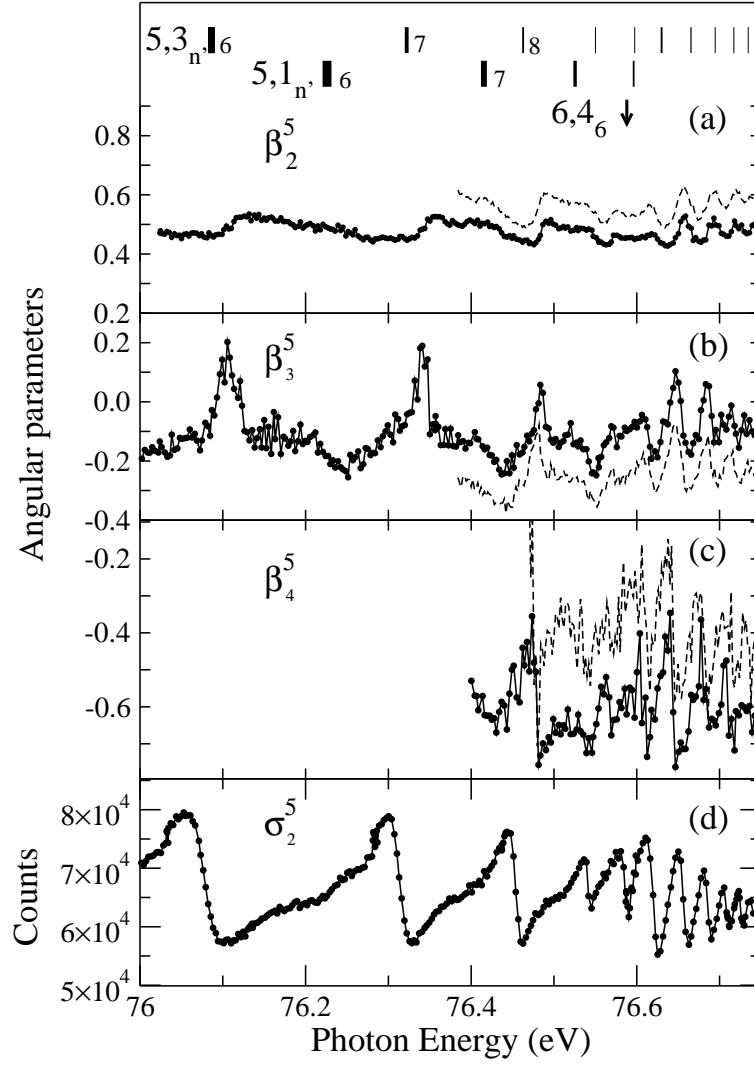


Figure 5.14: Angular distribution parameters β_n^5 with (a) $n = 2$, (b) $n = 3$, and (c) $n = 4$, respectively, together with (d) the PCS σ_2^5 below the SIT I_5 ; the measurements of Menzel *et al.* were displayed by dash lines. For details see Fig. 5.13.

As an example, the differential cross sections (DCS) $d\sigma_2/d\Omega$, measured at angles 0° , 55° , and 90° below the SIT I_6 are presented in Fig. 5.13(b), (c), and (d) together with the corresponding ADP β_2^6 in Fig. 5.13(a). The solid points represent the measurements and the solid lines are a guide to the eyes. In general, the resonances cause quite similar variations in the DCS, i.e. only slight differences were found in Fig. 5.13(b)-(d). Note that the same scale was used on the ordinate in this figure. The $d\sigma_2/d\Omega$ taken at 55° exhibits the strongest variations caused by the resonance, but the direct ionization cross section which causes the constant background is almost identical to that at 0° . The direct ionization cross section at 90° is by a factor 2 smaller than those at the other two angles. This is due to the positive mean value of the ADP $\beta_2^6 = 0.47$; its angular distribution of intensity is shown in Fig. 1.1. Indeed, the variations caused by the resonances and its absolute value of β are quite sensitive to those in the DCSs, $d\sigma_2/d\Omega$. The resonance structures seem quite pronounced in $d\sigma_2/d\Omega$, but sometimes they can lead to quite weak

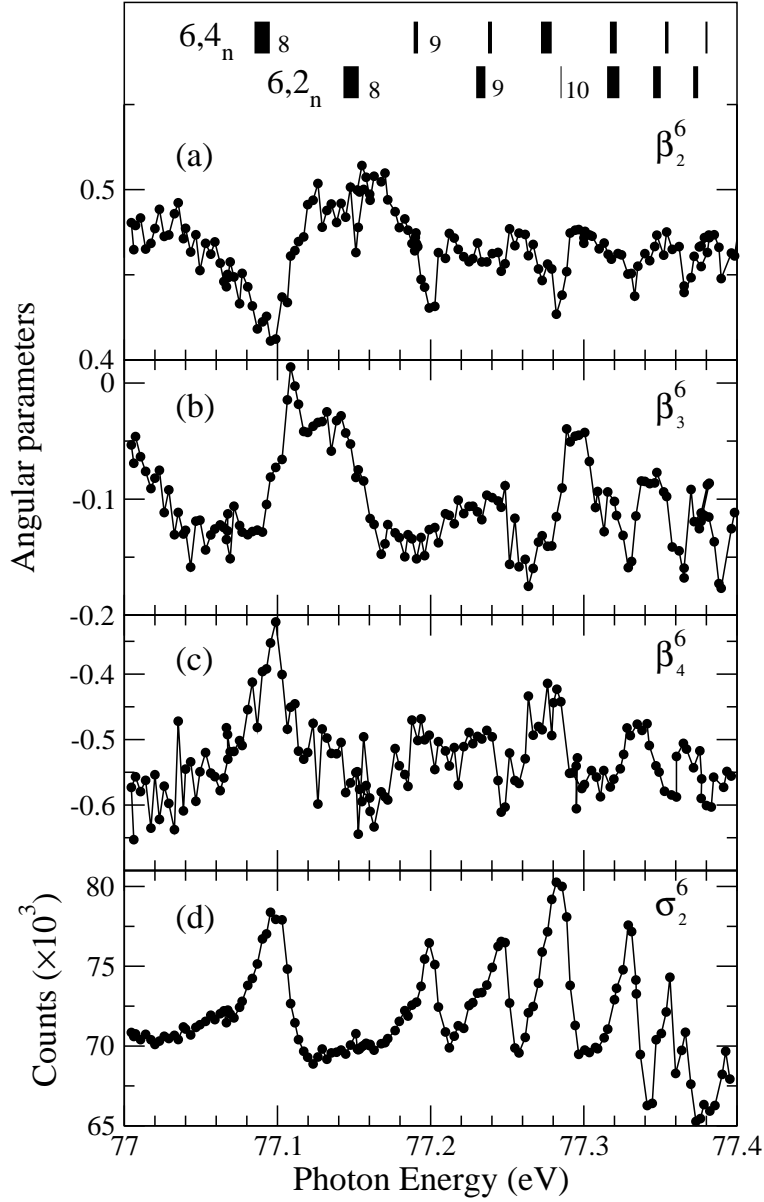


Figure 5.15: Angular distribution parameters β_n^6 with (a) $n = 2$, (b) $n = 3$, and (c) $n = 4$, respectively, together with (d) the PCS σ_2^5 below the SIT I_6 ; for details see Fig. 5.13.

variations in β . This is also the reason why more TOF spectrometers are needed in the experiments to improve the precision of the measurement.

The results of preliminary measurements of the β parameters below the SITs I_5 to I_7 are presented given in Figs. 5.14, 5.15, and 5.16. For a better identification of the resonances, the present PCSs σ_2^N are also plotted in these figures. Our measurements below the SIT I_5 agree well with the experimental results of Menzel *et al.* [35]. The first two members $5, 3_6$ and $5, 3_7$ of the principal series below the SIT I_5 were observed in the β_2^5 and β_3^5 curves for the first time. These resonances could not be observed in β_4^5 due to the low cross section in combination with a low transmission rate for this slow electrons. Systematic errors could result in large fluctuations of the absolute values of

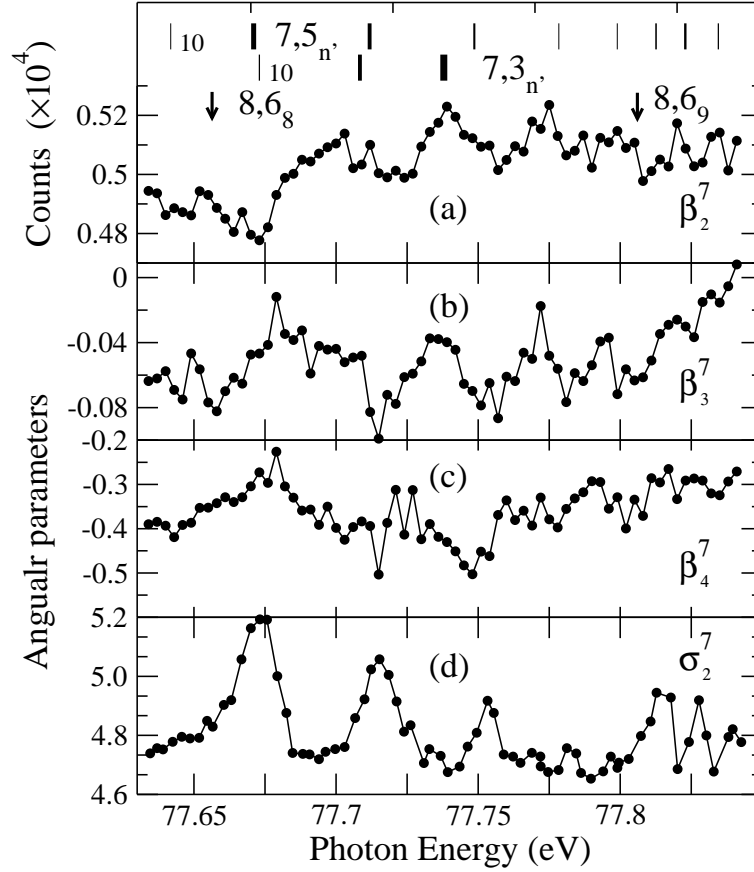


Figure 5.16: Angular distribution parameters β_n^7 with (a) $n = 2$, (b) $n = 3$, and (c) $n = 4$, respectively, together with (d) the PCS σ_2^7 below the SIT I_7 ; for details see Fig. 5.13.

β as mentioned before. The error bars for the absolute value of β can easily reach more than 50% if only two TOFs are employed. For the results presented in Figs. 5.14, 5.15, and 5.16, three or four TOFs were employed, and the error bars on absolute value of β are estimated to be less than 15%. Considering these error bars, the present absolute values of β^5 are in agreement with previous measurements and calculations published in Ref. [35].

For β^6 and β^7 , presented in Figs. 5.15 and 5.16, neither experimental nor theoretical results are available in the literature for comparison. Interestingly, the variations of the resonance $6, 2_8$ are clearly observed in β_2^6 and β_3^6 for the first time. In contrast to the variations in β , resonance $6, 2_8$ is strongly suppressed in σ_2 as shown in Fig. 5.15(d), as well as in the experimental and theoretical PCSs σ_n presented in Fig. 5.6. This can be understood by the different dependences of β and σ on the matrix elements for excitation and decay of the autoionization states as well as on the phase shifts of the various outgoing channels.

In order to improve the signal-to-noise ratio, the regions below the SITs I_6 to I_7 was again studied in our with 12 TOFs mounted at various angles in the dipole plane. These data are expected to have better statistics and higher transmission rate. However, they are not fully analyzed so far and, therefore, cannot be presented in this dissertation.

Part III

Theoretical work on photoionization with excitation in helium

Chapter 6

Theoretical calculation of n – and l –specific partial cross sections

The fact that direct photoionization and the autoionization of the highly correlated doubly-excited states can interfere renders these process a challenge for theory. This is particularly valid for the evaluation of l -specific partial cross sections (PCS), σ_{nl} , and angular distribution parameters (ADP), β_{nl} , which are much more sensitive to small deficiencies in the used wave functions than the total cross section (TCS). In addition, some Rydberg series that are weak in the TCS and n -specific PCSs can be much more intense in the l -specific PCSs and ADPs; this fact can be very helpful in resolving resonance patterns such as the mirroring behavior discussed in Sect. 5.3.3. These facts have caused substantial interest in l -specific PCSs and ADPs both from a theoretical and an experimental point of view. Very recently, Harries *et al.* reported on the first analysis of l -specific PCSs below the $N = 4$ ionization threshold using a lifetime-resolved fluorescence technique [39, 40]. These measurements of l -specific PCSs allow a critical test of the theoretical approach, the results of which can be employed to further discuss the mirroring behavior and the mimicking behavior. In addition, reliable l -specific ADPs are expected to represent a guidance for future experiments, in regions where measurements still are not available.

In section 5.3.3, the mirroring behavior in the PCSs first developed by Liu and Starace [36] was already discussed. We did not find a general mirroring behavior in the PCSs of doubly excited helium, and extended the analytical expression given by Liu and Starace to a more general case in order to understand this finding. We realize that $\rho^2 \rightarrow 0$ is not a sufficient condition for mirroring behavior. It is additionally necessary that the variations in the PCS are considerably larger than those in the TCS. In the principal series of helium, the variations of the PCSs and those of the TCS are of comparable magnitude, i.e. the observation of a mirroring behavior in some special cases is only accidental, e.g. if one PCS mimics the TCS (see Sect. 5.3). In the following theoretical work, we shall examine the second and third Rydberg series, which that possess ρ^2 -values that are much smaller than these of the principal series. In this way, we are able to further confirm our predictions given in Sect. 5.3.3.

In the following we will discuss shortly the mimicking behavior, which is the opposite of the mirroring behavior and can be found for the case of $\rho^2 \rightarrow 1$. If $\rho^2 \rightarrow 1$, C_1 and C_2 in Eq. 3.8 are equal to q and q^2 , respectively [38, 59]. Then, with Eq. (3.8), the two groups of resonances in the PCSs, σ_P and σ_Q , can be written as

$$\frac{\sigma_P}{\sigma_P^0} = \frac{\sigma_Q}{\sigma_Q^0} = \frac{(q + \epsilon)^2}{1 + \epsilon^2}. \quad (6.1)$$

Obviously, the resonances in the two PCSs, σ_P and σ_Q , mimic each other, and according to this the observation was called mimicking behavior by Liu and Starace [38]. Such a mimicking behavior in the n and l -specific ADPs of the principal series can be understood on the basis of that of the l -specific PCSs. Besides this, one can understand on the basis of such mimicking behavior and an analytical expression of the ADPs, why some resonances cause only rather small variations in the l -specific ADP in some cases, while – on the other hand – they exhibit pronounced variations in the respective l -specific PCS. A study of mirroring as well as mimicking behavior can improve the understanding of correlation and decay dynamics in two-electron atoms.

In this chapter, we report on R-matrix calculations of the PCSs, σ_{nl} , and ADPs, β_{nl} , below the single ionization threshold I_3 and I_4 for the photoionization process described with Eq. (3.2). The calculations were performed in LS coupling, although recent experimental and theoretical studies have shown that spin-orbit interaction has an important influence on the photoionization spectrum very close to the SIT I_2 [42]. However, experimental PCSs and ADPs are not available close to threshold, and the present calculations were restricted to the energy region where the LS-coupling scheme is a good approximation.

6.1 R-matrix method

The R-matrix method, which is based on the theory developed by Burke *et al.* [108], has become a quite powerful tool to calculate the interaction of electrons and photons with isolated atoms and their ions. R-Matrix theory [108] starts by partitioning the configuration space into two regions by a sphere of radius a centered on the target nucleus. In the internal region $r \leq a$, electron exchange and correlation between the scattered electron and the N -electron target are taken into account. The $(N + 1)$ -electron wave function

$$\Psi_E = \sum_k B_{Ek} \Psi_k \quad (6.2)$$

in the internal region is expanded in terms of energy-independent basis Ψ_k ,

$$\begin{aligned} \Psi_k = & \mathcal{A} \sum_{ij} c_{ijk} \bar{\phi}_i(x_1, \dots, x_N; \hat{r}_{N+1} \sigma_{N+1}) \frac{1}{r_{N+1}} u_{ij}(r_{N+1}) \\ & + \sum_j d_{jk} \chi_j(x_1, \dots, x_{N+1}), \end{aligned} \quad (6.3)$$

where \mathcal{A} is the antisymmetrization operator which accounts for electron exchange between the target electrons and the free electron. Note that the energy dependence is described by the coefficients B_{Ek} . $\bar{\phi}_i$ are channel functions of the target terms that are included in the close-coupling (CC) expansion and are coupled to the angular and spin functions of the scattered electron. The χ_j in the second sum, which vanish at the surface of the internal region, are formed from the bound orbitals of the $(N + 1)$ system and are included to ensure completeness of the total wave function. The c_{ijk} and d_{jk} coefficients in Eq. (6.3) are determined by diagonalizing the $(N + 1)$ -electron Hamiltonian.

The continuum orbitals u_{ij} in Eq. (6.3) for each angular momentum l_i are normally obtained by solving the model single-channel scattering problem

$$\left(\frac{d^2}{dr^2} - \frac{l_i(l_i + 1)}{r^2} + V_0(r) + k_{ij}^2 \right) u_{ij}(r) = \sum_n \Lambda_{ijn} P_{nl_i}(r) \quad (6.4)$$

subject to the fixed boundary conditions

$$u_{ij}(0) = 0 \quad (6.5)$$

$$\left(\frac{a}{u_{ij}(a)} \right) \left(\frac{du_{ij}}{dr} \right)_{r=a} = b. \quad (6.6)$$

The Lagrange multipliers Λ_{ijn} ensure that the continuum orbitals are orthogonal to the bound orbitals $P_{nl_i}(r)$ of the same angular symmetry. $V_0(r)$ is a zero-order potential chosen to be the static potential of the target. k_{ij}^2 and a are the eigenvalues and the radius of the sphere defining the internal region, respectively. The constant b is arbitrary, and normally set to zero.

The orbital functions $P_{nl}(r)$ are expressed in slater-type analytical form

$$P_{nl}(r) = \sum_{jnl} C_{jnl} r^{P_{jnl}} \exp(-\xi_{jnl} r) \quad (6.7)$$

and they satisfy the orthonormality conditions:

$$\int_0^\infty P_{nl}(r) P_{n'l'}(r) dr = \delta_{nn'}. \quad (6.8)$$

C_{jnl} , ξ_{jnl} and P_{jnl} are the Clementi-Roetti parameters [109]. In the external region, the colliding electron is outside the atom and a set of coupled differential equations, satisfied by the reduced radial wave functions, are solved subject to the boundary conditions as $r \rightarrow \infty$. The two regions are linked by the R-matrix on the boundary ($r = a$) [108].

The R-Matrix method uses the same target orbitals to deal with the initial and final $(N + 1)$ -electron in the photoionization calculations. The choice of these orbitals for the $(N + 1)$ -electron system in the first sum of Eq. (6.3) as well as a configuration-interaction expansion for each target state is very crucial. In this dissertation, the CC expansion of the He^+ target is represented by 20 states obtained from the configurations nl , $n = 1, 2, 3, 4, 5$ and $l = s, p, d, f, g$ as well as $\bar{6}s$, $\bar{6}p$, $\bar{6}d$, $\bar{6}f$, $\bar{6}g$, $\bar{6}h$. The $1s - 5g$ are exact hydrogen-like wave functions of He^+ that limit the present calculation below the SIT I_4 . The $\bar{6}l$ are polarized correlation orbitals of He^+ and represent electron correlation

Table 6.1: Radial function parameters for He^+ targets.

orbitals (nl)	C_{jnl}	P_{jnl}	ξ_{jnl}
$1s - 5g$	hydrogen-like orbitals		
$\bar{6}s$	3.72615	1	0.99478
	-12.31193	2	1.01114
	15.65776	3	0.99832
	-7.40524	4	0.99084
	0.68349	5	0.48055
	-0.37439	6	0.37308
$\bar{6}p$	1.57314	2	2.22668
	-1.28440	3	1.69799
	1.60044	4	0.50277
	-2.42762	5	0.47997
	1.06946	6	0.45202
$\bar{6}d$	1.00608	3	3.69850
	-0.14955	4	1.02029
	0.21028	5	0.42455
	-0.17955	6	0.41004
$\bar{6}f$	0.99998	4	4.78402
	-0.01674	5	0.57790
	0.01191	6	0.44364
$\bar{6}g$	1.00000	5	5.95148
	-0.00036	6	0.43459

optimized on the ground state using the CIVPOL code [110]. The optimized parameters are shown in Table 6.1.

The polarized orbitals included in the target states provide a faster convergence of the wave function in Eq. (6.3) and a better value for the ground state energy. Their effects on photoionization cross sections and resonance properties for the doubly excited states $^1P^o$ of helium have been discussed in detail in Ref. [111]. In the present case they improve the agreement between the results in length and velocity forms. A crucial choice of the target terms is provided by a calculation of the ground state. The ground state has an energy of $E = -4 + I_1$ in Rydberg obtained from the variational principle. Table 6.2 lists ionization energies I_1 calculated by the use of different sets of target functions in Refs. [111, 112, 113, 114]. Our calculations lead to an energy of -1.80243 Ry for I_1 , which can be compared with the non-relativistic limit (Pekeris's result) of -1.8074 Ry

[112]; the present calculations give obviously better results than other calculations using different target terms.

Table 6.2: Results for the energy of the SIT I_1 of Helium.

States included in expansion	$I_1[\text{Ry}]$	Refs.
1s	-1.7450	Ref. [113]
1s, $\bar{2}p$, $\bar{3}d$	-1.7817	[113]
1s, 2s, $\bar{2}p$, 2p, $\bar{3}d$	-1.8007	[113]
1s, 2s, 2p, $\bar{3}p$, $\bar{3}d$	-1.7868	[114]
1s, 2s, 2p, 3s, 3p, 3d	-1.7732	[111]
1s, 2s, 2p, ..., 4f	-1.7741	[111]
1s, 2s, 2p, ..., 5g	-1.7742	[111]
1s, 2s, 2p, 3s, 3p, 3d, $\bar{4}s$, $\bar{4}p$, $\bar{4}d$	-1.7908	[111]
1s, 2s, 2p, ..., 5g, $\bar{6}s$, ..., $\bar{6}h$,	-1.8024	present work
Pekeris's result	-1.8074	[112]

Table 6.3: Results of the present calculations for the effective quantum numbers of the singly excited states $1sns$ ($^1S^e$) and $1snp$ ($^1P^o$) of helium. Comparison with experimental results of Moore [115], and the results of calculations based on the R-matrix method by Fernley et al. [114].

n	$1sns$ ($^1S^e$)			$1snp$ ($^1P^o$)		
	theor. results		exp.	theor. results		exp.
	present	Ref. [114]	exp. [115]	present	Ref. [114]	exp. [115]
1	0.74485	0.7481	0.7439			
2	1.85205	1.8579	1.8509	2.01016	2.0101	2.0095
3	2.85799	2.8637	2.8568	3.01203	3.0120	3.0113
4	3.85972	3.8657	3.8585	4.01254	4.0125	4.0118
5	4.86051		4.8593	5.01276		5.0120
6	5.86090		5.8596	6.01287		6.0121
7	6.86115		6.8598	7.01294		7.0121
8	7.86131		7.8602	8.01299		8.0117
9	8.86142		8.8595	9.01302		9.0117
10	9.86149		9.8596			

Tab. 6.3 provides the present effective quantum numbers for the $1sns$ ($^1S^e$) and $1snp$ ($^1P^o$) of Rydberg series along with the R-Matrix calculations of Fernley *et al.* [114] and

experimental values of Moore [115], which reveals a good agreement. Further confirmation on the convergence of the CI expansion is provided by the agreement of the length and velocity forms of the present results; this will be discussed in more detail on the basis of the data in the following section. The present configurations and optimized parameters were employed in the calculations of the DCSs below I_5 [116]. In this dissertation, the calculations will be extended to n - and l -specific PCSs and ADPs.

6.2 Photoionization spectra below I_3

The l -specific PCSs, as compared to the n -specific PCSs, are much more sensitive to the transition matrix elements, a fact that can be used to further explore the mirroring behavior in l -specific PCSs. In this section, the mimicking behavior in the ADPs is explained for the first time on the basis of the same behavior in the PCSs.

6.2.1 Partial cross sections σ_{nl}

Below the SIT I_3 of He^+ , the channels $n = 1$ and 2 are open resulting in $\text{He}^+(n = 1)$ and $\text{He}^+(n = 2)$ final states. In Fig. 6.1, we show the results of the present calculations for the PCSs to these channels and for the total photoionization cross section. The good agreement of the PCSs obtained in the length (solid line) and velocity gauge (dashed line) is due to the high quality of the chosen target wave function. In the discussed energy region, the spectrum includes five resonance series that—in the independent-electron limit—are linear combinations of the configurations $3sn'p$, $3pn's$, $3pn'd$, $3dn'p$, $3dn'f$. σ_1 consists of $\cong 90\%$ background cross section due to the strong direct ionization, which decreases strongly with increasing photon energy. The different variations in σ_1 and σ_2 caused by the principal series $3, 1_{n'}$ can be regarded as a consequence of different changes of the nodal structure of the wave function in the decay process according to the so-called propensity rules [33, 31], which were discussed in more details in Sect. 5.3.2.

The resonances $3, -1_3$ and $3, 2_4$, which is plotted in magnified form in the inset, are good examples for testing our predictions for mirroring behavior. Although ρ^2 is very small, namely 0.016 for $3, -1_3$ and 0.001 for $3, 2_4$, the two resonances do not show mirroring behavior between σ_1 and σ_2 , in contrast to the prediction of Liu and Starace [36]. Moreover, $3, -1_3$ shows mimicking behavior. As described above, the absence of mirroring behavior can be understood on the basis of the analytical expression derived in Sect. 5.3.3 as well as by the fact that the variations in the TCS caused by these two resonances are of the same order of magnitude as those of σ_1 . Compared to previous calculations, the present results—shown in Fig. 6.1—are in good agreement with the K-matrix L^2 -basis-set calculations of Moccia and Spizzo [117]. They are in between the results of calculations in the length form and in the velocity form obtained by Salomson [118], with many-body perturbation theory.

In Fig. 6.2, the theoretical results are convoluted with a Gaussian describing the appropriate photon band pass in order to facilitate a comparison with experimental

spectra. In Fig. 6.2(a), results of two measurements of the TCS, taken with a resolution of 4 meV (FWHM) [30] and 35 meV [34], respectively, are given. For the data of Domke *et al.* [30], taken with higher resolution and better signal-to-noise ratio, the cross section is given only in arbitrary units. Figure 6.2(b) and (c) show the experimental PCSs of Menzel *et al.* [34] measured with a resolution of 35 meV (FWHM). In Fig. 6.2(c), the results of Ref. [103], obtained with a resolution of 170 meV, are also plotted. It can be seen that the result of the present calculations agree well with the experimental data what resonance position, lineshape, and width are concerned. The TCS and the PCS σ_1 are about 5% larger than the only existing absolute experimental cross sections reported

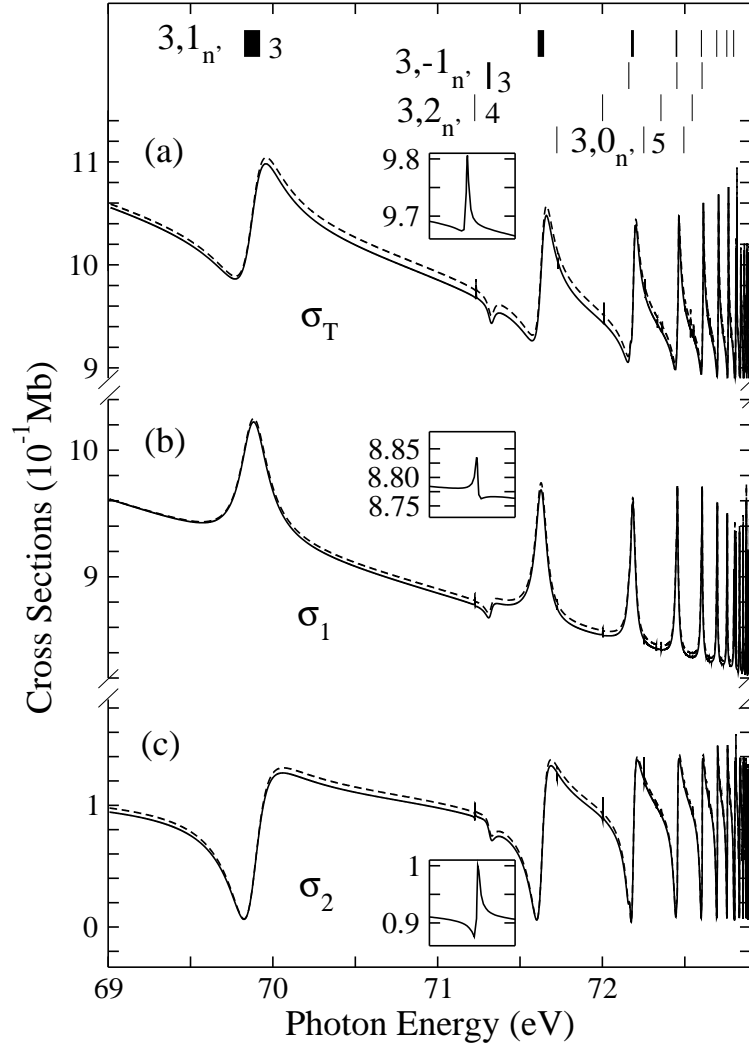


Figure 6.1: (a) Total photoionization cross section σ_T in the photon-energy region from 69.1 to 72.8 eV. In (b) and (c), the partial cross sections σ_1 and σ_2 are displayed. The solid lines and dashed lines represent the results obtained in the length form and in the velocity form, respectively. The insets give the resonance $3,2_4$ in the energy region from 71.22 to 71.25 eV on a magnified scale. The vertical bar diagrams in the upper part of the figure represent the assignment of the double-excitation resonances as obtained from theoretical calculations [31]. The widths of the vertical bars are proportional to the resonant linewidths.

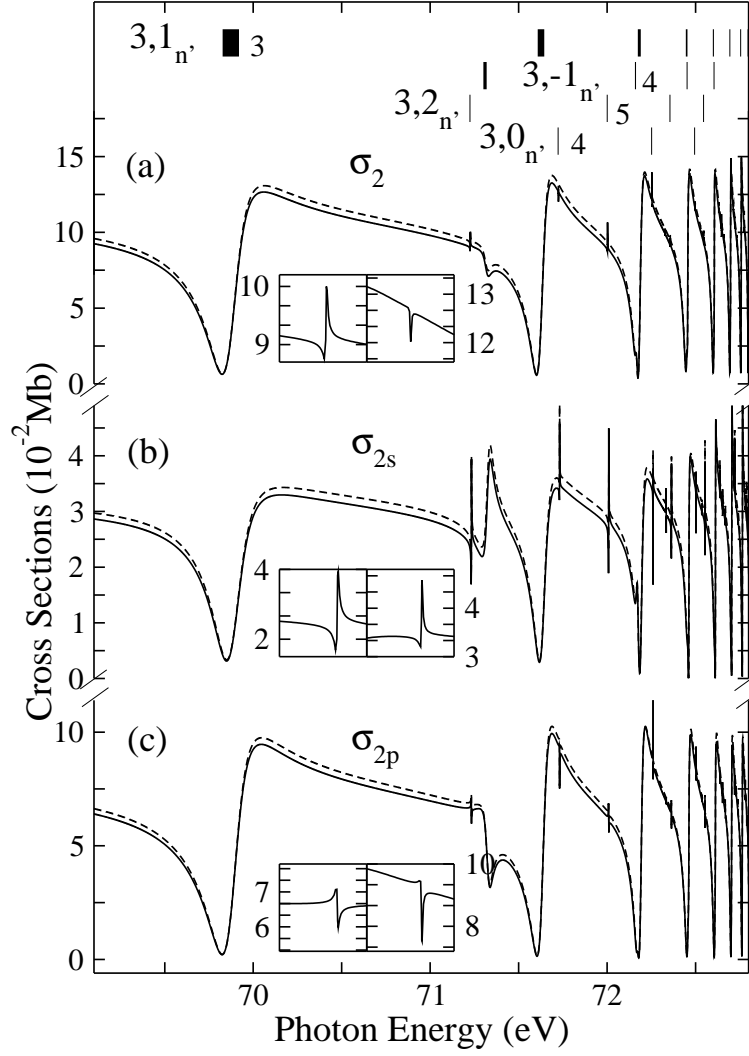


Figure 6.3: Partial photoionization cross sections (a) σ_2 , (b) σ_{2s} , and (c) σ_{2p} in the energy region from 69.1 to 72.8 eV. The left insets show the resonance $3,2_4$ in the energy region from 71.20 to 71.25 eV in magnified form, while the right insets show the $3,0_4$ resonance in the energy region from 71.70 to 71.75 eV. For further details, see Figs. 6.1 and 6.2.

as the maximum fractional depth of the minimum in the vicinity of a resonance in the sum of two individual PCSs. It loses its physical meaning defined by the Fano profiles for the TCSs, however. As a result, the analysis given in Sect. 5.3 can be employed to discuss and understand the mirroring and mimicking behaviors of any two individual PCSs although the sum of them are not the TCS, such as obtained in case of σ_{2s} and σ_{2p} (see Fig. 6.3). Because of $\rho^2 \rightarrow 1$, the resonances of the principal series $3,1_{n'}$ mimic each other in σ_{2s} and σ_{2p} , as expected by Liu and Starace [36]. Most of the secondary series exhibit $\rho^2 \rightarrow 0$ and show much stronger variations in σ_{2s} and σ_{2p} than in σ_2 , so that the prerequisites for mirroring behavior are fulfilled [37, 36]. The insets in Fig. 6.3 show that the resonances $3,2_4$ and $3,0_4$ actually display a mirroring behavior.

6.2.2 Angular distribution parameters β_{nl}

As compared to the PCSs, the ADPs show different dependences on the matrix elements for excitation and decay of the autoionization states. This can lead to the situation that a resonance is clearly seen in the PCSs but not in the ADPs or vice versa. In particular, the ADPs depend also on the phases of the matrix elements. In the LS-coupling scheme, the l -specific ADPs, β_{nl} , depend on the matrix elements and phase differences between the two different partial waves $\varepsilon(l-1)$ and $\varepsilon(l+1)$ of the outgoing electrons. The ADPs can be expressed in an effective spherically symmetric potential by [119]

$$\beta_{nl} = \frac{l(l-1)R_{nl,\varepsilon(l-1)}^2 + (l+1)(l+2)R_{nl,\varepsilon(l+1)}^2}{(2l+1)[lR_{nl,\varepsilon(l-1)}^2 + (l+1)R_{nl,\varepsilon(l+1)}^2]} \quad (6.9)$$

$$- \frac{6l(l+1)R_{nl,\varepsilon(l-1)}R_{nl,\varepsilon(l+1)}\cos(\delta_{l+1} - \delta_{l-1})}{(2l+1)[lR_{nl,\varepsilon(l-1)}^2 + (l+1)R_{nl,\varepsilon(l+1)}^2]}, \quad (6.10)$$

with $R_{nl,\varepsilon(l\pm 1)}$ being the radial integrals and $\delta_{l\pm 1}$ the background phases that can be considered to be constant in the region of the resonance [46]. Note that $\sigma_{nl} \propto lR_{nl,\varepsilon(l-1)}^2 + (l+1)R_{nl,\varepsilon(l+1)}^2$.

The interaction of a bound state with a continuum leads to an increase in the phase of the continuum wave function. The resulting effects on σ_{nl} and β_{nl} are described by the $R_{nl,\varepsilon(l\pm 1)}$, which – in the vicinity of a resonance – depend strongly on energy; the corresponding variations in $R_{nl,\varepsilon(l\pm 1)}^2$ can be parametrized by the Fano formula. In the following we shall briefly discuss the possibility of different behaviors of σ_{nl} and β_{nl} in the vicinity of a resonance. By assuming perfect mimicking of a resonance in $\sigma_{nl,\varepsilon l+1}$ and $\sigma_{nl,\varepsilon l-1}$, i.e. $\sigma_{nl,\varepsilon l-1} = c^2 \cdot \sigma_{nl,\varepsilon l+1}$ and $R_{nl,\varepsilon l-1} = c \cdot R_{nl,\varepsilon l+1}$, with c being a constant value, one obtains

$$\begin{aligned} \beta_{nl} &= \frac{[l(l-1) \cdot c^2 + (l+1)(l+2) - c \cdot 6l(l+1)\cos(\delta_{l+1} - \delta_{l-1})]}{(2l+1)(c^2 \cdot l + l + 1)} \\ &= \text{const.} \end{aligned} \quad (6.11)$$

From this we can conclude that resonances with strong variations in σ_{nl} may cause only small variations in β_{nl} if $\sigma_{nl,\varepsilon l+1}$ mimics $\sigma_{nl,\varepsilon l-1}$. A good example for this is the resonance $4,0_4$ that exhibits a strong variation in σ_{3d} (see Fig. 6.9), but only small variations in β_{3d} (see Fig. 6.11), as discussed above. Unfortunately, the corresponding PCSs $\sigma_{3d,\varepsilon p}$ and $\sigma_{3d,\varepsilon f}$ are not available from calculations so that the assumed mimicking behavior cannot be verified. If $\sigma_{nl,\varepsilon(l+1)}$ and $\sigma_{nl,\varepsilon(l-1)}$ show a mirroring behavior, the numerator and denominator of equation (6.10) change independently. Under these conditions we found in simulations that β_{nl} can vary strongly in the resonance region although there are no variations in σ_{nl} .

In LS coupling, all ADPs β_{ns} are identical to 2. Therefore, in Fig. 6.4 we only display the results for β_2 and β_{2p} below the SIT I_3 . In this figure, the results for β_2 and β_{2p} of both calculations (length form and velocity form) are almost identical, revealing again the quality of the target states used in the calculations. All five Rydberg series can

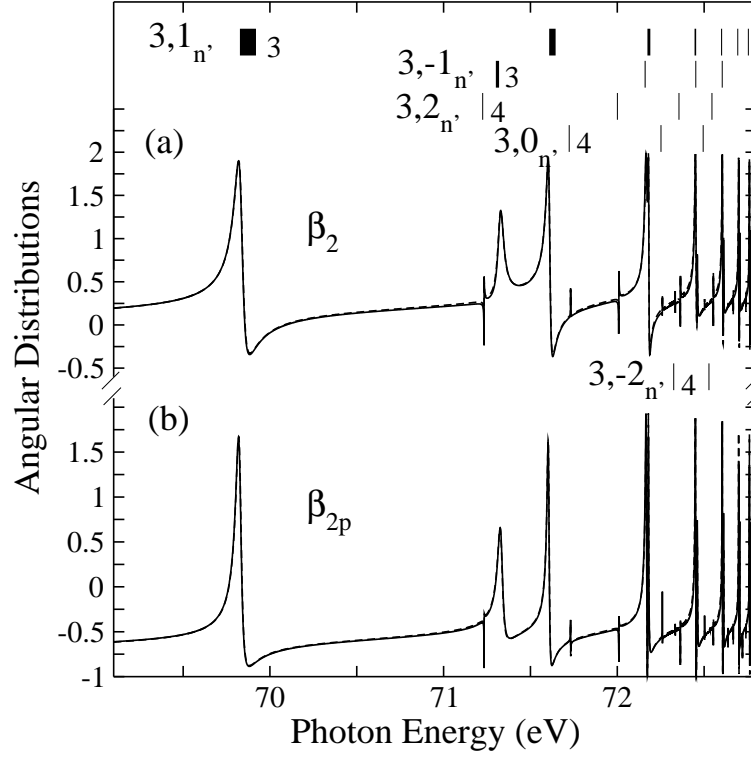


Figure 6.4: Angular distribution parameters (a) β_2 and (b) β_{2p} in the energy region from 69.1 to 72.8 eV. For further details, see Fig. 6.1.

be clearly seen in the curves for β_2 and β_{2p} . Because of the mimicking behavior of σ_{2s} and σ_{2p} in the series $3, 1_{n'}$, i.e. $\rho^2 \rightarrow 1$, we readily obtain from Eq. (6.1) the relation $\beta_2 = (2\sigma_{2s}^0 + \sigma_{2p}^0 \beta_{2p}) / \sigma_2^0$. Based on this expression, we then realize that β_2 and β_{2p} exhibit a similar energy dependence, and the mimicking behavior of β_2 and β_{2p} for the principal series $3, 1_{n'}$ can be readily understood. The mimicking of resonance $3, -1_3$ in β_2 and β_{2p} , however, is expected to be accidental due to the accidental mirroring behavior of σ_{2s} and σ_{2p} . Compared to previous theoretical calculations [117, 118], the present results generally reflect good agreement in magnitudes, peak positions, and line shapes. It should be noted that in the calculations of Sánchez and Martín [120], the principal series $3, 1_{n'}$ show an almost symmetric variation in the β_{2p} , while we find a rather asymmetric profile for these series.

The present results for the angular distribution parameters, convoluted with a Gaussian of 12 meV width, and the previously published results of the high resolution measurements of β_2 by Menzel *et al.* [34] are presented in Fig. 6.5. The experimental results of Zubek *et al.* [122], measured with a resolutions of 60 meV, and those of Lindle *et al.* [103], recorded with a resolution of 170 meV, are also given. In general, a good agreement between theory and experiments can be observed. However, with increasing photon energy, the values of Menzel *et al.* decrease in magnitude as compared to those of Zubek *et al.*. Close to the $N = 3$ ionization threshold, the ADPs of Menzel *et al.* are by $\cong 0.2$ lower than those of Zubek *et al.*, with the latter agreeing better with the present theoretical results. It should be noted that recent studies proved the geometry to be

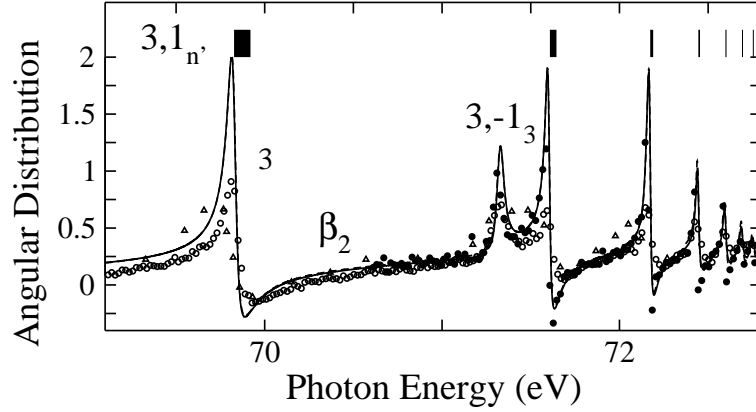


Figure 6.5: Angular distribution parameter β_2 in the energy region from 69.1 to 72.8 eV convoluted with a Gaussian of 12 meV. •, experimental data from Ref. [34], \triangle , from Ref. [103], \circ , from Ref. [122]. For further details, see Fig. 6.1.

important for measurements of the β -parameter. In particular, for a β determination, the measurements have to be done in the plane perpendicular to the direction of the photon beam. Contributions from out of this plane, caused by non-dipolar effects, can lead to wrong values of β [123, 124]. These non-dipolar effects in the angular distribution have been utilized by Krässig *et al.* [125] to detect the dipole-forbidden doubly excited resonances $^1D_2(2p^2)$ of helium. Such contributions of non-dipolar effects cannot be excluded as an explanation for the difference between theory and experimental by Menzel *et al.*, since no information was provided on the detection geometry in Ref. [35]. The present results and all available experimental data confirm clearly the observation of the state $3,-1_3$ in the spectrum.

6.3 Photoionization spectra below I_4

6.3.1 Partial cross sections σ_{nl}

The TCS σ_T and PCSs σ_1 , σ_2 , σ_3 for the photoionization processes below the SIT I_4 that lead to the channels $n = 1, 2$, and 3 are presented in Fig. 6.6(a-d). The results obtained in the velocity form are by $\cong 0.4$ to 3.8% larger in magnitude than those calculated in the length form; the shapes of the two curves, however, are almost identical. As observed for the states below the ionization threshold I_3 , the channel $n = 1$ is the most intense one due to strong contributions of direct photoionization dominating the TCS. Analogous to the situation below I_3 , the PCS σ_1 decreases quickly with increasing photon energy. All other resonance series besides the principal series are quite weak in the PCSs σ_n .

In Fig. 6.7(a), we show convoluted theoretical TCS and PCSs below I_4 , together with experimental results: the cross section in the upper part is convoluted with a Gaussian of 4.0 meV (FWHM) in order to allow a comparison with the relative experimental cross sections of Domke *et al.* [30]; in the lower part, the theoretical cross section is convoluted with a Gaussian of 35 meV (FWHM) to compare with the absolute cross sections of

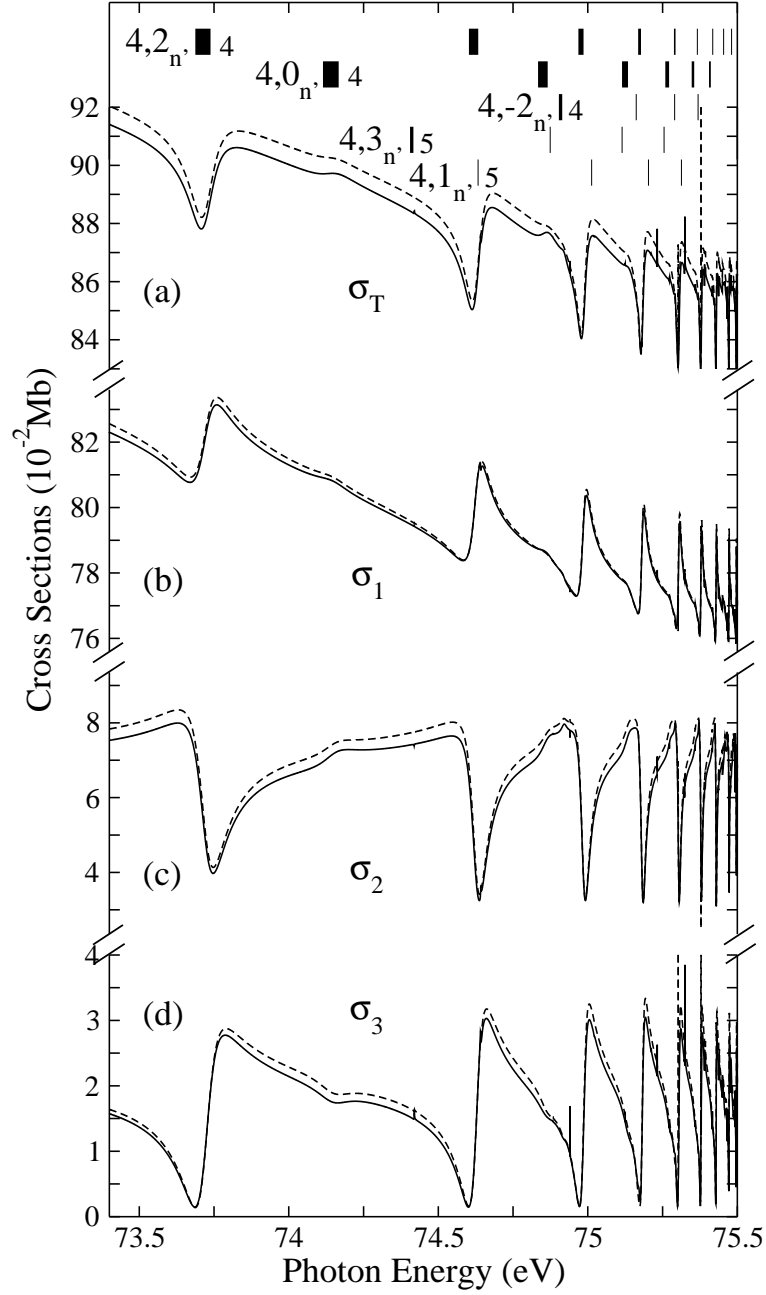


Figure 6.6: (a) Total cross section σ_T , (b) to (d) partial cross sections σ_1 to σ_3 in the energy region from 73.4 to 75.5 eV. For further details, see Fig. 6.1.

Menzel *et al.* [34]. The theoretical results agree well with the experimental results of Domke *et al.*, that revealed an asymmetric line shape with $q > 0$ for the principal series $4,2_{n'}$. In the experiments of Menzel *et al.*, however, the resonance profiles of the $4,2_{n'}$ series exhibit a ‘window-like’ lineshape, i.e. $q \cong 0$. In a direct comparison, the present theoretical cross sections agree within 6% with the only available absolute experimental results. This deviation slightly exceeds the combined error bars of the experimental and the theoretical data. The accuracy in the measurement of Menzel *et al.* is about 2% for σ_1 , 10% for σ_2 , and 13% for σ_3 . In addition, the present theoretical resonance positions

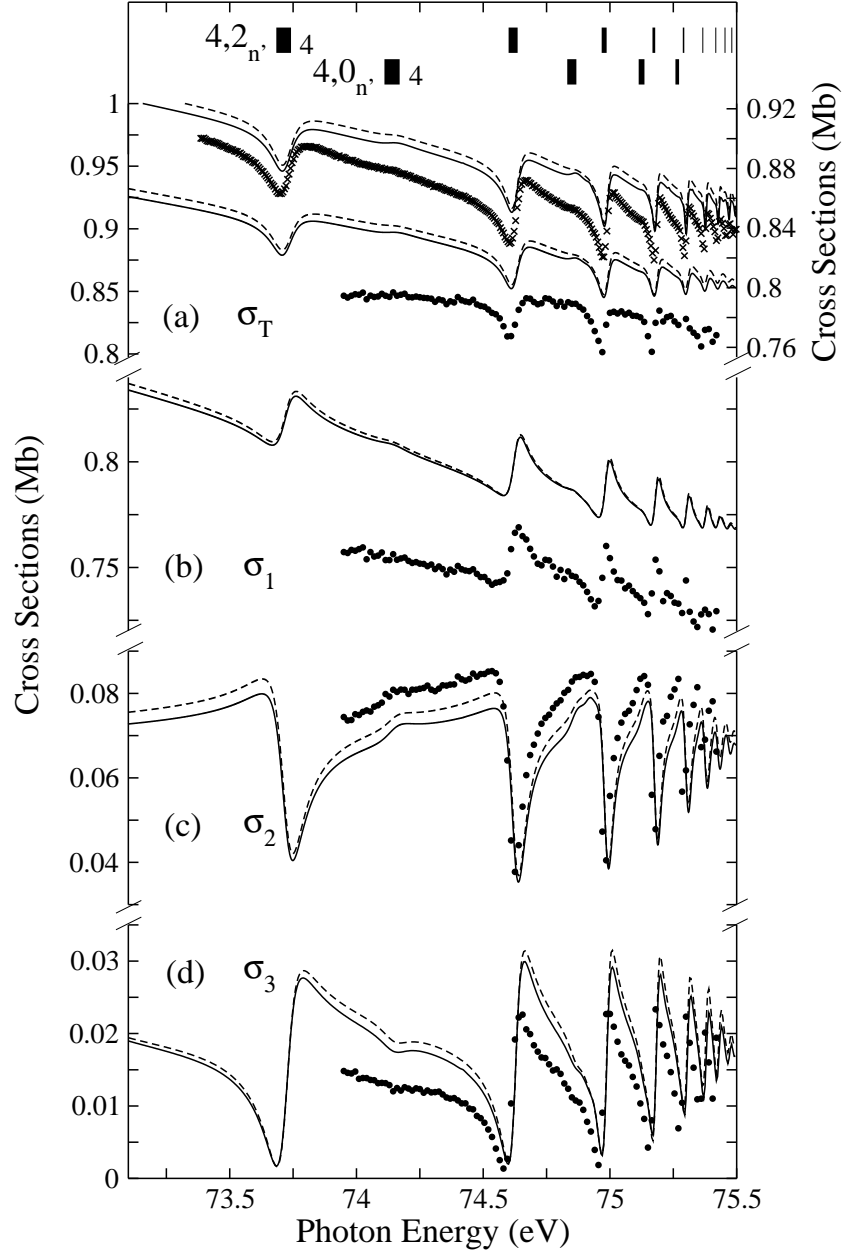


Figure 6.7: (a) TCS convoluted with a Gaussian of 4 meV (FWHM) (upper curves with scale on right ordinate) and 35 meV (lower curves with scale on left ordinate) in the energy region from 73.4 to 75.5 eV. (b) to (d), PCSs σ_1 , σ_2 , and σ_3 convoluted with a Gaussian of 35 meV. \times , related experimental data from Ref. [30], \bullet , from Ref. [34]. For further details, see Figs. 6.1.

are shifted slightly to higher energies by about 40 meV as compared to the experimental data. The present theoretical result as well as the calculations of Ref. [34] agree very well with regard to intensities, line widths, and shapes of the resonances; however, Menzel *et al.* gave no details of their calculations.

The theoretical l -specific PCSs σ_{2s} , σ_{2p} , σ_{3s} , σ_{3p} , and σ_{3d} are displayed in Figs. 6.8 and 6.9, together with the corresponding n -specific PCSs σ_2 and σ_3 . The PCSs σ_{np} dominate the PCSs σ_2 and σ_3 in Figs. 6.8 and 6.9 because of the strong coupling of the ground

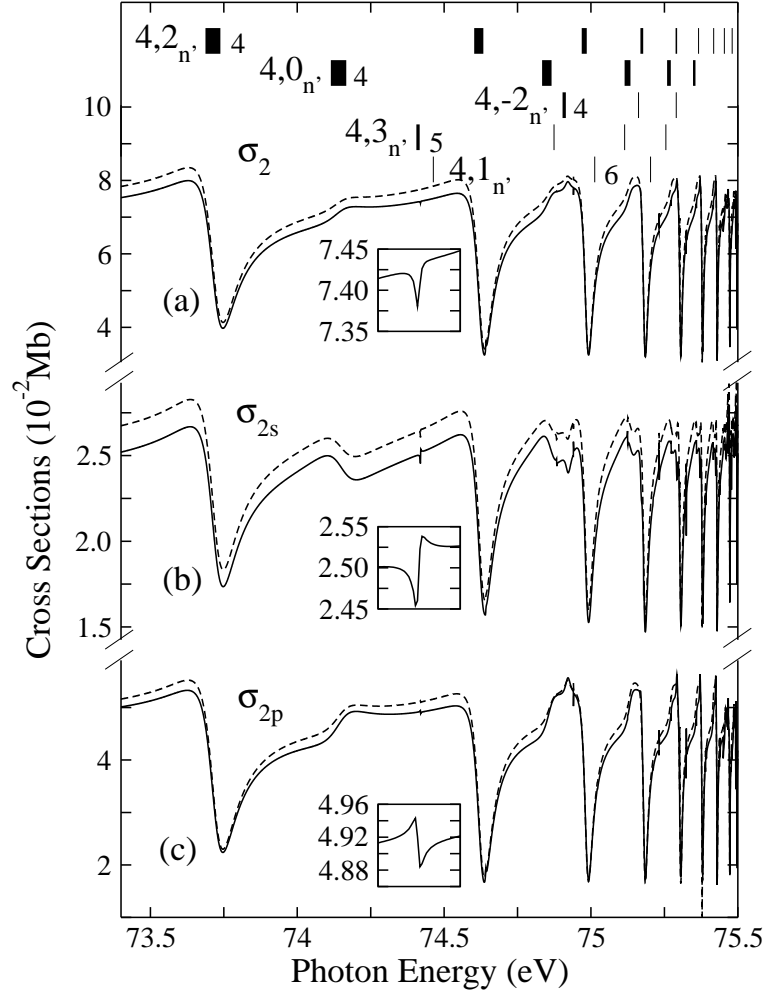


Figure 6.8: Partial photoionization cross sections (a) σ_2 , (b) σ_{2s} , and (c) σ_{2p} in the energy region from 73.4 to 75.5 eV. The insets show the resonance $4, 3_5$ in magnified form in the energy region from 74.41 to 74.43 eV. For further details, see Figs. 6.1 and 6.2.

state and the continuum states $2pn'l'$ and $3pn'l'$. The expected similarities in the σ_{nl} of the principal series have also been shown in Figs. 6.8 and 6.9, which can be explained by mimicking behavior. The overall agreement with the calculations of Sánchez and Martín [120] and with those of Hayes and Scott [121] is reasonable. However, in our calculations, σ_{3d} dominates over σ_{3s} in the entire energy region, while in the calculations of Hayes and Scott, the σ_{3d} partial cross section was consistently smaller than the σ_{3s} cross section at energies above 74.6 eV. Sánchez and Martín reported completely opposite results.

Very recently, Harries *et al.* [39] reported on the first measurements of l -specific PCSs σ_{2s} , σ_{2p} , σ_{3s} , σ_{3p} , and σ_{3d} below I_4 using a lifetime-resolved fluorescence technique; statistically improved data were later presented in Ref. [40]. The measurements of Ref. [39] are displayed in Fig. 6.10 along with the present calculations convoluted with a Gaussian of 10 meV (FWHM) in order to simulate the experimental resolution of the experiments. The relative intensities of the measurement are given on the right ordinate axis. The excellent agreement between theory and experiment confirms the high quality

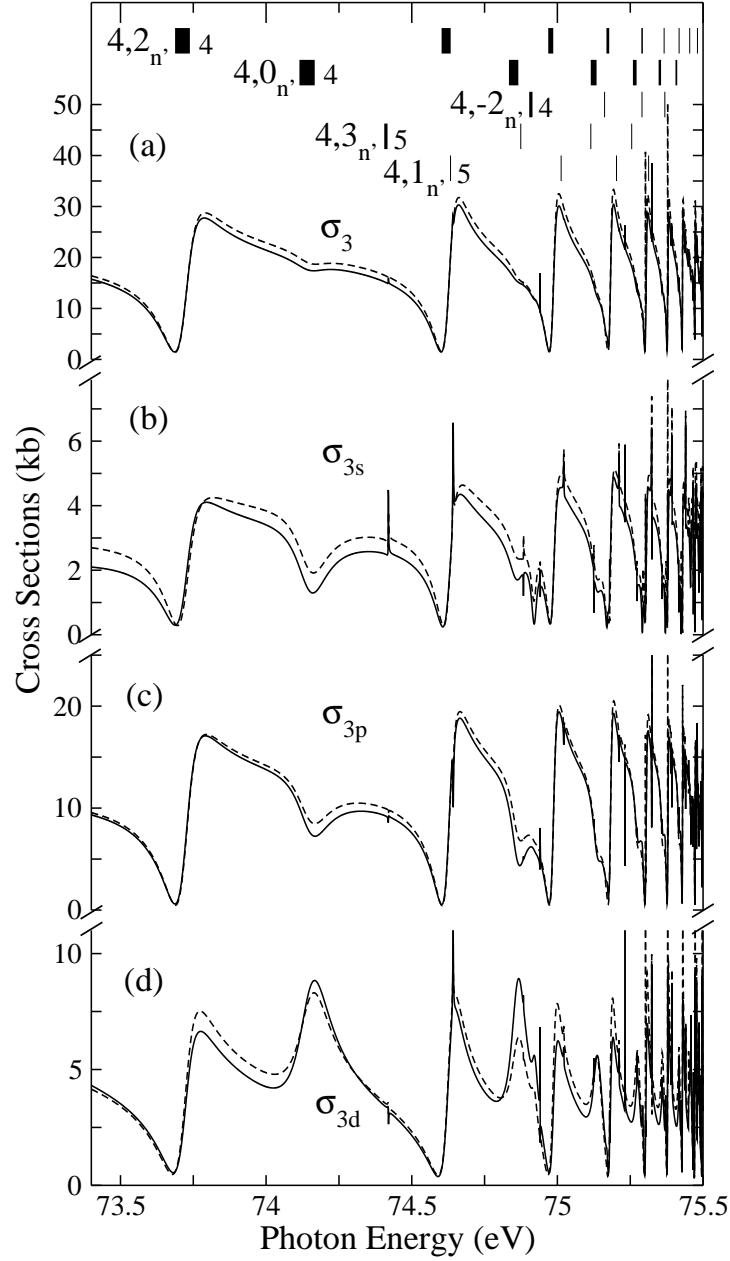


Figure 6.9: Partial photoionization cross sections (a) σ_3 , (b) σ_{3s} , (c) σ_{3p} , and (d) σ_{3d} in the energy region from 73.4 to 75.5 eV. For further details, see Figs. 6.1 and 6.2.

of the performed calculations. In the PCS σ_{3d} , the secondary series $4,0_{n'}$ shows the strongest coupling to this ionization channel. Therefore, the resonances $4,0_{n'}$ can be observed from $n' = 4$ to 8, which is shown in Fig. 6.10(e), with good agreement between experiment and theory. The experimental observations of the first resonance of the series $4,-2_{n'}$ also agree well with the present calculations. The first resonance of the $4,3_n$ series, namely $4,3_5$, is clearly visible in the theoretical partial cross section σ_{3s} convoluted with a Gaussian of 10 meV (FWHM); it also seems to be reproduced in the experimental results, although it is not discussed by the authors. However, the noise in the experiment is comparable to the expected intensity of the resonance $4,3_5$, i.e. the

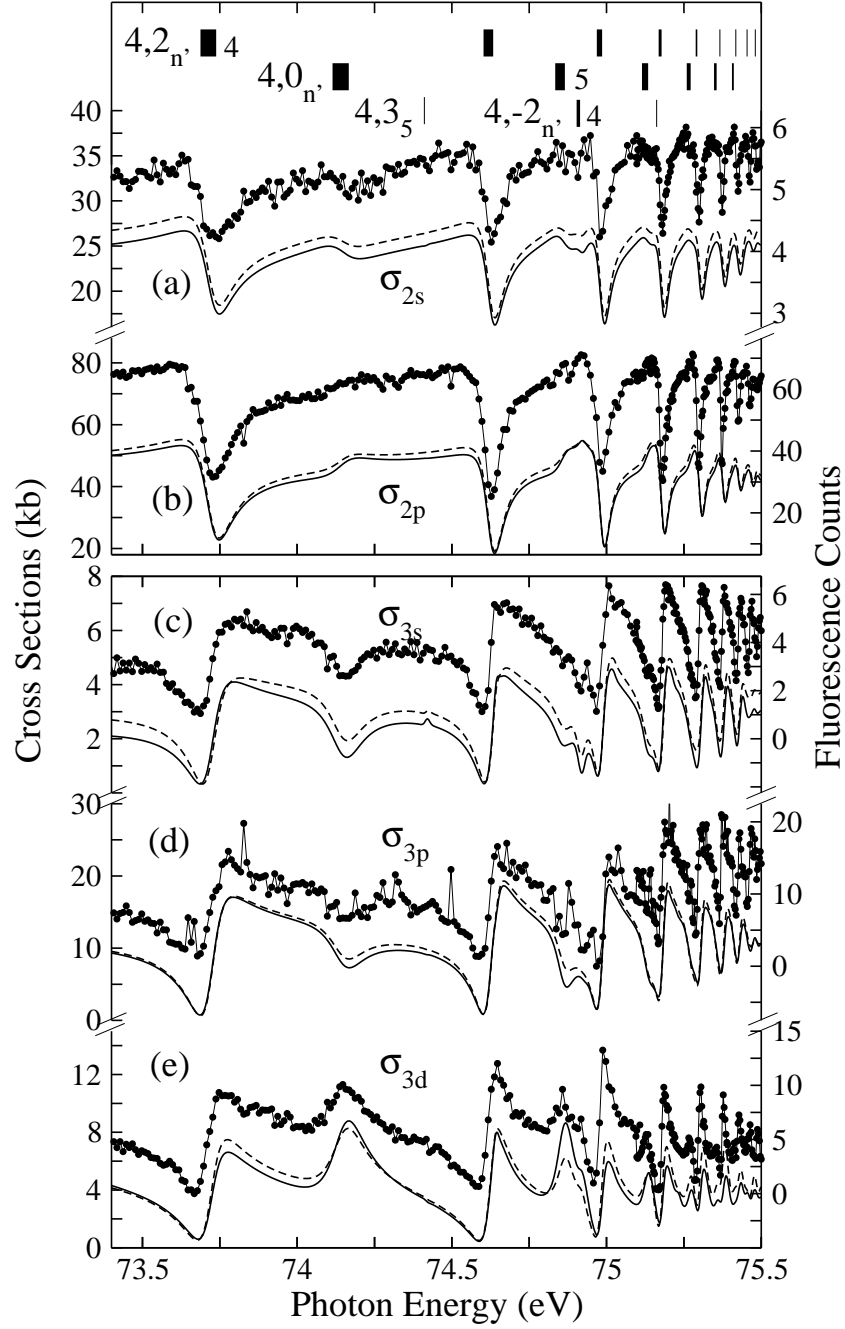


Figure 6.10: (a) l -specific partial photoionization cross sections σ_{2s} , σ_{2p} , σ_{3s} , σ_{3p} , and σ_{3d} convoluted with a Gaussian of 10 meV (FWHM) in the energy region from 73.4 to 75.5 eV (scale on left ordinate). The data points, connected by straight solid line (scale on right ordinate), represent experimental data from Ref. [39]. For further details, see Figs. 6.1 and 6.2.

observation of this resonance is not unambiguous. More recent experimental results [40], with improved signal-to-noise ratio, however, confirm the existence of the resonance $4, 3_5$. These recent data also show in general a better agreement with the present theoretical results. This is in particular valid for the resonance $4, 0_5$ in σ_{3p} . The lineshapes of the present calculations agree better with these measurements than those of Sánchez and

Martín shown in Ref. [39], in particular in case of σ_{3d} . The relative magnitudes from the measurements demonstrate that the PCS σ_{3d} always dominates over σ_{3s} , an observation that agrees well with our results, as discussed above.

6.3.2 Angular distribution parameters β_{nl}

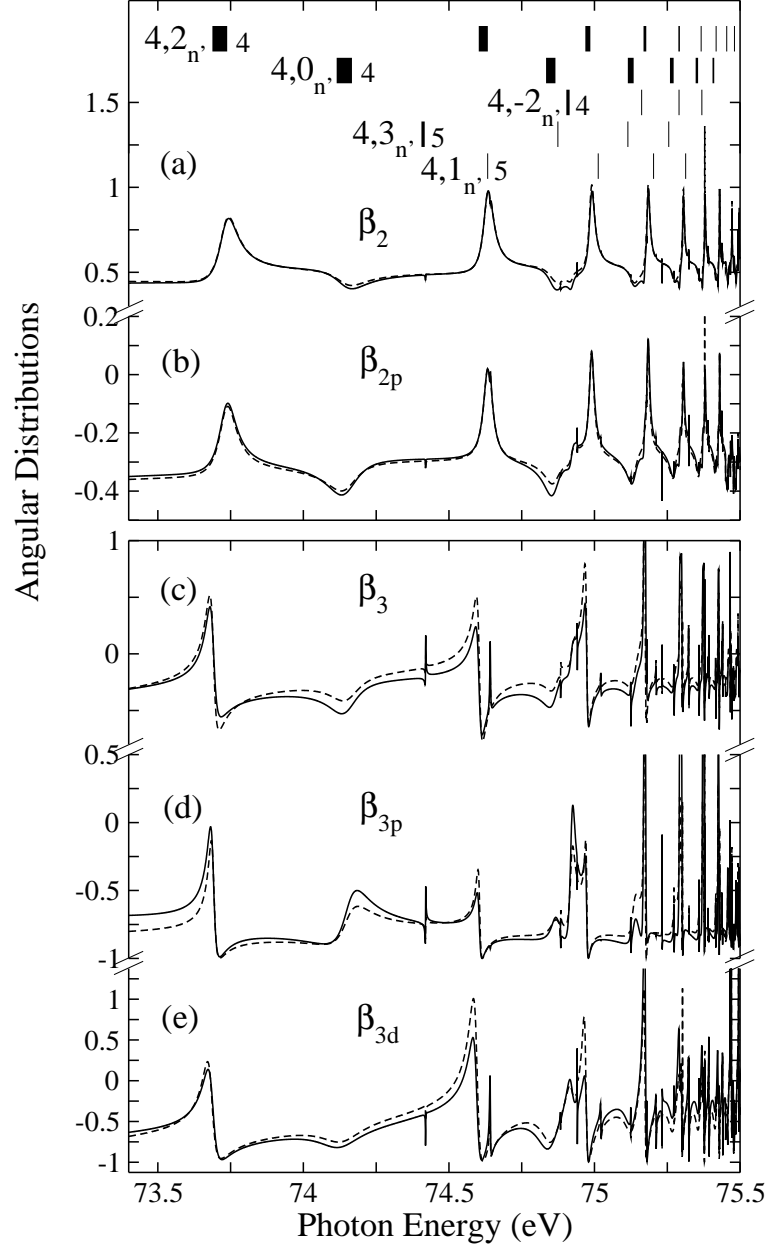


Figure 6.11: Angular distribution parameters (a) β_2 , (b) β_{2p} , (c) β_3 , (d) β_{3p} , and (e) β_{3d} in the energy region from 73.4 to 75.5 eV. For further details, see Fig. 6.1.

The theoretical ADPs β_2 , β_{2p} , β_3 , β_{3p} , and β_{3d} below I_4 are presented in Fig. 6.11(a-e). The 7 overlapping resonance series cause all comparable variations in β and this makes it very difficult to discuss the resonances separately, in particular in the l -specific β_{3l} .

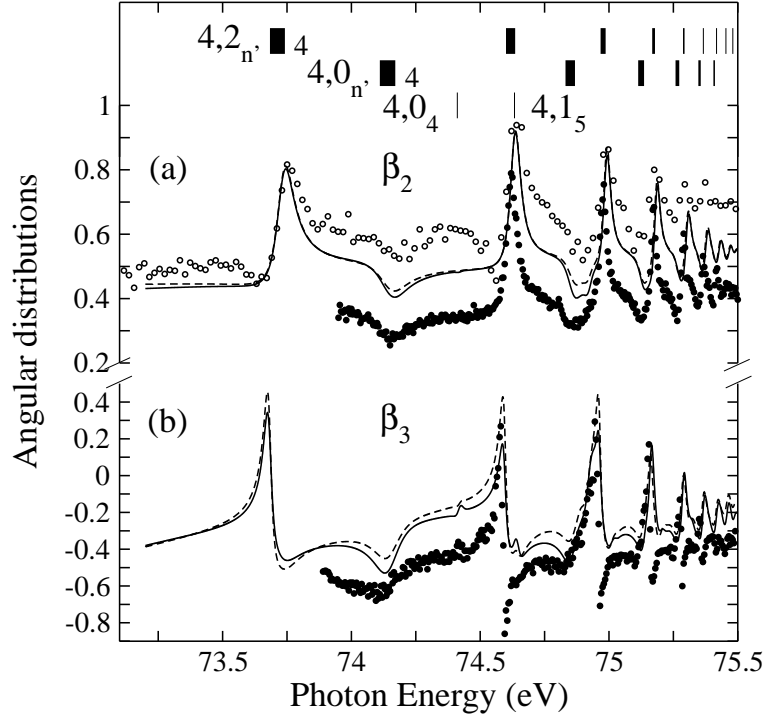


Figure 6.12: Angular distribution parameters (a) β_2 and (b) β_3 in the energy region from 73.1 to 75.5 eV, convoluted with a Gaussian of 12 meV. •, experimental data from Ref. [34]; ○, those from Ref. [122]. For further details, see Fig. 6.1.

Hayes and Scott [121] have also performed calculations of β_2 , β_3 , β_{3p} , and β_{3d} . However, considerable differences can be found between the two available calculations, e.g. some narrow peaks are missing in the calculated angular distribution parameters β_3 , β_{3p} , and β_{3d} of Hayes and Scott, such as the resonance 4,1₅. The mimicking behavior of β_2 and β_{2p} as well as of β_3 and β_{3l} of the resonance of the principal series 4,2_{n'} is shown in Fig. 6.11. It can also be understood on the basis of the mimicking behavior of the corresponding PCSs, as discussed before. With increasing energy, the overlap of 7 Rydberg series destroys the mimicking behavior. Although the present results are a considerable improvement compared to previously available theoretical calculations and experimental measurements, further advanced calculations and high-resolution measurements for l -specific ADPs are still necessary for this energy region.

In Fig. 6.12, the convoluted results for β_2 and β_3 are displayed together with experimental results of Menzel *et al.* [34] and Lindle *et al.* [103]. The present convoluted angular distribution parameters agree well with the theoretical results given in Ref. [34], which were obtained with the hyperspherical closed-coupling method. The β -values for both calculations are between the results of the two measurements presented in Fig. 6.12(a). The overall difference of 0.23 units between both experiments exceeds the given systematic experimental errors; as explained above, this could be due to non-dipolar effects. It should be mentioned that the energy positions of the resonances in β_2 and β_3 obtained in the present calculations show very good agreement with the experimental results of Lindle *et al.*

The present theoretical results have been published in Ref. [126]. Due to the absence of calculations for the n -specific ADPs below the SITs I_6 and I_7 , where our experiments had been performed (see previous chapter), the R-matrix method will be employed to calculate those ADPs in the near future.

Summary and Outlook

In this dissertation, the photoexcitation process and the subsequent autoionization decay of doubly excited helium were studied experimentally and theoretically in a broad photon energy region, where the spectra exhibit a characteristic change from strong electron correlation to quantum chaos.

On the experimental side, two different types of experiments were performed. The first type was the experimental study of the total cross sections (TCS) by measuring the total ion yield using a gas cell. With a high-resolution monochromators at the third generation synchrotron radiation sources the present studies of the TCSs were first extended to the single ionization threshold (SIT), I_{14} , of He^+ . These new data agree remarkably well with the results of very recent state-of-the-art complex-rotation calculations by Delande [27], which could be performed up to the SIT I_{17} . The present experimental spectra together with these confirmed theoretical results were employed to study signatures of quantum chaos in doubly excited helium in the region very close to double-ionization threshold.

The experimental spectra below each threshold can be described well by a describing fit using only few number (about 15) of resonances, where most of these resonances belong to the principal Rydberg series. Since there are normally several hundred of resonances in the region chosen for the fits, the resonances are strongly overlapping, a situation that in principle results in so-called Ericson fluctuations [26], i.e. one of the features of quantum chaos. On the basis of theoretical data, we found that the angular correlation quantum numbers K for the principal Rydberg series are still good quantum numbers at least up to the SIT I_{17} . Since the resonances with $K = N - 2$ carry most of the intensity of the cross sections, we can understand why the Ericson fluctuations were not observed in doubly excited helium although the spectra studied are in the Ericson regime, i.e. they are strongly overlapping. The present conclusions demonstrate that the conditions of comparable intensities for the resonances are needed to observe Ericson fluctuations. It is not reliable to prove the Ericson fluctuations only by the autocorrelation function with a Lorentzian form. The calculated K values are found to be good quantum numbers for resonances with $K \rightarrow K_{max}$ and $K \rightarrow K_{min}$, but not for $K \rightarrow 0$. These can be well understood by the classical collinear eZe and Zee configurations. On the basis of the present calculated K values for the principal Rydberg series, we analyzed the angular correlation mechanisms below and above the double-ionization threshold, which shows the photon double-ionization process is described by the same mechanism with photon single ionization, particularly for the regions very close to double-ionization threshold.

The assignment of the spectra was done for the first time up to I_{14} in this dissertation.

Statistical properties of the energy levels, linewidths, and Fano q parameters can also demonstrate quantum signatures of chaos. These statistical properties were studied on the basis of theoretical data [27], since only a small fraction of the resonances can be observed experimentally. In order to derive different aspects of quantum chaos different kinds of the nearest-neighbor spacings (NNS) were performed. First, a global analysis of the NNSs, i.e. all resonances were taken into account without further restriction. The distribution derived from this analysis results in a Poisson distribution up to the SIT I_{16} . This indicates that there are still independent subsystems, which can be identified by good quantum numbers like K . These studies prove the transition region from integrability to quantum chaos to be much large than expected before, since the quantum number K dissolves rather slowly. Full chaos in $^1P^o$ doubly excited helium may occur only at the double-ionization threshold. The slow transition towards chaos is analogous to the situation observed theoretically in doubly excited helium with $^1S^e$ symmetry [19]. Second, the Rydberg series with a well-defined K -value were analyzed individually. In this way, the loss of quantum numbers N can be confirmed for Rydberg series with $K \rightarrow K_{max}$ by the NNS distributions that clearly develop towards a Wigner distribution. The statistical NNS distribution below I_{17} matches almost a Wigner form, so that the transition from a Poisson-like distribution for a regular system towards a Wigner-like distribution for a chaotic system is almost completed. Since for Rydberg series with a well-defined K -value the angle between the two electrons and nucleus is constant, the 3-D helium atom can be considered to represent a stretched 1-D character with both electrons on opposite sites of the nucleus for $K \rightarrow K_{max}$. The Wigner-like form of K -selected NNS distributions for Rydberg series with $K \rightarrow K_{max}$ shows a quantum signature of chaos for the stretched “1-D” cases of real 3-D helium. These “1-D” cases in 3-D helium agree very well with those obtained for 1-D helium as presented by Püttner *et al.* [18], and we confirm the prediction that a full Wigner distribution will be found around I_{17} . We also employed statistical tools for studies of the linewidths and the Fano q parameters, which exhibit a Porter-Thomas distribution and a Lorentzian form, respectively. Both distributions are considered to be characteristics of a chaotic systems, and the present statistical studies for the Fano q parameters are the first confirmation of the theoretical predictions [84]. In summary, a number of features typically for chaotic systems are found for the doubly excited states of helium. In order to answer the open question if Ericson fluctuations are present in the spectra of doubly excited helium, the cross section below a number of additional thresholds have to be studied experimentally and theoretically.

With time-of-flight electron spectrometer, the partial cross sections (PCS) below the SITs I_5 to I_9 [37, 104] and the angular distribution parameters (ADP) below the SITs I_5 to I_7 were performed. The measurements for the PCS below the SITs I_6 to I_9 were performed for the first time and show a very good agreement with eigenchannel R-matrix calculations [33]. It was shown that the PCSs display additional information about the doubly excited states of helium. For example, the resonance $8, 4_{10}$ of the secondary series was resolved for the first time in the present PCS in contrast to the TCS, although the

latter one was measured with higher resolution and better signal-to-noise ratio. For the lower ionization thresholds we confirmed so-called general pattern in the PCSs which were explained theoretically by Schneider *et. al.* [33] with the propensity rules derived from a molecular description of helium. We also showed experimentally that these general patterns disappear with an increasing number of perturbers. In addition, an analytical expression for the mirroring behavior [36] was extended to a more general case. This allowed us to understand the mirroring behavior in doubly excited helium and to discuss it in a more general way: we realized that the mirroring behavior between two groups of PCSs can only occur accidentally, although $\rho^2 \rightarrow 0$. This is due to the fact that the amplitudes of the variations in the PCS and in the TCS are of the same order of magnitude. Further, the ADPs below the SITs I_5 to I_7 were measured, and the data below the SITs I_6 to I_7 are new. The additional resonance $6, 2_8$ was observed in the present ADP measurements for the first time. All statistical studies for quantum chaos had to be done on the basis of theoretical results. The present experimental results for these PCSs and ADPs can however substantiate the applied theoretical methods, and, in this way, assure the validity of these statistical analysis on the basis of theoretical data. In addition, since the PCSs and the ADPs carry additional coupling informations of the outgoing channel, quantum chaos is expected to manifest itself more clearly or in different ways in these data as compared to the TCS. Vice versa, the success of the present experimental and theoretical study of TCSs in such a high excited region will initiate further studies of PCSs and ADPs.

In the last part of dissertation, detailed R-matrix calculations on the n - and l -specific PCSs and ADPs leading to all possible accessible ionization channels (nl) were performed for the energy regions below the SITs I_3 and I_4 . In these regions, the approximate quantum numbers reflecting the strong electron correlation can be used to identify the spectra with physical meaning. The good agreement with the measurements proves the quality of the used target wave functions. In particular, it is encouraging to find almost perfect agreement between the present calculations [126] and very recent measurements [39, 40] of l -specific PCSs below the SIT I_4 . Mirroring behavior for other series were also analyzed and similarity to the principal series were found with respect to mirroring behavior. As $\rho^2 \rightarrow 1$, we observe that the principal series below the SITs I_3 and I_4 mimic each other in the l -specific PCSs, which is also the reason why mimicking behavior is found for the principal series among the n - and l -specific ADPs.

In the near future, with the ball chamber which was used to measure the ADPs in this moment the no-dipole effect of doubly excited helium will be studied. The expected forward-backward asymmetry of the outgoing electrons relative to the propagation direction of light will allow to access the final states with a total symmetry different from $^1P^o$. In addition, the set-up of metastable helium source is on the way, which can be used for the observations of photoionization process of $^3P^o$ doubly excited helium.

Acknowledgements

I would like to take the opportunity to express my sincere gratitude to the people who helped me to achieve this dissertation.

First of all, I want to thank my supervisors Prof. Dr. G. Kaindl and Prof. Dr. J. M. Rost for the possibility to start this work and for arranging the financial support. I benefit greatly from their scientific insights and foresights to this project, which, together with a lot of valuable comments, were the guarantee to successfully complete this doctoral dissertation.

Second, I am strongly indebted to my daily adviser Dr. R. Püttner, for his fruitful supervision. Within 5 years, I shared his rich ideas of science as well as friendship. I was benefited significantly from his deep knowledge and many critical discussions as well as constant assistance in all possible ways.

Special appreciations go to Prof. Dr. U. Becker for his pleasant cooperation on the TOF measurements, and I always enjoyed his constructive scientific comments. In his group, R. Hentges, Dr. J. Viefhaus, and Dr. M. Braune were strongly involved in the TOF measurements, and they really contributed to my scientific success.

Pleasant thanks are sent to Prof. D. Delande from Universite Pierre et Marie Curie in Paris, who allowed me to use his theoretical data to analyze the absorption spectra in the dissertation. It is his contribution that makes my studies on quantum chaos so very exciting.

Thanks are also due to Dr. M. Martins for his inputs in the beginning of my doctoral work and for sharing his fruitful and valuable discussions.

Finally, I want to thank all members and colleagues of the group of Prof. Kaindl for the friendly, helpful, and frequent discussions as well as the help they provided me in many ways. Special thanks go also to M. Poiguine for his help during many of the measurements.

Without the everlasting support and understanding of my wife, my son, and my daughter, however, I would not have managed to come this far; thank you very much.

Appendix A

Semiclassical case of helium at double-ionization threshold

In the following it will be shortly discussed why quantum chaos is expected close to the double-ionization threshold of helium. For this we will consider the Hamiltonian of classical helium, which can be read as

$$H = \frac{\mathbf{p}_1^2 + \mathbf{p}_2^2}{2} - \frac{2}{\mathbf{r}_1} - \frac{2}{\mathbf{r}_2} + \frac{1}{\mathbf{r}_1 + \mathbf{r}_2} = E, \quad (\text{A.1})$$

where E is the total energy relative to the double-ionization threshold. If E is positive both electrons can escape, which corresponds to the double-ionization of helium. The region $E < 0$ is more interesting since it represents the region of the doubly excited states. Taking negative energies E into account, one can scale the coordinates as

$$\mathbf{r}_i = \frac{\tilde{\mathbf{r}}_i}{-E} \quad \mathbf{p}_i = \sqrt{-E} \tilde{\mathbf{p}}_i,$$

and then, the Hamiltonian of classical helium becomes

$$H = \frac{\tilde{\mathbf{p}}_1^2 + \tilde{\mathbf{p}}_2^2}{2} - \frac{2}{\tilde{\mathbf{r}}_1} - \frac{2}{\tilde{\mathbf{r}}_2} + \frac{1}{\tilde{\mathbf{r}}_1 + \tilde{\mathbf{r}}_2} = -1. \quad (\text{A.2})$$

This transformation shows that the dynamics of classical helium remains invariant under variations of the energy since (A.2) can always be obtained by a simple scaling transformation. Under the scaling, the uncertainty principle can be given by

$$\tilde{\hbar} = \Delta \tilde{\mathbf{r}}_i \cdot \Delta \tilde{\mathbf{p}}_i = (-E) \mathbf{r}_i \cdot \frac{\mathbf{p}_i}{\sqrt{-E}} = \sqrt{-E} \hbar. \quad (\text{A.3})$$

As can be seen from (A.3), Planck constant in the rescaled coordinates, $\tilde{\hbar}$, approaches zero as $E \rightarrow 0$. Therefore, according to Bohr's correspondence, in the region close to the double-ionization threshold, helium can be described as a semiclassical way where quantum chaos is expected because of the non-integrability in classical helium.

Appendix B

Random matrix theory

Random matrix theory [64, 65], developed in the nineteen fifties and sixties, is a quite successful tool to study the level fluctuations in the quantum spectra of a chaotic system. In this theory, the quantum chaos is accounted for by representing the Hamiltonian by a matrix whose elements are randomly chosen; this represents the minimum knowledge about the system. The construction of a Gaussian ensembles will be illustrated by considering real symmetric 2×2 matrices with $O(2)$ symmetry as their group of orthogonal transformations. What we are seeking is a probability density $P(H)$ of three independent matrix elements H_{11} , H_{22} and H_{12} under the normalization condition

$$\int_{-\infty}^{+\infty} P(H) dH_{11} dH_{22} dH_{12} = 1. \quad (\text{B.1})$$

Two requirements, which take into account very principal physical ideas, suffice to determine $P(H)$. First, $P(H)$ must be invariant under the orthogonal transformation of the two-dimensional basis, i.e.

$$P(H) = P(H'), \quad H' = OHO^T. \quad (\text{B.2})$$

Second, the three independent matrix elements must be uncorrelated. The probability density $P(H)$ must therefore be the product of the three densities,

$$P(H) = P_{11}(H_{11})P_{22}(H_{22})P_{12}(H_{12}). \quad (\text{B.3})$$

This assumption can be interpreted as one of minimum-knowledge input or of maximum disorder. The transformation matrix $O(2)$ can be written by

$$O = \begin{pmatrix} \cos\Theta & -\sin\Theta \\ \sin\Theta & \cos\Theta \end{pmatrix}. \quad (\text{B.4})$$

One can consider an infinitesimal ($\Theta \rightarrow 0$) orthogonal transformation of the basis, and obtains

$$O = \begin{pmatrix} 1 & -\Theta \\ \Theta & 1 \end{pmatrix}. \quad (\text{B.5})$$

Considering $H' = OHO^T$, the matrix elements result in

$$\begin{aligned} H'_{11} &= H_{11} - 2\Theta H_{12} \\ H'_{22} &= H_{22} + 2\Theta H_{12} \\ H'_{12} &= H_{12} + \Theta(H_{11} - H_{22}). \end{aligned} \quad (\text{B.6})$$

According to the invariance given in Eq. (B.2), the factorization and the invariance of $P(H)$ yield

$$P(H) = P(H) \left\{ 1 - \Theta \left[2H_{12} \frac{d \ln P_{11}}{dH_{11}} - 2H_{12} \frac{d \ln P_{22}}{dH_{22}} - (H_{11} - H_{22}) \frac{d \ln P_{12}}{dH_{12}} \right] \right\}. \quad (\text{B.7})$$

Since the infinitesimal angle Θ is arbitrary, its coefficient in Eq. (B.7) should vanish, i.e.

$$\frac{1}{H_{12}} \frac{d \ln P_{12}}{dH_{12}} - \frac{2}{H_{11} - H_{22}} \left(\frac{d \ln P_{11}}{dH_{11}} - \frac{d \ln P_{22}}{dH_{22}} \right) = 0 \quad (\text{B.8})$$

The solution of this equation is given by Gaussian function of the form

$$P(H) = C \exp[-A(H_{11}^2 + H_{22}^2 + 2H_{12}^2) - B(H_{11} + H_{22})]. \quad (\text{B.9})$$

B vanishes if the average energy, $\text{Tr}(H)$, is properly shifted to zero, A fixes the unit of energy, and C is determined by the normalization. Without the loss of generality, $P(H)$ can be written as

$$P(H) = C \exp[-A \text{Tr} H^2]. \quad (\text{B.10})$$

It can be shown the probability density (Eq. (B.10)) obtained from the 2×2 matrices in fact holds also for $M \times M$ matrices with arbitrary size.

By assuming that Hamiltonian matrix elements are described according to Eq. (B.10) the eigenvalues are given by

$$E_{\pm} = \frac{1}{2}(H_{11} + H_{22}) \pm \frac{1}{2} \left[(H_{11} - H_{22})^2 + 4H_{12}^2 \right]^{1/2}. \quad (\text{B.11})$$

With the help of the eigenvalues E_{\pm} , we obtain the diagonal matrix

$$D = \begin{pmatrix} E_+ & 0 \\ 0 & E_- \end{pmatrix}, \quad (\text{B.12})$$

and by an orthogonal transformation given by Eq. (B.4), one can write the matrix H as

$$H = O D O^T. \quad (\text{B.13})$$

This yields the following transformation between the elements H_{11} , H_{22} , H_{12} and the variables E_+ , E_- , Θ :

$$\begin{aligned} H_{11} &= E_+ \cos^2(\Theta) + E_- \sin^2(\Theta), \\ H_{22} &= E_- \cos^2(\Theta) + E_+ \sin^2(\Theta), \\ H_{12} &= (E_+ - E_-) \cos \Theta \sin \Theta. \end{aligned} \quad (\text{B.14})$$

The Jacobian determinant of this orthogonal transformation is given by,

$$\det(J) = \det \frac{\partial(H_{11}, H_{22}, H_{12})}{\partial(E_+, E_-, \Theta)} = E_+ - E_-. \quad (\text{B.15})$$

Because of

$$P(E_+, E_-, \Theta) = P(H) \det(J) \quad (\text{B.16})$$

and

$$\text{Tr} H^2 = E_+^2 + E_-^2, \quad (\text{B.17})$$

one obtain the distribution $P(E_+, E_-, \Theta)$ in the form:

$$P(E_+, E_-) = C |E_+ - E_-| \exp[-A(E_+^2 + E_-^2)]. \quad (\text{B.18})$$

Note that this form is independent of Θ . To calculate the distribution of nearest-neighbor-spacing (NNS), we should integrate the variables E_+ and E_- in the equation (B.18)

$$P(E_+, E_-) = C \int dE_+ \int dE_- \delta(S - |E_+ - E_-|) |E_+ - E_-| \exp[-A(E_+^2 + E_-^2)]. \quad (\text{B.19})$$

Setting the variables $S = E_+ - E_-$ and the variable $z = (E_+ + E_-)/2$, Eq. (B.19) can be written as

$$\begin{aligned} P(S) &= C' \int_{-\infty}^{\infty} dz S \exp[-A(S^2/2 + 2z^2)] \\ &= C' \sqrt{\frac{\pi}{2A}} S \exp(-AS^2/2). \end{aligned} \quad (\text{B.20})$$

A and C' can be evaluated by the normalization condition

$$\int_0^{\infty} dS P(S) = 1 \quad (\text{B.21})$$

and with the unit of energy set such that the mean spacing is unity, namely

$$\int_0^{\infty} dS S P(S) = 1. \quad (\text{B.22})$$

In the end, eq. (B.20) yields the Wigner distribution $P_W(S)$ given in Eq. (4.1)

$$P_W(S) = \frac{\pi}{2} S \exp(-\frac{\pi}{4} S^2). \quad (\text{B.23})$$

Bibliography

- [1] R. P. Madden and K. Codling, Phys. Rev. Lett. **10**, 516 (1963).
- [2] G. Tanner, K. Richter, and J. M. Rost, Rev. Mod. Phys. **72**, 497 (2000).
- [3] C. M. Marcus, A. J. Rimberg, R. M. Westervelt, P. F. Hopkins, and A. C. Gossard, Phys. Rev. Lett. **69**, 506 (1992).
- [4] K. Nakamura and T. Harayama, *Quantum Chaos and Quantum Dots* (Oxford University Press, 2004).
- [5] T. M. Fromhold, L. Eaves, F. W. Sheard, M. L. Leadbeater, T. J. Foster, and P. C. Main, Phys. Rev. Lett. **72**, 2608 (1994).
- [6] T. Guhr, A. Müller-Groeling, and H. A. Weidenmüller, Phys. Rep. **299**, 189 (1998).
- [7] M. C. Gutzwiller, J. Math. Phys. **12**, 343 (1971).
- [8] M. C. Gutzwiller, *Chaos in Classical and Quantum Mechanics* (Springer, New York 1990).
- [9] H. -J. Stöckmann, *Quantum Chaos* (Cambridge University Press, Cambridge 1999).
- [10] R. Blümel and W. P. Reinhardt, *Chaos in Atomic Physics* (Cambridge University Press, Cambridge 1997).
- [11] H. Friedrich and D. Wintgen, Phys. Rep. **183**, 37 (1989).
- [12] C. Iu, G. R. Welch, M. M. Kash, K. Hsu, and D. Keppner, Phys. Rev. Lett. **63**, 1133 (1989).
- [13] R. Niemeiner, G. Zeller, W. Schweizer, and G. Wunner, Comments on At. and Mol. Phys. **25**, 291 (1990).
- [14] D. Delande, A. Bommier, J. C. Gay, Phys. Rev. Lett. **66**, 141 (1991).
- [15] J. Zakrzewski, K. Dupret, and D. Delande, Phys. Rev. Lett. **74**, 522 (1996).
- [16] G. Stania and H. Walther, Phys. Rev. Lett. **95**, 194101 (2005).
- [17] J. Madronero and A. Buchleitner, Phys. Rev. Lett. **95**, 263601 (2005).

- [18] R. Püttner, B. Grémaud, D. Delande, M. Domke, M. Martins, A. S. Schlachter, and G. Kaindl, Phys. Rev. Lett. **86**, 3747 (2001).
- [19] A. Th. Le, T. Morishita, X. M. Tong, and C. D. Lin, Phys. Rev. A, **72** 032511 (2005).
- [20] U. Fano, Phys. Rev. **124**, 1866 (1961).
- [21] M. Domke, T. Mandel, A. Puschmann, C. Xue, D. A. Shirley, G. Kaindl, H. Petersen, and P. Kuske, Rev. Sci. Instrum. **63**, 80 (1992).
- [22] U. Becker, D. Szostak, H. G. Kerkhoff, M. Kupsch, B. Langer, R. Wehlitz, A. Yagishita, and T. Hayaishi, Phys. Rev. A, **39**, 3902 (1989).
- [23] D. R. Herrick and O. Sinanoğlu, Phys. Rev. A **11**, 97 (1975).
- [24] J. M. Feagin and J. S. Briggs, Phys. Rev. Lett. **57**, 984 (1986).
- [25] H. Friedrich, *Theoretical Atomic Physics* (Springer, Berlin, 1998).
- [26] T. Ericson, Phys. Rev. Lett. **5**, 430 (1960).
- [27] D. Delande, *private communication* (2004).
- [28] K. Richter, G. Tanner, and D. Wintgen, Phys. Rev. A **48**, 4182 (1993).
- [29] J-Zh. Tang and I. Shimamura, Phys. Rev. A **50**, 1321(1994).
- [30] M. Domke, K. Schulz, G. Remmers, and G. Kaindl, Phys. Rev. A **53**, 1424 (1996).
- [31] J. M. Rost, K. Schulz, M. Domke, and G. Kaindl, J. Phys. B **30**, 4663 (1997).
- [32] B. Grémaud and D. Delande, Europhys. Lett. **40**, 363 (1997).
- [33] T. Schneider, Ch. N. Liu, and J. M. Rost, Phys. Rev. A **65**, 042715 (2002).
- [34] A. Menzel, S. P. Frigo, S. B. Whitfield, C. D. Caldwell, M. O. Krause, J. Z. Tang, and I. Shimamura, Phys. Rev. Lett. **75**, 1479 (1995).
- [35] A. Menzel, S. P. Frigo, S. B. Whitfield, C. D. Caldwell, and M. O. Krause, Phys. Rev. A **54**, 2080 (1996).
- [36] Ch-N. Liu and A. Starace, Phys. Rev. A **59**, R1731 (1999).
- [37] Y. H. Jiang, R. Püttner, R. Hentges, J. Viefhaus, M. Poiguine, U. Becker, J. M. Rost, and G. Kaindl, Phys. Rev. A **69**, 042706 (2004).
- [38] Ch-N. Liu and A. Starace, Phys. Essays **13**, 2 (2000).
- [39] J. R. Harries, J. P. Sullivan, S. Obara, P. Hammond, and Y. Azuma, J. Phys. B **36** L319 (2003).

- [40] J. R. Harries, J. P. Sullivan, S. Obara, Y. Azuma, J. G. Lambourne, F. Penent, R. I. Hall, P. Lablanquie, K. Bucar, M. Zitnik, and P. Hammond, *J. Phys. B* **38**, L153 (2005).
- [41] J.-E. Rubensson, C. S  the, S. Cramm, B. Kessler, S. Stranges, R. Richter, M. Alagia, and M. Coreno, *Phys. Rev. Lett.* **83**, 947 (1999).
- [42] T. W. Gorczyca, J. E. Rubensson, C. S  the, M. Str  m, M. Ag  ker, D. J. Ding, S. Stranges, R. Richter, and M. Alagia, *Phys. Rev. Lett.* **85**, 1202 (2000).
- [43] J. W. Cooper, *Phys. Rev. A* **47**, 1841 (1993).
- [44] H. A. Bethe and E. E. Salpeter, *Quantum Mechanics of one- and two-electron Atoms* (Academic, New York, 1977).
- [45] V. L. Jacobs, *J. Phys. B* **5**, 2257 (1972).
- [46] N. M. Kabachnik and I. P. Sazhina, *J. Phys. B* **9**, 1681 (1976).
- [47] V. Schmidt, *Electron Spectrometry of Atoms using Synchrotron Radiation* (Cambridge University Press, 1997).
- [48] D. H. Tomboulion and P. L. Hartman, *Phys. Rev.* **102**, 1423 (1956).
- [49] K. J. Kim, K. Halbach, and D. Attwood, *Laser techniques in the extreme ultraviolet* (AIP Conf. Proc. Vol. 119, 1984).
- [50] M. Martins, G. Kaindl, and N. Schwentner, *J. Elec. Spectrosc. Rel. Phenom.* **101**, 965 (1999).
- [51] R. Z. Bachrach, F. C. Brown, and S. B. M. Hagstr  m, *J. Vac. Sci. Technol.* **12**, 309 (1975).
- [52] M. G. White, R. A. Rosenberg, G. Gabor, E. D. Poliakoff, G. Thornton, S. H. Southworth, and D. A. Shirley, *Rev. Sci. Instr.* **50**, 1268 (1979).
- [53] R. Hentges, *private communication*.
- [54] O. Hemmers, S. B. Whitfield, P. Glans, H. Wang, D. W. Lindle, R. Wehlitz, and I. A. Sellin, *Rev. Sci. Instr.* **69**, 3809 (1998).
- [55] F. Wuilleumier, M. O. Krause, *Phys. Rev. A* **10**, 242 (1974).
- [56] M. Wickenhauser, J. Burgd  rfer, F. Krausz, and M. Drescher, *Phys. Rev. Lett.* **94**, 023002 (2005).
- [57] U. Fano and J. W. Cooper, *Phys. Rev.* **137**, A1364 (1965).
- [58] U. Fano and J. W. Cooper, *Rev. Mod. Phys.* **40**, 441 (1968).

- [59] A. F. Starace, Phys. Rev. A **16**, 231 (1977).
- [60] U. Becker, *private communication*.
- [61] C. D. Lin, Phys. Rev. A **29**, 1019 (1984).
- [62] K. Schulz, G. Kaindl, M. Domke, J. D. Bozek, P. A. Heimann, A. S. Schlachter, and J. M. Rost, Phys. Rev. Lett. **77**, 3086 (1996).
- [63] H. W. van der Hart and C. H. Greene, Phys. Rev. A **66**, 022710 (2002).
- [64] T. A. Brody, J. Flores, J. B. French, P. A. Mello, A. Pandey, and S. S. M. Wong, Rev. Mod. Phys. **53**, 385 (1981).
- [65] F. Haake, *Quantum signatures of Chaos* (Springer, Berlin, 2001).
- [66] O. Bohigas, M. J. Giannoni, and C. Schmit, Phys. Rev. Lett. **52**, 1 (1984).
- [67] A. Hönig and D. Wintgen, Phys. Rev. A **39**, 5642 (1989).
- [68] T. Zimmermann, H. Köppel, L. S. Cederbaum, G. Persch, and W. Demtröd, Phys. Rev. Lett. **61**, 3 (1988).
- [69] M. Oxborrow and C. Ellegaard, *Proceedings of the 3rd Experimental Chaos Conference*, Edinburgh, Scotland, UK 1995.
- [70] S. Deus, P. M. Koch, and L. Sirko, Phys. Rev. E **52**, 1146 (1995).
- [71] O. Legrand, C. Schmit, and D. Sornette, Europhys. Lett. **18**, 101 (1992).
- [72] P. Von Brentano, J. Ernst, O. Häusser, T. Mayer-Kuckuk, A. Richter, and W. Von Witsch, Phys. Rev. Lett. **9**, 48 (1964).
- [73] J. Main and G. Wunner, Phys. Rev. Lett. **69**, 586 (1992).
- [74] K. Richter and D. Wintgen, J. Phys. B **23**, L197 (1990).
- [75] Y. Qiu, J. Müller, and J. Burgdörfer, Phys. Rev. A **54**, 1922 (1996).
- [76] N. N. Choi, M-H Lee, and G. Tanner, Phys. Rev. Lett. **93**, 054302 (2005).
- [77] D. Wintgen, A. Bürgers, K. Richter, and G. Tanner, Prog. Theor. Phys. Suppl. **116**, 121 (1994).
- [78] B. R. Junker, Adv. At. Mol. Phys. **18**, 207 (1982).
- [79] Y. K. Ho, Phys. Rep. **99**, 1 (1983).
- [80] W. Mahler, *private communication*.
- [81] A. Bürgers, D. Wintgen, and J. M. Rost, J. Phys. B **28**, 3163 (1995).

- [82] C. E. Porter and R. G. Thomas, *Phy. Rev.* **104**, 483 (1956).
- [83] B. Grémaud, D. Delande, and J. C. Gay, *Phy. Rev. Lett.* **70**, 1615 (1993).
- [84] W. Ihra, *Phys. Rev. A* **66**, 020701(R) (2002).
- [85] G. Wannier, *Phys. Rev.* **90**, 817 (1953).
- [86] A. R. P. Rau, *J. Phys. B* **9**, L283 (1976).
- [87] J. M. Feagin, *J. Phys. B* **17**, 2433 (1984).
- [88] P. L. Altick, *J. Phys. B* **18**, 1841 (1985).
- [89] A. K. Kazansky and V. N. Ostrovsky, *J. Phys. B* **26**, 2231 (1993).
- [90] A. Huetz, P. Lablanquie, P. Selles, and J. Mazeau, *J. Phys. B.* **27**, L13 (1994).
- [91] J. M. Rost, *Phy. Rev. Lett.* **72**, 1998 (1994); *J. Phys. B* **28**, 3003 (1995).
- [92] P. Lablanquie, J. Mazeau, L. Andric, P. Selles, and A. Huetz, *Phys. Rev. Lett.* **74**, 2192 (1995).
- [93] G. Dawber, L. Avaldi, A. G. McConkey, H. Rojast, M. A. MacDonald, and G. C. King, *J. Phys. B* **28**, L271 (1998).
- [94] J. M. Feagin, *J. Phys. B* **29**, L551 (1996).
- [95] R. Dörner, J. M. Feagin, C. L. Cocke, H. Bräuning, O. Jagutzki, M. Jung, E. P. Kanter, H. Khemliche, S. Kravis, V. Mergel, M. H. Prior, H. Schmidt-Böcking, L. Spielberger, J. Ullrich, M. Unversagt, and T. Vogt, *Phys. Rev. Lett.* **77**, 1024 (1996).
- [96] R. Dörner, H. Bräuning, J. M. Feagin, V. Mergel, O. Jagutzki, L. Spielberger, T. Vogt, H. Khemliche, M. H. Prior, J. Ullrich, C. L. Cocke, and H. Schmidt-Böcking, *Phys. Rev. A* **57**, 1074 (1998).
- [97] Y. H. Qiu and J. Burgdörfer, *Phys. Rev. A* **59**, 2738 (1999).
- [98] J. S. Briggs and V. Schmidt, *J. Phys. B* **33**, R1 (2000).
- [99] A. Huetz and J. Mazeau, *Phy. Rev. Lett.* **85**, 530 (2000).
- [100] A. Knapp, A. Kheifets, I. Bray, Th. Weber, A. L. Landers, S. Schössler, T. Jahnke, J. Nickles, S. Kammer, O. Jagutzki, L. Ph. H. Schmidt, T. Osipov, J. Rösch, M. H. Prior, H. Schmidt-Böcking, C. L. Cocke, and R. Dörner, *Phy. Rev. Lett.* **89**, 033004 (2002).
- [101] A. Y. Istomin, A. F. Starace, N. L. Manakov, A. V. Meremianin, A. S. Kheifets, I. Bray, *Phys. Rev. A* **72**, 052708 (2005).

- [102] A. Czasch, M. Schöffler, M. Hattass, S. Schössler, T. Jahnke, Th. Weber, A. Staudte, J. Titze, C. Wimmer, S. Kammer, M. Weckenbrock, S. Voss, R. E. Grisenti, O. Jagutzki, L. Ph. H. Schmidt, H. Schmidt-Böcking, R. Dörner, J. M. Rost, T. Schneider, Ch-N Liu, I. Bray, A. S. Kheifets, and K. Bartschat, *Phys. Rev. Lett.* **95**, 243003 (2005).
- [103] D.W. Lindle, T.A Ferrett, U. Becker, P. H. Kobrin, C. M. Truesdale, H. G. Kerkhoff, and D. A. Shirley, *Phys. Rev. A* **31**, 714 (1985).
- [104] Y. H. Jiang, R. Püttner, R. Hentges, J. Viefhaus, M. Poiguine, C. Cacho, U. Becker, J. M. Rost, and G. Kaindl, *J. Phys. B* **39** L9 (2006).
- [105] R. Wehlitz, B. Langer, N. Berrah, S. B. Whitfield, J. Viefhaus and U. Becker, *J. Phys. B* **26**, L783 (1993).
- [106] T. Schneider, *Doctoral Dissertation* (Max-Planck-Institut für Physik Komplexer Systeme, Dresden, Germany, 2002).
- [107] S. E. Canton-Rogan, A. A. Wills, T. W. Gorczyca, M. Wiedenhoef, O. Nayandin, Ch. N. Liu, and N. Berrah, *Phys. Rev. Lett.* **85**, 3113 (2000).
- [108] P. G. Burke, A. Hibbert, and W. D. Robb, *J. Phys. B* **4**, 153 (1971).
- [109] E. Clementi and R. Roetti, *At. Data Nucl. Data Tables* **14**, 177 (1974).
- [110] M. Le Dourneuf (unpublished); Vo ky Lan, M. Le Dourneuf, and P. G. Burke, *J. Phys. B* **9**, 1065 (1976).
- [111] J. Yan, Y. Z. Qu, Lan Vo ky, and J. M. Li, *Phys. Rev. A* **57**, 997 (1998).
- [112] C. L. Pekeris, *Phys. Rev.* **126**, 1470 (1962).
- [113] J. Mcl. Calvert and W. D. Davison, *J. Phys. B* **4**, 314 (1971).
- [114] J. A. Fernley, K. T. Taylor, and M. J. Seaton, *J. Phys. B* **20**, 6457 (1987).
- [115] C. E. Moore, *Atomic energy levels I* (U. S. GPO, Washington, 1971).
- [116] Y. H. Jiang, J. Yan, J. M. Li, J. F. Sun, and L. D. Wan, *Phys. Rev. A* **61**, 032721 (2000).
- [117] R. Moccia and P. Spizzo, *Phys. Rev. A* **43**, 2199 (1991).
- [118] S. Salomonson, S. L. Carter, and H. P. Kelly, *Phys. Rev. A* **39**, 5111 (1989).
- [119] J. Cooper and R. N. Zare, *J. Chem. Phys.* **48**, 942 (1968).
- [120] I. Sánchez and F. Martín, *Phys. Rev. A* **45**, 4468 (1992).
- [121] M. A. Hayes and M. P. Scott, *J. Phys. B* **21**, 1499 (1988).

- [122] M. Zubek, G. Dawber, R. I. Hall, L. Avaldi, K. Ellis, and G. C. King, *J. Phys. B* **24**, L337 (1991).
- [123] V. K. Dolmatov and S. T. Manson, *Phys. Rev. Lett.* **83**, 939 (1999).
- [124] A. Derevianko, O. Hemmers, S. Oblad, P. Glans, H. Wang, S. B. Whitfield, R. Wehlitz, I. A. Sellin, W. R. Johnson, and D. W. Lindle, *Phys. Rev. Lett.* **84**, 2116 (2000).
- [125] B. Krässig, E. P. Kanter, S. H. Southworth, R. Guillemin, O. Hemmers, D. W. Lindle, R. Wehlitz, and N. L. S. Martin, *Phys. Rev. Lett.* **88**, 203002 (2002).
- [126] Y. H. Jiang, R. Püttner, and G. Kaindl, *J. Phys. B* **38**, 2157 (2005).

Curriculum Vitae

Name: Yuhai Jiang
Sex: Male
Date and place of birth: Nov. 20, 1969; Henan, P.R. China
Nationality: P.R. China
Marital status: Married
Present Address: Department of Experimental Physics,
Freie Universität Berlin,
Arnimallee 14, D-14195 Berlin,
Germany
Tel: 0049-30-838 56152 (office)
Fax: 0049-30-838 56560
EMAIL: yhjjiang@physik.fu-berlin.de

Academic Background:

Sep. 1988–July 1992: Henan Normal University, China (Undergraduate student)
July, 02, 1992: B. Sc. in theoretical physics
Sep.1992–June 1995: Henan Normal University, China (Graduate student)
June, 24, 1995: M. Sc. in atomic and molecular physics
July 1995–Oct. 2000: Henan Normal University, China (Lecturer)
Mar. 1998–May 1998: Phys. Instit. Beijing, China (Visiting Scholar)
Nov. 2000–present Freie Universität Berlin, Germany (Doctoral student)

Research Backgrounds:

Experiment: VUV and X-ray spectroscopy of atoms and molecules
in the gas phase

Theory: Atomic and molecular interactions with electrons,
positrons, and photons

Publications and Conference contributions

Publications

1. Y.H. Jiang, R. Püttner, R. Hentges, J. Viefhaus, M. Poiguine, U. Becker, J. M. Rost, and G. Kaindl, Phys. Rev. A **69**, 042706 (2004),
Partial cross sections of doubly excited helium below the ionization threshold I_7
2. Y. H. Jiang, R. Püttner, M. Martin, R. Follath, J. M. Rost, and G. Kaindl, Phys. Rev. A **69**, 052703 (2004),
Isotope shifts of double-excitation resonances in helium
3. Y.H. Jiang, R. Püttner, G. Kaindl, J. Phys. B **38**, 2157 (2005),
Theoretical photoionization partial cross sections and angular distributions of doubly excited helium
4. Y. H. Jiang, R. Püttner, R. Hentges, J. Viefhaus, M. Poiguine, C. Cacho, U. Becker, J. M. Rost, and G. Kaindl, J. Phys. B **39**, L9 (2006),
Partial cross sections of doubly excited helium below the ionization thresholds I_8 and I_9
5. M. Poiguine, R. Püttner, M. Martin, V. Pennanen, M. Jurvansuu, Y. H. Jiang, S. Aksela, and G. Kaindl, Phys. Rev. A (submitted),
Detailed studies of the normal Auger spectra in H_2S
6. Y. H. Jiang, R. Püttner, D. Delande, M. Martins, G. Kaindl, Phys. Rev. Lett. (in preparation)
Slow transition to chaos in the $^1P^o$ doubly excited helium

Invited talks in the international conferences

7. “Quantum signatures of Chaos in doubly excited helium”: International Workshop on Photoionization (IWP) (July 27, 2005, Campinas, Brazil).

Oral presentations and posters

8. “Partial cross sections of doubly excited helium”: Ninth International Conference on Electronic Spectroscopy and Structure (ICESS9) (June 30, 2003, Uppsala, Sweden).
9. “Partial cross sections of doubly excited helium below the $N=7$ ionization threshold”: AMOP-Frühjahrstagung (German atom, molecule and optic physics annual meeting) (March 22, 2004, München)
10. “Experimental n -specific partial cross sections and angular distribution parameters of doubly excited helium”: Eighth European Conference on Atomic and Molecular Physics (ECAMP8) (July 6, 2004 Rennes, France).
11. “Quantum Chaos in doubly excited helium”: AMOP-Frühjahrstagung (German atom, molecule and optic physics annual meeting) (March 4, 2005, Berlin).
12. “Quantum signatures of Chaos in doubly excited helium”: DESY Research School: New Science in the VUV to soft X-Ray Domain (March 16, 2005, Hamburg, Germany).
13. “Doubly excited helium: from strong correlation to quantum chaos”: AMOP-Frühjahrstagung (German atom, molecule and optic physics annual meeting) (13 March, 2006, Frankfurt).

Invited talks in other institutes

14. “Quantum Chaos in doubly excited helium”: Max-Planck-Institut für Kernphysik (October 19, 2005, Heidelberg, Germany)